



Sol-gel materials for optofluidics - process and applications

Mikkelsen, Morten Bo Lindholm; Kristensen, Anders

Publication date:
2011

Document Version
Publisher's PDF, also known as Version of record

[Link back to DTU Orbit](#)

Citation (APA):
Mikkelsen, M. B. L., & Kristensen, A. (2011). Sol-gel materials for optofluidics - process and applications.

DTU Library

Technical Information Center of Denmark

General rights

Copyright and moral rights for the publications made accessible in the public portal are retained by the authors and/or other copyright owners and it is a condition of accessing publications that users recognise and abide by the legal requirements associated with these rights.

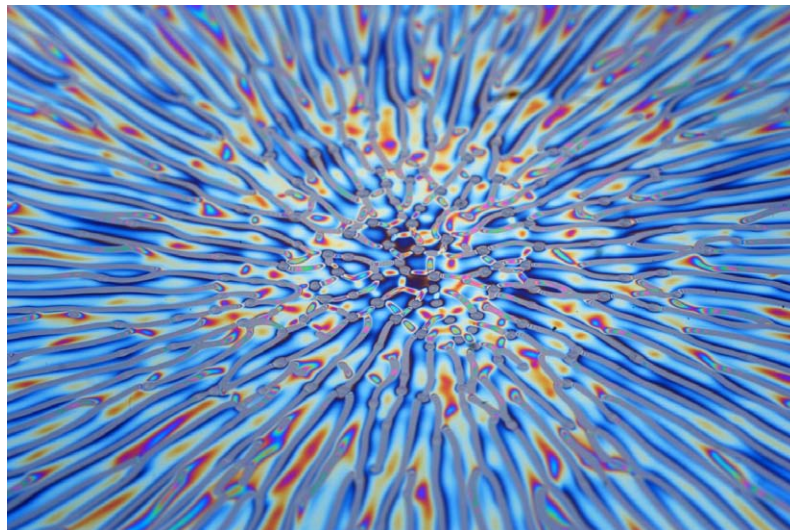
- Users may download and print one copy of any publication from the public portal for the purpose of private study or research.
- You may not further distribute the material or use it for any profit-making activity or commercial gain
- You may freely distribute the URL identifying the publication in the public portal

If you believe that this document breaches copyright please contact us providing details, and we will remove access to the work immediately and investigate your claim.

Ph.D. thesis

Sol-gel materials for optofluidics – process and applications

Morten Bo Lindholm Mikkelsen



Supervisor:

Prof. Anders Kristensen
DTU Nanotech – Department of Micro- and Nanotechnology,
Technical University of Denmark

Copyright: Morten Bo Lindholm Mikkelsen

31 October 2011

The front page image shows close-up photo, taken by Jesper Scheel, of unsuccessful spin-coating of MTES sol-gel material. Due to insufficient stirring, the material had not been fully hydrolyzed and was still phase-separated when deposited on the substrate. Though the coating was unsuccessful, it turned out rather beautiful, however.

Abstract

This Ph.D. thesis is concerned with the use of sol-gel materials in optofluidic applications and the physics of DNA molecules in nanoconfinement.

The bottom-up formation of solid material, which is provided by the sol-gel process, enables control of the chemical composition and porosity of the material. At early stages of gelation, thin gel coatings can be structured by nanoimprint lithography, and purely inorganic silica materials can be obtained by subsequent thermal annealing. The sol-gel process thus constitutes a unique method for nanofabrication of silica materials of special properties.

In this work, sol-gel silica is introduced as a new material class for the fabrication of lab-on-a-chip devices for DNA analysis. An imprint process with a rigid, non-permeable stamp was developed, which enabled fabrication of micro- and nanofluidic silica channels in a single process step without use of any high-vacuum techniques. Sealing of the channels was performed by fusion bonding of a glass cover slip to the imprinted surface, and the applicability of the device was demonstrated by sizing experiments on DNA molecules confined in the imprinted nanochannels.

In addition, in a fused silica device, the dynamics of linear and circular DNA molecules was studied under pressure driven flow in a slit channel with arrays of transverse nanogrooves. In the nanogroove geometry, transport occurs through two states of propagation: a slow, stepwise groove-to-groove translation called the 'sidewinder' and a fast, continuous tumbling across the grooves called the 'tumbleweed'. Dynamical transitions between the two states cause DNA molecules to exhibit both size- and topology-dependent velocities that may be utilized for separation.

By templating the porosity of sol-gel silica with sub-wavelength latex particles, tuning of the effective refractive index of the material was enabled. Using nanoimprint lithography, a diffraction grating with refractive index of 1.33 was fabricated. This low-index grating was used to demonstrate reconfigurability of an optically functional surface topography by electrophoretic actuation of charged latex nanoparticles. Preliminary results showed 22 dB modulation of the intensity of the first diffraction order.

Sol-gel material was also used as a permeable solid matrix for immobilization of analyte-sensitive dye molecules, thus constituting a sensor material for use in reagent-based optical sensing systems. Using the principle of hemiwicking, a method that enables deposition of the liquid sensor material in a homogeneous layer on a well-defined region of a surface was developed. The method simplifies the fabrication of optical sensors integrated in disposable lab ware.

Dansk resumé

Denne Ph.D.-afhandling omhandler brugen af sol-gel-materialer i optofluide systemer samt fysikken af DNA molekyler fanget i nanokanaler.

Sol-gel-materiale dannes ved polymerisering af separate molekyler til en gel, hvilket muliggør kontrol af materialets kemiske sammensætning og porøsitet. Tidligt i geleringsprocessen kan tynde gel-film nanostruktureres ved prægning af overfladen med et stempel, og rent inorganiske silika materialer kan opnås ved efterfølgende termisk behandling af den prægede film. Sol-gel-processering udgør derved en unik metode til nanofabrikation af silikamaterialer med specielle egenskaber.

I denne afhandling introduceres sol-gel-silika som en ny materialeklasse til fremstilling af lab-on-a-chip-systemer til brug for DNA-analyse. En prægeproces blev udviklet, i hvilken et ikke-permeabelt silicium-stempel muliggjorde fabrikation af væskekanaler i mikro- og nanostørrelse i et enkelt procestrin, uden brug af høj-vakuump-teknikker. Kanalerne lukkedes ved at fusions-bonde et glaslåg til den prægede overflade, og anvendeligheden af den fremstillede chip blev demonstreret ved at udføre længdemålinger på DNA-molekyler fanget i de prægede nanokanaler.

Desuden blev dynamikken af lineære og cirkulære DNA-molekyler i trykdrevet væskeflow studeret i en lav nanokanal med tværgående nanoriller. I denne geometri foregår transporten af molekyler i to tilstande: En langsom, trinvis rille-til-rille bevægelse, kaldet 'sidewinder', og en hurtig, uafbrudt tumlende bevægelse over rillerne, kaldet 'tumbleweed'. Dynamiske skift mellem disse to tilstande får DNA-molekylerne til at udvise både længde- og topologiafhængige hastigheder, som kan bruges til separering.

Ved brug af latex-partikler, som er mindre end bølgelængden af lys, kan der skabes en designet porøsitet i et sol-gel-silikamateriale, således at det effektive brydningsindeks af materialet kan tunes. Ved prægning af dette materiale med et nanostruktureret stempel blev et diffraktionsgitter med et brydningsindeks på 1,33 fremstillet. Dette gitter blev anvendt til at demonstrere rekonfigurering af en optisk funktionel overfladestruktur ved elektroforese af ladede latex-nanopartikler. Foreløbige resultater viste 22 dB modulering af intensiteten af første diffraktionsorden.

Sol-gel-materiale blev også benyttet som permeabelt fast stof til fastholdelse af analytfølsomme farvestofmolekyler for derved at danne et sensormateriale til brug i reagensbaserede optiske sensorsystemer. Ved brug af hemiwicking blev en metode udviklet til at sprede det flydende sensormateriale i et ensartet lag i et veldefineret område på en overflade. Denne metode forsimples fremstillingen af integrerede optiske sensorer i engangslaboratorieudstyr.

Preface

This thesis is submitted in partial fulfillment of the requirements for obtaining the degree of Philosophiæ Doctor (Ph.D.) at the Technical University of Denmark (DTU). The work presented here has been carried out in the Optofluidics group at the Department of Micro and Nanotechnology (DTU Nanotech) and in the Danchip cleanroom facility.

The project was supervised by professor Anders Kristensen, whom I gratefully acknowledge for his enthusiasm and encouragement during the past eight years, more or less, which I have spent at DTU Nanotech under his supervision.

I also want to acknowledge all the past and present members of the Optofluidics group and thank you for being such good colleagues. In particular, I want to thank Rodolphe Marie for the good collaboration and fruitful discussions; and Mads Brøkner Christiansen, Thomas Buss, Christopher Lüscher, and Cameron Smith for the good collaboration, barbecues, and ski trips we have had.

This project could not have been realized if it had not been for the collaboration with SVI CNRS/Saint-Gobain in Paris. I gratefully acknowledge Jérémie Teisseire, Etienne Barthel, Elin Søndergård, and, in particular, Alban A. Leteilleur for introducing me to sol-gel materials and helping me getting the process to work. I also wish to thank Alban for his hospitality during my stays in Paris and his patience when I try to explain things in French.

Furthermore, I want to acknowledge and thank Henrik Flyvbjerg and Walter Reisner, for the collaboration on the work on DNA dynamics, and Jan H. Hansen and Hans Ole Nielsen, for the collaboration on sol-gel sensor materials.

Finally, I wish to thank my family and friends for their love and support during the past three years.



Morten Bo Lindholm Mikkelsen
DTU Nanotech – Department of Micro- and Nanotechnology
Technical University of Denmark
31 October 2011

Contents

Abstract	iii
Dansk resumé	v
Preface	vii
1 Introduction	1
1.1 Sol-gel materials in optofluidic applications	1
1.1.1 Optofluidics	1
1.1.2 Sol-gel materials	2
1.2 Objective of the thesis	2
1.3 Publications	3
1.4 Thesis outline	4
2 Nanoimprint lithography	7
2.1 Nanoimprint lithography	7
2.2 Material flow during imprint	8
2.3 Imprint materials and technology	9
3 Sol-gel materials	11
3.1 Sol-gel materials	11
3.2 The sol-gel process	12
3.2.1 Precursors	12
3.2.2 Hydrolysis	12
3.2.3 Condensation	13
3.2.4 Gelation	14
3.2.5 Properties of a thin gel film	15
3.2.6 Annealing	17
4 Nanofluidic sol-gel silica devices	21
4.1 Nanoimprint of sol-gel silica	21
4.2 Nanofluidic devices for DNA analysis	22
4.2.1 Fabrication of nanochannels	23
4.3 Nanofluidic sol-gel silica devices - results from Paper 1	24

4.3.1	Imprint process	24
4.3.2	Device assembly	26
4.3.3	Material deformation during annealing	27
4.4	Chapter summary	27
5	DNA in nanoconfinement	31
5.1	Introduction to DNA	31
5.1.1	DNA sequencing and separation	31
5.1.2	Lab-on-a-chip systems for DNA analysis	32
5.2	Modeling of confined DNA	33
5.2.1	Freely-jointed chain model	33
5.2.2	Entropic energy of a polymer chain	35
5.2.3	Excluded volume interactions	36
5.2.4	Confined polymers	36
5.3	Extension measurements	38
5.3.1	Results from Paper 1	39
5.4	Entropic trapping and separation	40
5.4.1	Results from Paper 2	41
5.5	Chapter summary	43
6	Reconfigurable optical surface topography	47
6.1	Optical reconfigurability by electrophoresis of nanoparticles	47
6.1.1	Applications for reconfigurable optical device	48
6.2	Fabrication of reconfigurable device	49
6.2.1	Charged latex particles for electrophoresis	50
6.2.2	Device fabrication	50
6.3	Results	52
6.4	Discussion	53
6.4.1	pH of latex solution	53
6.4.2	Closed porosity	54
6.5	Chapter summary	57
7	Deposition of sol-gel material using hemiwicking	59
7.1	Sol-gel-based optical sensors	59
7.2	Wetting of a surfaces	61
7.2.1	Surface energy	61
7.2.2	Contact angle θ_{eq}	61
7.2.3	Wetting of rough surfaces	62
7.3	Hemiwicking	63
7.3.1	Critical angle θ_c	63
7.3.2	Spreading of liquid by hemiwicking	64
7.4	Results from Paper 3	66
7.4.1	Sensor characterization	68
7.5	Chapter summary	69

<i>CONTENTS</i>	xi
8 Conclusions and outlook	71
A List of publications	75
B Paper 1	77
C Supplementary information for Paper 1	87
D Paper 2	93
E Paper 3	101

Chapter 1

Introduction

1.1 Sol-gel materials in optofluidic applications

The subject of this thesis is sol-gel materials and how they can be used in different optofluidic applications, such as lab-on-a-chip devices, reconfigurable optics, and reagent-based optical sensors. Furthermore, the thesis deals with confinement of DNA molecules in nanochannels and the dynamics of these molecules under pressure-driven flow in a nano-engineered topography.

In this chapter, the different topics of the thesis are briefly presented and related. More elaborated introductions with descriptions of state-of-the-art are found in the chapters devoted to the different applications.

1.1.1 Optofluidics

Optofluidics is the interdisciplinary research field that covers optics and fluidics [1]. While each of the topics date back several hundred years, the two topics in combination have gained increasing interest during the past decade due to the possibility of integrating both optics and fluidics in micro- and nanofabricated systems [2-5]. The integration of microfluidics with optical components and methods has many advantages:

- In microfluidic systems, such as lab-on-a-chip devices [6], optics enable imaging [7] or sensing [8] of biomolecules or measuring of the concentration of analytes [9, 10].
- In optical systems, liquids enable tuning of optical properties, e.g., by changing the concentration of solutes [11] or actuating suspended particles or liquid crystals [12, 13], which enable the optical functionality of the system to be reconfigured.

An important aspect in optofluidics is material properties. While fluidic systems mainly rely on mechanical and surface properties of the device material, optical systems mainly rely on optical properties, such as refractive index, fluorescence, and absorption. For an optofluidic device to work, all of the material requirements must be met.

Another key issue is material structuring since many functionalities are based on surface structures:

- Surface structures with dimensions of the order of the characteristic length of biomolecules enable controlled interaction with these molecules and can thus constitute tools for analysis of biomolecules, such as DNA or proteins [14].
- Surface structures with dimensions below the order of the wavelength of light enable interaction with light so as to make optical elements with special properties, such as photonic crystals [15], anti-reflective surfaces [16], or surfaces with structural colors, like the wings of butterflies [17].
- Surface structures with dimensions below the capillary length provide enhanced control of the wetting properties of a surface and enable, e.g., self-cleaning or antifogging properties [18–20].

Such surface structures form the basis of the functionality of the optofluidic applications presented in this thesis, and they can be made in either of two ways: by top-down methods, where the surface of a bulk material is structured by removal of material, or by bottom-up methods, where atoms or molecules are arranged to form structures [21].

1.1.2 Sol-gel materials

In the sol-gel process, which is introduced in Chap. 3, solid material is produced in a bottom-up process by polymerization of precursor molecules to form a gel. This bottom-up formation of material provides control of the chemical composition and structure of the material and enables materials of, e.g., special mechanical, optical or thermal properties [22, 23]. At early stages of gelation, thin gel coatings can be structured by nanoimprint lithography, and purely inorganic silica materials can be obtained by subsequent thermal annealing. The sol-gel process thus constitutes a unique method for nanofabrication of silica materials with special properties.

The tunable optical and mechanical properties of sol-gel silica and the easy nanostructuring by imprint lithography make this kind of material convenient for use in optofluidic applications. For example, the ability to control the porosity of a silica material enables tuning of the refractive index [24], and silica nanostructures with a refractive index equal to that of a liquid, or even lower, can then be produced [25].

1.2 Objective of the thesis

In this thesis, several different optofluidic applications are presented. The main objectives of these applications are:

- Fabrication of silica lab-on-a-chip devices for DNA analysis, featuring both micro- and nanochannels, by imprint of sol-gel material. Fusion bonding of a glass lid to the imprinted surface to seal the nanochannels. Demonstration of applicability of the device by measuring the length, using fluorescence microscopy, of DNA molecules confined in the nanochannels.

- Study of the dynamics of DNA molecules under pressure-driven flow in a fused silica device with entropic traps. Demonstration of size- and topology-dependent velocities.
- Fabrication of a low-index silica diffraction grating on transparent electrodes and demonstration of reconfigurability by electrophoretic actuation of charged latex nanoparticles.
- Demonstration of method for deposition of liquid sol-gel sensor material in a homogeneous film on a well-defined region of a microstructured surface, which simplifies the fabrication of integrated optical sensors.

Despite the different nature of these applications, they are all based on optics, microfluidics and surface structuring. Three of them include sol-gel material, and two of them deals with confined DNA. An overview of the mutual relations between the different topics and the properties they provide for the applications is sketched in Fig. 1.1. Furthermore, nanoimprint lithography is used as fabrication method in three of the four applications.

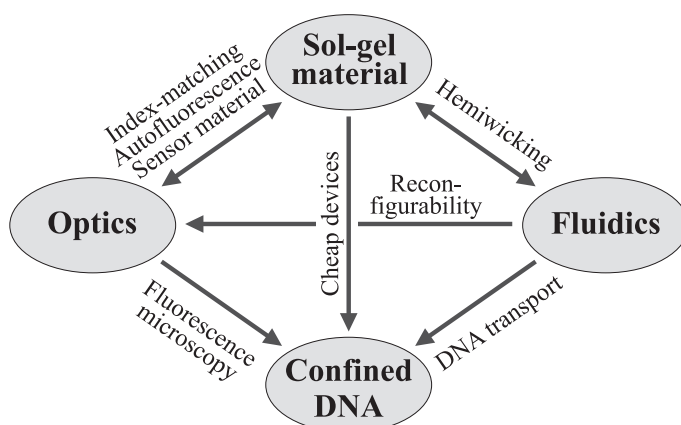


Figure 1.1: Sketch of the relations between the different topics of this thesis and the properties they provide for the applications.

1.3 Publications

The work presented in this thesis has resulted in three peer-reviewed journal papers which are included in the Appendix:

Paper 1: Morten Bo Mikkelsen, Alban A. Letailleur, Elin Søndergård, Etienne Barthel, Jérémie Teisseire, Rodolphe Marie, and Anders Kristensen, All-silica nanofluidic devices for DNA-analysis fabricated by imprint of sol-gel silica with silicon stamp. *Lab on a Chip* **12**, 262-267 (2012). Paper included in App. B.

Paper 2: Morten Bo Mikkelsen, Walter Reisner, Henrik Flyvbjerg, and Anders Kristensen, Pressure-driven DNA in nanogroove arrays: Complex dynamics leads to length- and topology-dependent separation, *Nano Letters* **11**, 1598-1602 (2011). Paper included in App. D.

Paper 3: Morten Bo Mikkelsen, Rodolphe Marie, Jan H. Hansen, Dorota Wencel, Colette McDonagh, Hans Ole Nielsen, and Anders Kristensen, Controlled deposition of sol-gel sensor material using hemiwicking, *Journal of Micromechanics Microengineering* **21**, 115008 (2011). Paper included in App. E.

These papers are considered part of the thesis, and it is the intension that they should be read together with the thesis. The chapters of the thesis that cover the same applications as the papers are written as an introduction in which the background, state-of-the-art, and the main results of the papers are presented. An overview of all publications is found in App. A.

A patent application regarding the method for uniform deposition of sol-gel sensor material, which is described in Paper 3, has been submitted. Another patent application regarding the method for reconfiguring an optically functional surface topography by electrophoresis of nanoparticles, which is described in Chap. 6, is under preparation.

1.4 Thesis outline

The thesis is organized as follows:

Chapter 2: Nanoimprint lithography.

A short introduction to nanoimprint lithography is given and the most important aspects of the technology are described.

Chapter 3: Sol-gel materials.

A general introduction to sol-gel materials is given. Special emphasis is put on the processing of thin films of these materials.

Chapter 4: Nanofluidic sol-gel silica devices.

Nanoimprint of sol-gel materials is introduced, and the process for fabrication of nanofluidic devices and the main results of Paper 1 are presented.

Chapter 5: DNA in nanoconfinement.

A short introduction to polymer physics and confined DNA is given. DNA sizing experiments from Paper 1 are presented. Entropic trapping of DNA is introduced and the main results of Paper 2 are presented.

Chapter 6: Reconfigurable optically functional surface topography.

Preparation and nanoimprint of a low-index sol-gel silica is described. Fabrication of a device for reconfiguring of the diffraction grating by electrophoresis of latex nanoparticles is described and preliminary results are presented and discussed.

Chapter 7: Controlled deposition of sol-gel sensor material using hemiwicking.

A method for uniform spreading of liquid sol-gel sensor material on a microstructured surface is described and the main results of Paper 3 are presented.

Chapter 8: Conclusions and outlook.

Conclusions are drawn based on the experimental results and future development is discussed.

Appendix: Journal publications.

The journal publications, which the work of this thesis has resulted in, are found in the appendix.

Chapter 2

Nanoimprint lithography

2.1 Nanoimprint lithography

In nanoimprint lithography (NIL) [26, 27], the pattern of a nanostructured stamp is replicated into a softer imprint material by direct mechanical contact with the stamp. A sketch of the process is shown in Fig. 2.1. As pressure is applied to the backside of the stamp, it sinks into the imprint material, which deforms viscously, conformal to the stamp structures. Before release of the stamp, cross-linking of the imprint material or cooling below the glass transition temperature T_g is required in order to harden the material and retain the replicated structures.

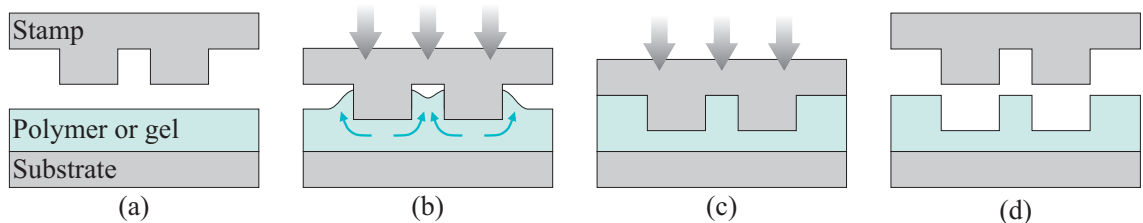


Figure 2.1: Cross-sectional sketch of the different stages of nanoimprint lithography. (a) The imprint stack consists of a nanostructured stamp and a substrate with a thin film of viscous polymer or gel. (b) When pressure is applied on the backside of the stamp, the protrusions sink into the soft imprint material, which is squeezed out and fills the cavities of the stamp. (c) Fully imprinted stamp. Before demolding, cross-linking of the imprint material (thermal or UV-induced) or cooling below the glass transition temperature is required to obtain a hard material. (d) Demolding. The stamp pattern has been transferred to the imprint material.

Traditionally, UV lithography has been used in microfabrication to transfer patterns in a parallel process by exposure of a photo-sensitive polymer to UV light through an optical mask [28]. In optical lithography, the resolution of the transferred pattern depends on the wavelength of the exposure light, and for fabrication of increasingly smaller features, it has been necessary to use light of increasingly shorter wavelength at the cost of increasingly complex and expensive lithography tools. Optical masks for UV lithography are fabricated using electron beam lithography, in which an electron-sensitive polymer is directly exposed

by a beam of electrons. The resolution is limited by the polymer thickness but may be down to the order of 1 nm [29]. Since electron beam lithography is a serial process, it is extremely slow for large area patterning of small structures and hence not suitable for production.

In nanoimprint lithography, the nanostructures of the stamp are defined by electron beam lithography as well. Like UV lithography, nanoimprint lithography thus provides a method for parallel transfer of these structures. The advantage of nanoimprint, however, is that the resolution of the transferred pattern, in principle, does not depend on the imprint tool. In most cases, the resolution is limited by the precision in fabrication of the stamp [30], and nanoimprint is therefore able to resolve structures that are too small even for extreme-UV lithography [31]. Hence, nanoimprint lithography is a convenient way to combine the high resolution of electron lithography with a parallel process, thus achieving a much higher throughput and lower price.

2.2 Material flow during imprint

An important aspect in nanoimprint lithography, is the thickness of the residual layer, which is the layer of imprint material left under the stamp protrusions when the imprint is finished. In order for the imprinted material to be used as mask for etching or lift-off, the residual layer often has to be removed by etching with an oxygen plasma. A thin residual layer of homogeneous thickness is therefore necessary, since over-etching may cause broadening of the imprinted features.

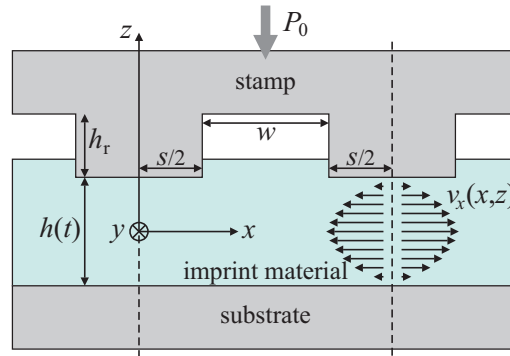


Figure 2.2: Cross-sectional sketch of material flow during nanoimprint. A hard stamp with protrusions of width s is pressed into a soft imprint material. The material flows out under the protrusions and fills up the cavities. The protrusion height is h_r , the cavity width is w , and the time-dependent thickness of imprint material under the protrusions is $h(t)$. The pressure on a single protrusion $P = P_0/P_C$, where P_C is the protrusion coverage density.

The imprint process can be modeled analytically when the imprint material is considered a Newtonian liquid [32]. For the situation sketched in Fig. 2.2, a relation for the

residual layer thickness as function of time $h(t)$ can be derived,

$$h(t) = \left(\frac{2P}{\eta_0 s^2} t + \frac{1}{h_0^2} \right)^{-1/2}, \quad (2.1)$$

where P is the pressure on a protrusion, s is the protrusion width, η_0 is the zero-shear viscosity, and h_0 is the initial film thickness. The imprint time t_f needed to reach a specific film thickness $h_f = h(t_f)$ is then

$$t_f = \frac{\eta_0 s^2}{2P} \left(\frac{1}{h_f^2} - \frac{1}{h_0^2} \right), \quad (2.2)$$

which is known as the Stefan equation [33, 34].

The time t_f is seen to be proportional to s^2 , and imprint of small protrusions is thus much faster than imprint of large protrusions. To achieve low residual layer thickness in a reasonable amount of time, nanoimprint lithography is thus normally only useful for replication of small structures. However, it may be combined with UV-lithography in order to produce features from nm-scale to cm-scale on the same substrate [35, 36].

While the small protrusions sink faster into the imprint material than larger ones, the stamp is exposed to different normal forces from the imprint material, depending on the size of the stamp protrusions. The uneven force distribution may cause the stamp to bend, which introduces defects in the replication, such as uneven residual layer thickness [37].

The actual material flow during imprint is much more complicated than what is modeled by the Stefan equation [38–41]. Surface energy [42], triboelectric charging [43], and shear effects [44] makes filling of the stamp cavities a complicated problem to model exactly. However, the Stefan equation can provide a basic understanding of the issues in nanoimprint lithography.

2.3 Imprint materials and technology

For patterning of a thermoplastic polymer, imprint is performed at temperatures above the glass transition temperature T_g , e.g. 50°C above T_g , where the material can be viscously deformed. For imprint polymers, T_g is typically in the range of 80°C–160°C. When the stamp has been completely imprinted, the polymer is cooled below T_g to stop material flow. For a thermoplastic material, the rheological behavior is reversible with respect to temperature, as long as the temperature is kept low enough for the material not to decompose. During heating of a thermoplastic material, only van der Waals bonds are broken, thereby allowing viscous flow of polymers, and when cooling down, the bonds are reestablished. Other things being equal, temperature thus provides complete control of the zero-shear viscosity η_0 [34, 44].

A machine for thermal nanoimprint consists, in principle, just of two hotplates that are pressed together with the imprint stack in between. However, for industrial production, an important issue is the time it takes to heat above and cool below T_g , i.e., the thermal cycling time [45]. Several techniques have been developed for increasing the throughput

of thermal imprint lithography and reduce the thermal cycling time [46]. An example of this is thermal Step & Stamp [47], where a small heatable stamp, which reduces the thermal mass, is stepped over the surface of the substrate in a sequential imprinting process. Reduction of the stamp size also decreases the costs of fabrication and inspection of the master. Continuous imprinting at constant stamp temperature can be achieved in the thermal Roll-to-Roll process [48], where a heated, rotating, nanopatterned cylinder imprints thermoplastic polymer foils.

In the case of imprint of thermoset or UV-curable materials, the imprint material is cured by exposure to heat or UV-light, which cross-links and hardens the materials. The cross-linking produces a slight shrinkage during imprint. Compared to thermoplastics, this kind of materials often has very low molecular weight, which gives low viscosity and easy imprint of large structures. For UV-curable materials, very fast cycle times can be obtained since the exposure time is usually much faster than heating and cooling of the imprint stack [49].

For industrial production of UV-curable imprint materials, UV Roll-to-Roll [50] and UV Step & Flash imprint [51–53] technologies exist. UV Step & Flash imprint, in competition with extreme-UV lithography, is considered candidate for the next-generation lithography technology in the semiconductor industry [31, 54].

While extreme-UV lithography is still used in high-end large-scale production, NIL is particularly well suited for nanostructuring of materials that are not sensitive to photons. Examples of these are special polymer materials [55, 56] or even Pyrex glass [57]. Furthermore, sol-gel materials [58], which will be introduced in the following chapter, can be patterned by nanoimprint lithography. Another advantage of NIL is the possibility to replicate three-dimensional or multi-level structures in a single process [59]. This is not possible in planar processing.

Chapter 3

Sol-gel materials

3.1 Sol-gel materials

In a sol-gel process, ceramic materials are prepared from a chemical solution of *precursor* molecules. Under influence of water, the precursors are *hydrolyzed*, which enables them to link together in a polymerization process and form a solution of polymeric particles, i.e. a *sol*. A sol is defined as a colloidal suspension of solid particles in liquid, where the particles size is so small (sub-1 μm) that gravitational forces are negligible and Brownian motion dominates [60]. By continuous growth of the polymeric particles, a macroscopic polymer network, i.e. a *gel*, may be formed. A gel is defined as a substance that contains a continuous solid skeleton enclosing a continuous liquid phase. In contrast to the viscous behavior of a sol, the continuity of the solid structure gives elasticity to a gel [60]. The process is sketched in Fig. 3.1.

The gel may be dried without shrinkage of the solid skeleton to form an *aerogel*, which has extremely low density and refractive index [61, 62], or dried with shrinkage of the solid skeleton to form a *xerogel*, a much denser, but still porous, material. Xerogels are used, e.g., as permeable matrix for immobilization of reagent dyes in optical sensing systems [63], see Chap. 7, or catalysts [64] in reactors. Furthermore, thin film coatings of xerogel are used, e.g., as spin-coatable dielectrics (spin-on glass) in microelectronics [65], optical coatings [23], self-cleaning coatings [66], or scratch protective coatings [67, 68].

When the gel is annealed above 450°C in oxygen atmosphere, the organic compounds of the material are calcinated, and purely inorganic glass materials are obtained. At high temperature > 1000°C, sintering will close the porosity of the material, and dense materials can be obtained.

The bottom-up formation of solid material, which is provided by the sol-gel process, enables control of the chemical composition and porosity of the material. This makes it possible to produce materials of, e.g., special mechanical, optical or thermal properties, which can not be made in any other manner. The low viscosity of the sol at early stages of gelation enables thin film coatings to be made by spin-coating [69], spray-coating [68], or dip-coating [70], and the gel films are easy structured by casting [71] or imprint [58, 72–74]. This makes sol-gel derived materials very versatile. In the following sections,

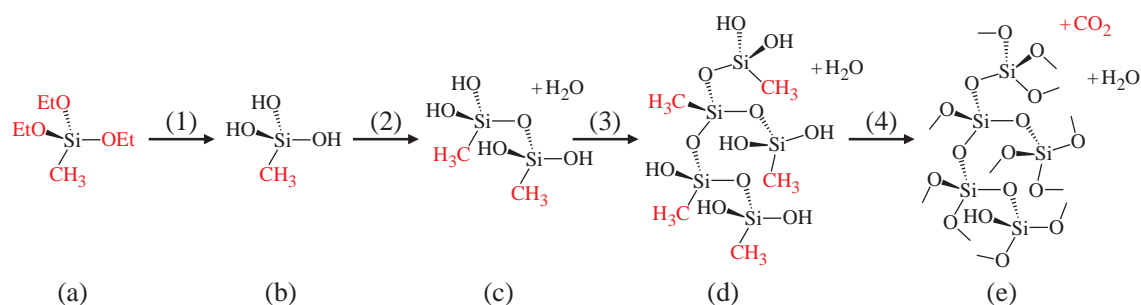


Figure 3.1: Sketch of the chemical structure at different stages of a sol-gel process. *EtO* denotes an ethoxy group ($\text{CH}_3\text{CH}_2\text{O}-$). The alkoxysilane precursor (a) undergoes a hydrolysis process (1) during which the alkoxy side groups are exchanged by hydroxyl groups. The hydrolyzed precursor (b) forms bonds to other precursors in a condensation process (2) to build polymeric molecules (c). As the polymerization process (3) proceeds, a gel (d) is eventually formed. By thermal annealing of the gel, the organic compounds are calcinated (4) and a purely inorganic material (e) is produced.

characteristics of sol-gel materials are further described.

3.2 The sol-gel process

3.2.1 Precursors

Precursors for sol-gel materials are typically metal alkoxides. An alkoxy is a ligand formed by removing a proton from the hydroxyl on an alcohol, such as methoxy ($\text{CH}_3\text{O}-$) or ethoxy ($\text{CH}_3\text{CH}_2\text{O}-$), where the hyphen indicates an electron that is capable of forming a bond. Metal alkoxides are metal atoms which have one or more alkoxide side groups [60]. Precursors with different side groups have different reaction kinetics which influence the gel structure and hence the properties of the final material [75], and using mixtures of different precursors, specific properties can be obtained [72, 76]. In this work, the alkoxysilanes tetraethoxysilane (TEOS) and methyltriethoxysilane (MTES) were used, see Tab. 3.1 and Fig. 3.1a.

Other than alkoxysilanes, examples of precursors are titanium compounds ($\text{Ti}(\text{OC}_4\text{H}_9)_4$), used, e.g., for photocatalytic coatings [77], zirconium compounds ($\text{Zr}(\text{OC}_3\text{H}_7)_4$), used, e.g., for advanced optical materials [22], and tin compounds ($\text{Sn}(\text{CH}_3\text{COO})_4$), used, e.g., with indium dopant to produce transparent conducting indium tin oxide (ITO) thin films [78].

3.2.2 Hydrolysis

In contact with water, metal alkoxides are readily hydrolyzed, see Fig. 3.1b. This reaction exchanges the alkoxy groups ($-\text{OR}$) of the precursor with hydroxyl groups ($-\text{OH}$), where, for generality, R represents an alkyl so that $-\text{OR}$ is an alkoxy, and releases alcohol. In the

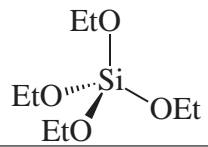
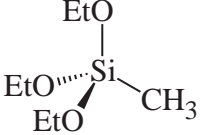
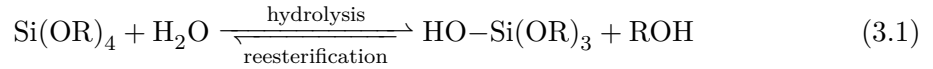
Alkoxysilane precursors		
Tetraethoxysilane (TEOS) 	Linear formula: CAS number: Density: Molecular weight:	$\text{Si}(\text{OCH}_2\text{CH}_3)_4$ 78-10-4 0.933 g/ml 208.33 g/mol
Methyltriethoxysilane (MTES) 	Linear formula: CAS number: Density: Molecular weight:	$\text{CH}_3\text{Si}(\text{OCH}_2\text{CH}_3)_3$ 2031-67-6 0.895 g/ml 178.30 g/mol

Table 3.1: Chemical structure and properties of alkoxysilane precursors. EtO is shorthand notation for an ethoxy group, $\text{CH}_3\text{CH}_2\text{O}-$.

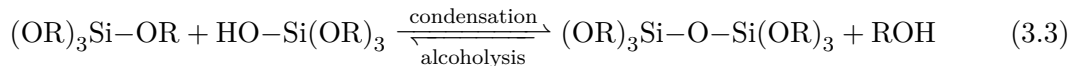
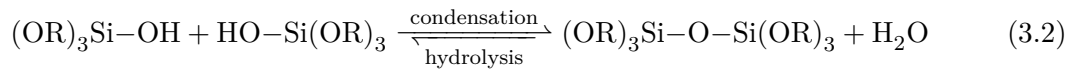
general form, hydrolysis of a single side group is written



Depending on the amount of water and catalyst present, hydrolysis may continue to completion, so that all alkoxy groups are exchanged by hydroxyl groups, but the reverse arrow indicates that the reaction may go backwards in a reesterification process as well. Mineral acids or bases are used to catalyze the hydrolysis reaction, and the rates of the two reactions depend on the catalyst concentration, i.e., pH. Water and alkoxysilanes are immiscible, but vigorous stirring improves mixing, and the alcohol released as by-product of the hydrolysis helps homogenizing the initially phase separated system. After hydrolysis of the precursors, a single phase system is obtained.

3.2.3 Condensation

When a hydrolyzed precursor molecule encounters another precursor, the two molecules can link together in a condensation reaction, see Fig. 3.1c, by which siloxane bonds ($\text{Si}-\text{O}-\text{Si}$) are formed and water or alcohol is released



Whether the water-producing (3.2) or the alcohol-producing (3.3) reaction takes place depends on the side groups taking part in the reaction. The number of hydroxyl groups increases with the degree of hydrolysis, which in turn depends on the water concentration and the pH. The probability of side group encounters depends on the mobility of the molecules, and hence temperature and steric hindrance.

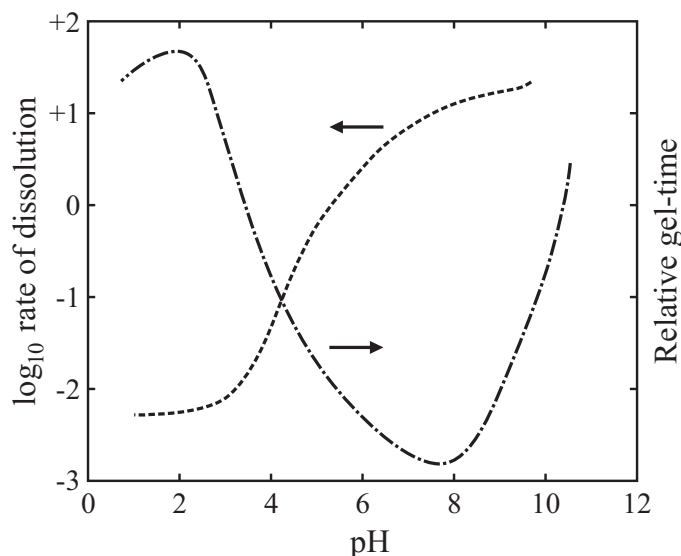


Figure 3.2: Example of pH-dependence of dissolution rate (left axis) and relative gel time (right axis) for aqueous silicate. Figure reproduced from Brinker and Scherer [60].

For precursor molecules that can form at least two bonds, these condensation reactions can continue to build larger and larger molecules in a polymerization process. The structure of the polymeric network depends on the *functionality* of the precursors, i.e., the number of bonds that each monomer can form. Fully hydrolyzed TEOS molecules can form four bonds, whereas MTES molecules only form three bonds, since the methyl group is not hydrolyzed. For both precursors, three-dimensional polymer networks with complex branching will be made, but MTES will have less branching than TEOS due to the lower functionality. The presence of the methyl group on the MTES monomer thus influences the mechanical properties of the polymer network [75].

The growing polymer network is continuously dissolved due to alcoholysis and hydrolysis of siloxane bonds. Since acids or bases are used to catalyze the hydrolysis reaction, pH controls the net rate of the reversible reactions 3.1–3.3 and causes dissolution and growth of the silica network to exhibit a strong pH-dependence, as shown in Fig. 3.2. At low pH, dissolution of the polymer is seen to be very slow. The bonds are relatively permanent, which favors formation of viscous polymeric sols (linear or chain molecules). At high pH, dissolution of the polymer is much faster. Reversibility of the bonds favors formation of particulate sols (condensed particles) [60, 79].

3.2.4 Gelation

During formation of a gel, polymer clusters grow by condensation. These clusters collide and link together, until, eventually, a single giant cluster extending throughout the solution is produced, see Fig. 3.1d. The time it takes for this macroscopic polymer to be made is called the *gel-time*, and it can be measured as the time of an abrupt rise of the viscosity [60, 69]. Figure 3.2 also shows pH-dependence of the gel-time, which can be interpreted as

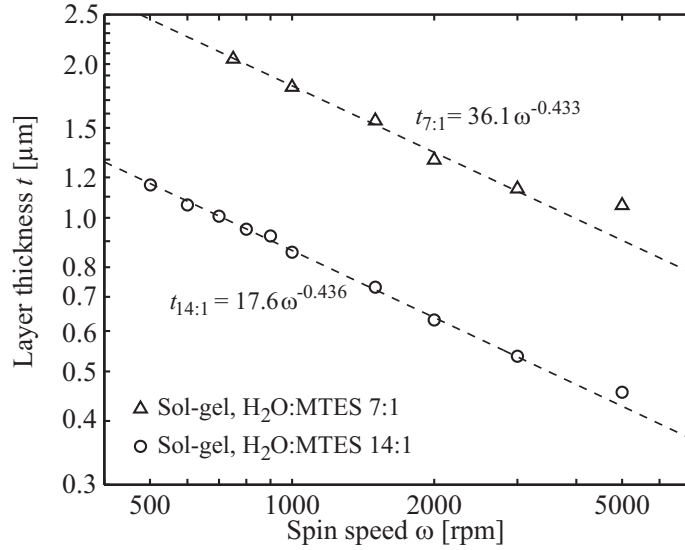


Figure 3.3: Log-log plot of spin-coated film thickness t as function of rotation frequency ω for sol-gel solutions of H_2O :MTES ratios of 7:1 and 14:1. The sols were prepared using pH 2.0 HCl and aged for 4 hours. 50 s spin time and 1000 rpm/s acceleration were used. Dashed lines show fitted power functions. It is observed that the exponent is the same for both solutions and that the gel thickness is doubled when the H_2O :MTES ratio is halved.

a measure of the overall reaction kinetics. At low pH, gel formation is very slow, and the sol contains separate polymeric clusters, as explained above. The rheological properties of the sol are controlled by aging of the sol [80] in order to let the clusters grow to a certain average size where thin film formation by spin-coating [69] or dip-coating [70] is possible. During coating, rapid evaporation of the solvent causes the polymeric clusters to collapse into a gel [60]. Figure 3.3 shows a plot of spin-coated film thickness as function of rotation frequency ω for two different sol-gel solutions. As is the case for spin-coating of polymers [28], a power-law dependence is observed. A thin film of gel can also be produced on a microstructured surface using the principle of hemiwicking, as it will be described in Chap. 7.

In this work, only thin films of sol-gel materials are used. However, bulk gel objects can be manufactured by gelation of the polymeric sol in a mold, and structuring of the gel is thus obtained by casting [71]. This process is favorable to do at higher pH where the gel-time is lower, according to Fig. 3.2.

3.2.5 Properties of a thin gel film

When a thin gel film has been made, most of the solvents, i.e., water and alcohol, have been removed. But due to the hydrophilic silica skeleton and the porosity of the gel, solvents are still present inside the pores.

In the confined space of a capillary, multi-layer adsorption of a vapor phase on the walls may eventually fill the pore, so that vapor condensation occurs below the saturation

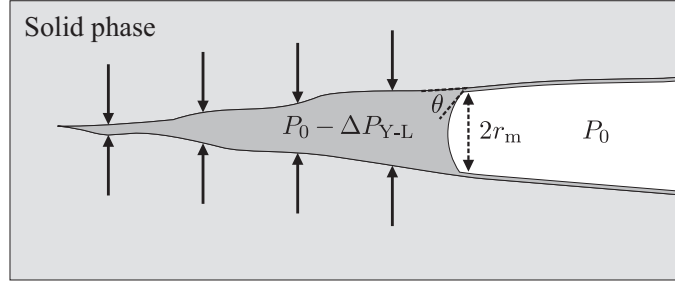


Figure 3.4: Sketch of water (dark gray) adsorbed in a nanopore of a solid material (light gray). The Young-Laplace pressure ΔP_{Y-L} over the meniscus puts the liquid inside the pore under tension. This tension is balanced by a tensile stress in the solid phase of equal magnitude [60], indicated by the arrows perpendicular to the walls of the pore. P_0 is the atmospheric pressure, θ is the contact angle, and r_m is the pore radius minus the thickness of adsorbed films on the pore walls.

vapor pressure p_{sat} . For a nanoporous material, depending on the pore size, liquid water will thus always be present in the pores at non-zero relative humidity [60]. As soon as a liquid phase is present inside the pore, surface tension creates a meniscus, as sketched in Fig. 3.4, which gives rise to a Young-Laplace capillary pressure [33]

$$\Delta P_{Y-L} = \frac{2\gamma_{lg} \cos \theta}{r_m}, \quad (3.4)$$

where γ_{lg} is the surface tension of the liquid-vapor interface, θ is the contact angle, and r_m is the pore radius minus the thickness of adsorbed films on the walls of the pores.

The Kelvin equation gives a relation between the relative humidity of the atmosphere and the pore radius where the capillary condensation occurs [81]

$$\ln(\text{RH}) = \ln\left(\frac{p}{p_{\text{sat}}}\right) = -\frac{\Delta P_{Y-L} V_m}{RT} = -\frac{2\gamma_{lg} V_m \cos \theta}{RT r_m}, \quad (3.5)$$

where p/p_{sat} is the relative partial pressure of water, i.e., the relative humidity (RH), $V_m = M/\rho$ is the molar volume of the liquid, M is the molar mass, ρ is the density, R is the gas constant, and T is temperature. When the relative humidity of the atmosphere is increased, liquid will fill up the pore until the pore radius r_m has been reached where the capillary condensation is balanced by evaporation. The amount of liquid in a porous material thus depends on the pore size and the relative humidity.

As explained by Brinker and Scherer [60], the capillary pressure puts liquid in the pore under tension. In a compliant gel, the tension in the liquid is supported by the solid skeleton, so that the walls of the pore are subjected to a tensile stress equal to the liquid tension which pulls them radially inward. This is sketched in Fig. 3.4. When the relative humidity of the atmosphere surrounding the gel is decreased, the menisci move towards smaller pore size, according to Eq. 3.5, causing the capillary pressure to increase. The correspondingly increased stress in the solid skeleton causes the gel to contract as the liquid evaporates from its pores. If the pressure is uniformly applied on the network, it will shrink uniformly and have no tendency to crack. However, large pressure gradients can develop through a thick gel, which may crack during drying.

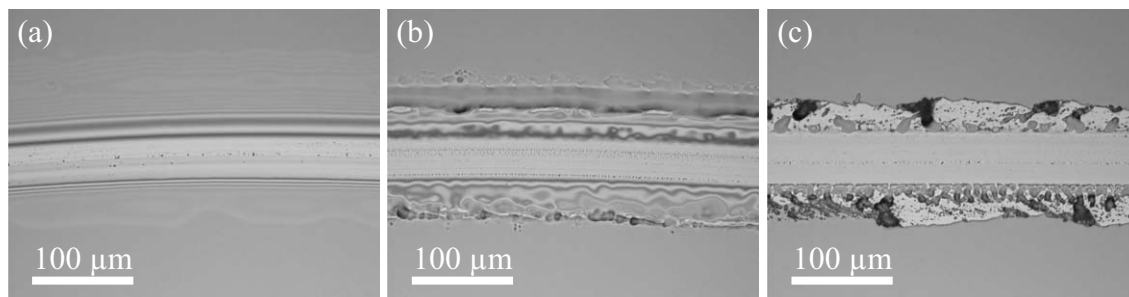


Figure 3.5: Scratch test. Optical microscope images show scratches in spin-coated gel film during different stages of thermal treatment. In the beginning (a), the gel is liquid and parallel thickness fringes are observed. Later (b), the gel has become more viscous, and whirls appear. Finally (c), the gel has become brittle, and delamination of the layer is seen.

Likewise, if the relative humidity of the atmosphere surrounding the gel is increased, the menisci will move towards larger pore size, causing the capillary pressure to decrease. The stress in the gel thus decreases, as more liquid is adsorbed in the pores, and the gel swells. Since the thickness of the gel film depends on the relative humidity, humidity sensors can be made from sol-gel derived materials [82, 83]. Swelling of the gel in wet atmosphere increases the mobility of the polymers, since steric hindrance is decreased. This causes the probability of side group encounters to increase, and hence the condensation rate increases as well. For spin-coated gel films, condensation can thus be decreased by storing them in dry atmosphere at low temperature, which reduce the mobility.

After gelation, stiffness and strength of the network continuously increase, since more and more bridging bonds are made by condensation. The stiffer the gel network becomes, the better it can withstand the capillary pressure, and it becomes less sensitive to the relative humidity. However, for nanostructuring of the gel film by imprint lithography, see the following chapter, it is required that viscous flow is still possible. The branching of polymer chains must therefore not prevent the polymers from sliding against each other, and the gel must not have reached the elastic state.

When heating a gel, the viscosity decreases since van der Waals bonds are broken and the mobility of the polymer chains is increased. Viscous flow of the gel is thus improved. However, the increased mobility also increases condensation, as explained in Sec. 3.2.3, which makes the gel stiffen faster. Molding of a gel must therefore be performed when the gel is in the right rheological state, which depends on humidity, temperature and time.

Quantitative monitoring of the rheological state of a thin gel film is complicated. Conventional viscosimetric methods use bulk materials, and *in situ* viscosity measurements of thin films are difficult [84, 85]. The easiest way to qualitatively monitor the state of a thin gel film is by scratch testing [86], as shown in Fig. 3.5.

3.2.6 Annealing

In order to accelerate condensation and obtain a hard material, thermal annealing at 100°C–150°C is necessary. After this annealing, the gel is still a hybrid material, consisting

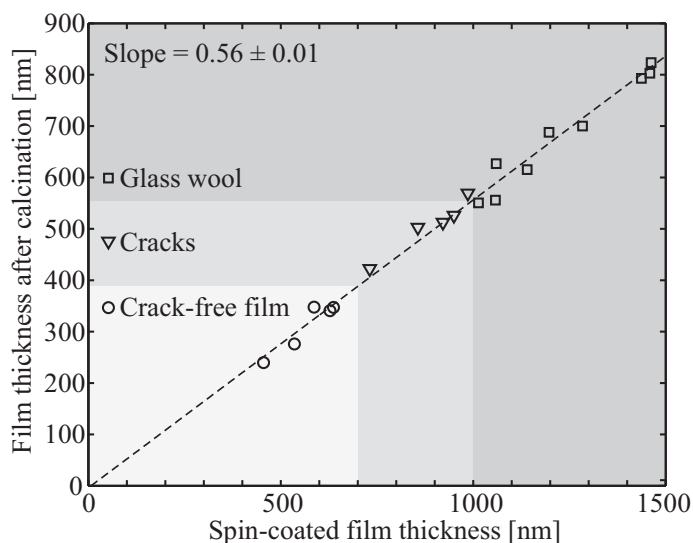


Figure 3.6: Thickness of sol-gel silica films on silicon substrates measured after calcination at 600°C as function of the initial spin-coated thickness. A linear reduction of the film thickness to 56% is seen. Circles show crack-free films, triangles show films with few cracks around surface defects and imprinted structures, squares show films that produced glass wool.

of a silica matrix with unbonded hydroxyl side groups and, in the case of the MTES precursor, methyl side groups. Though the organic content and the porosity of the material make it sensitive to organic solvents and strong acids and bases, the material is durable at this stage and find use in many applications [23, 63–65, 67, 68].

A purely inorganic glass material, see Fig. 3.1e, can be obtained by annealing of the gel in oxygen atmosphere at temperatures higher than 450°C. At the high temperature, condensation is pushed further and the organic compounds of the material are calcinated under influence of oxygen. Using Fourier transform infrared (FTIR) spectroscopy, this can be seen as an extinction of the Si–OH peak at 900 cm^{-1} for condensation and of the Si–CH₃ peak at 1250 cm^{-1} for calcination in the spectrum shown in Fig. 3.7. After calcination, a pure silica material is left, indicated by the Si–O–Si peak at 1100 cm^{-1} . Since most of the liquid phase disappear during spin-off, only trace amounts of catalyst (Cl) are present in the final material. Condensation and the removal of organics cause a large volume reduction of the material. As shown in Fig. 3.6, an unstructured MTES film shrinks to 56% of its initial thickness. Since the film adheres to the substrate, large in-plane compressive stress is induced, which may cause the film to crack. For films of final thickness above 1 μm , narrow bands of the material peels off and produces glass wool on the surface. Only films of final thickness less than 400 nm were free of cracks and thus useful. Cracking of the gel during annealing is further described in the supplementary information of Paper 1, see App. C.

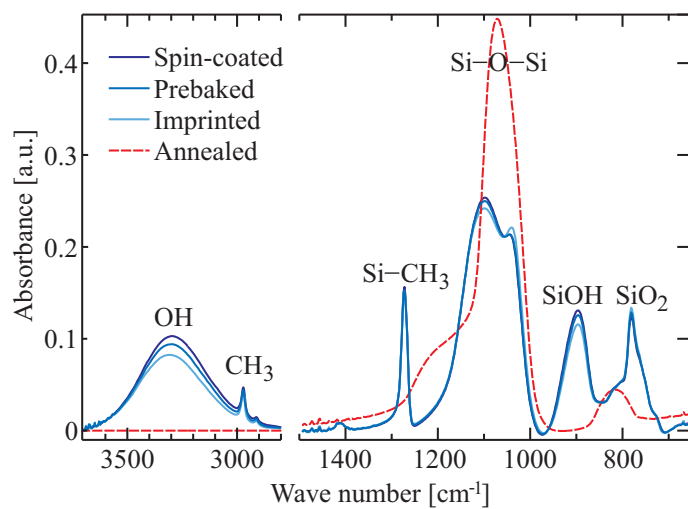


Figure 3.7: Fourier transform infrared (FTIR) spectrum of MTES sol-gel silica at various stages during imprint process. Decrease of the OH peak at 3300 cm^{-1} shows that water content of the gel film is reduced during prebake and imprint. Condensation is seen as a decrease in the Si-OH peak at 900 cm^{-1} . Extinction of both of these peaks are seen after annealing. Calcination of the methyl side groups is seen as an extinction of the Si-CH₃ peak at 1250 cm^{-1} . After calcination, a pure silica material is left, indicated by the Si-O-Si peak at 1100 cm^{-1} . Figure from Paper 1.

Chapter 4

Nanofluidic sol-gel silica devices

4.1 Nanoimprint of sol-gel silica

As described in the previous chapter, the sol-gel process offers possibilities to make glass materials starting from a liquid solution. The bottom-up approach to material processing enables easy surface structuring of gel films at early stage of gelation, due to viscous flow of the material, and nanostructured glass films can thus be produced by nanoimprint lithography.

Different examples of previous works on nanoimprint of sol-gel material are shown in Fig. 4.1 and include both direct imprint [58, 74] and reverse printing [73] techniques using permeable PDMS stamps. Non-permeable silicon stamps have been used for imprinting 15 nm lines in a SiO_2 - TiO_2 film [72]. If the same surface structures were to be made by top-down planar processing of a thin silica film or a silica substrate, in addition to a lithography process step, it would require reactive-ion etching, which is an expensive high-vacuum process. Furthermore, unique materials can be made using the sol-gel process [22, 25], and nanoimprint of such materials thus provides an unparalleled fabrication platform. An example is described in Chap. 6 where low-index nanostructures are fabricated by nanoimprint of a sol-gel material.

At early stages of gelation, a gel prepared from metal alkoxides exhibits some reversible thermoplastic behavior due to van der Waals bonds between polymer chains. However, thermally driven cross-linking by condensation, as described in Sec. 3.2.3, dominates the rheologic behavior for high temperatures or long times [86]. Cross-linking is not a reversible process as it involves establishment of covalent bonds. Since silica gels cross-link when heated, they are considered thermoset materials. As explained in Sec. 3.2.5, the rheological properties of a gel are influenced by pH, temperature history, and the relative humidity of the surroundings. Condensation is an on-going chemical reaction, which make imprint of sol-gel materials very different from thermoplastics.

Imprint of sol-gel materials is performed at low temperature, where the cross-linking rate is low [86]. When the material has flowed to fill the cavities of the stamp, heating of the material is performed to increase the cross-linking rate and obtain a stable material before demolding. After imprint, a calcination process is carried out to obtain an inorganic

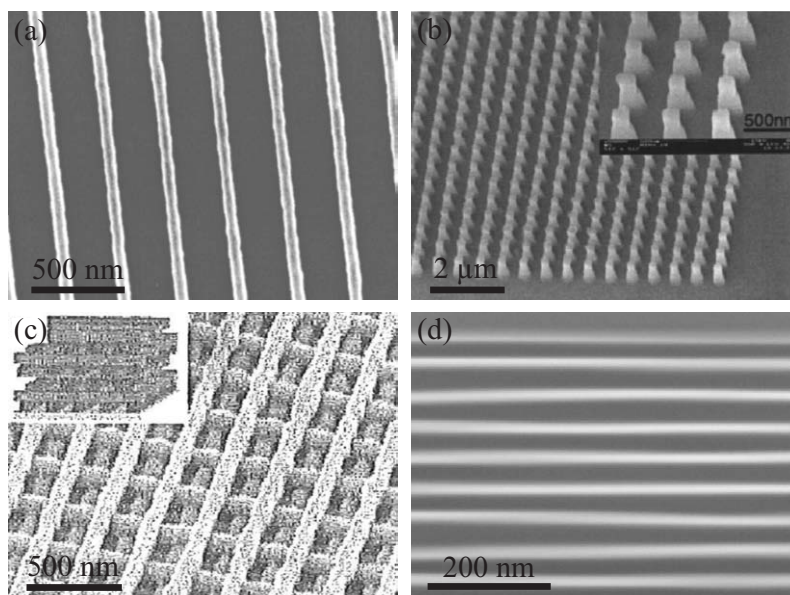


Figure 4.1: SEM images of examples of previous works on imprint of sol-gel material. (a) 80 nm lines of $\text{SiO}_2\text{-TiO}_2$ fabricated by direct imprint of glass stamp [72]. (b) Array of 160 nm pillars made by imprint of PDMS stamp [58]. (c) Woodpile 3D-structure (70 nm lines, 240 nm pitch) created using direct imprint of PDMS stamp and planarized sacrificial polymer [74]. (d) 15 nm TiO_2 lines fabricated by reverse imprint using PDMS stamp [73].

material. These stages of the imprint process are sketched in Fig. 4.2 together with the chemical structure of the sol-gel material. It is important to notice in Fig. 4.2 that water is released during the condensation reaction, see also Eq. 3.2. Typically, permeable PDMS stamps [58, 86] are used to allow diffusion of water vapor.

4.2 Nanofluidic devices for DNA analysis

The ability to produce glass nanostructures directly by imprint lithography makes sol-gel processing interesting for simple and cheap fabrication of high-quality nanofluidic devices for single-molecule studies of DNA. Such a device is sketched in Fig. 4.3 and consists of an array of nanochannels in the center of the device, where DNA molecules, e.g., are confined and stretched due to an entropic force. Confinement of DNA molecules is further described in Chap. 5. Four inlet holes provide fluidic access to the nanochannels, and, in order to assure easy liquid transport, microchannels lead from the inlet holes to nanochannel array. The device thus contains channels of different depths, which require separate lithography and etching steps when using planar processing techniques. Using imprint lithography, however, a multi-level stamp can produce all channel depths in a single process step [59].

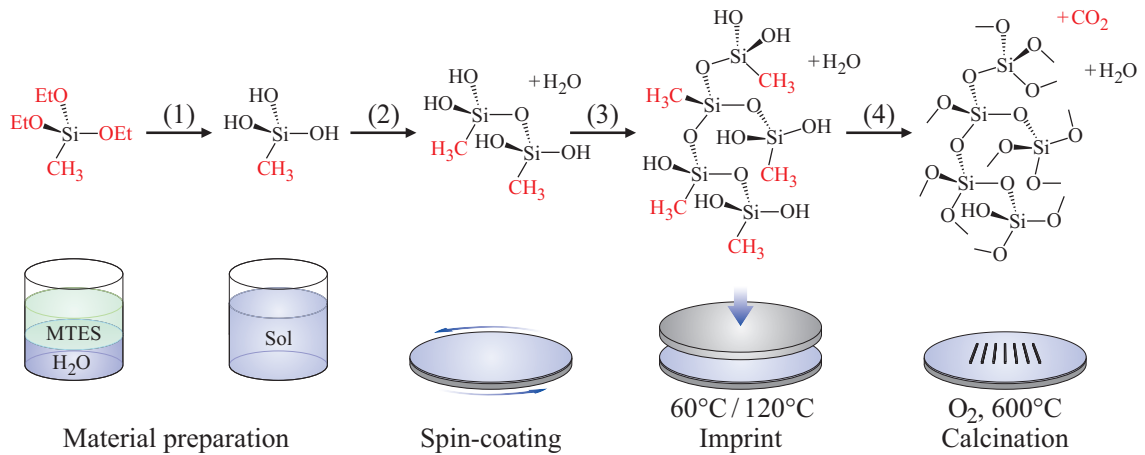


Figure 4.2: The chemical structure of the sol-gel material is shown at the different stages of the imprint process. (1) hydrolysis, (2) condensation and gelation, (3) condensation during imprint, and (4) calcination of organics during thermal annealing.

4.2.1 Fabrication of nanochannels

Figure 4.4 shows a selection of different methods for fabrication of fluidic nanochannels. Nanofluidic lab-on-a-chip devices for DNA-analysis have conventionally been fabricated by top-down planar processing of fused silica [7, 87–91] or silicon [92, 93] substrates due to high quality of processing and low autofluorescence of the materials [21]. Anisotropic etching of fused silica or silicon provides very good dimensional control, but most of the required lithography and etching techniques are expensive high-vacuum processes, and many process steps are needed to produce nanofluidic channels of different depths in the same device.

Polymer devices for DNA-analysis have been made by imprint lithography [59] and injection molding [94], and elastomeric PDMS devices have been made by casting [95]. These fabrication processes have the advantage of enabling channels of different depths to be produced in a single process step, requiring only subsequent bonding of a lid to complete the device. Easy fabrication and low-cost materials make such nanofluidic devices very cheap to produce, but swelling and deformation of the soft materials during bonding reduce the control of channel dimensions [21, 96–99].

For fluorescent imaging of single molecules, silica devices have a number of advantages compared to similar devices fabricated in polymer: The low autofluorescence of the device material increases the fluorescence signal-to-noise ratio [104, 105], possibility of fusion bonding enables accurate control of channel dimensions [106], and the high stability and the hydrophilic character of silica make the devices compatible with numerous chemicals used in biology. Silica surfaces are therefore easily functionalized by grafting organic compounds, enabling control of the adhesion of biomolecules [107].

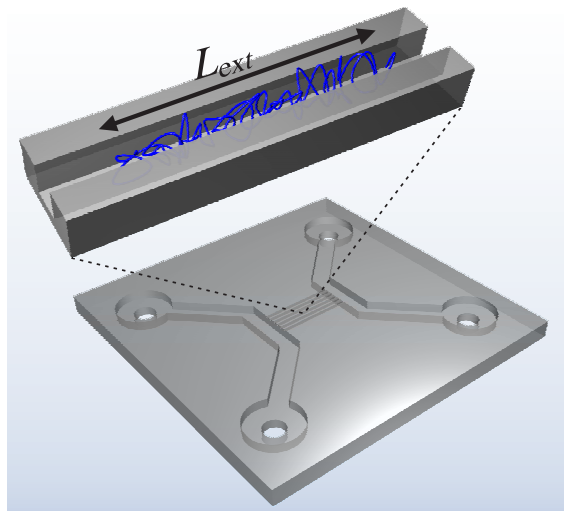


Figure 4.3: Cartoon of the fluidic device. Microchannels lead from four inlet holes to the array of nanochannels in the center. Confined in the nanochannels, DNA molecules stretch to the length L_{ext} along the channel. Figure from Paper 1.

4.3 Nanofluidic sol-gel silica devices - results from Paper 1

By introducing sol-gel materials for fabrication of lab-on-a-chip devices, it is possible to get the best from both silica and polymer fabrication technologies: Through imprint of a sol-gel silica material, all-silica fluidic devices, featuring both micro- and nanochannels, can be fabricated in a single process step without use of any high-vacuum processes. Calcination of the imprinted sol-gel material produces purely inorganic silica, which has very low autofluorescence, see Fig. 4.5, and can be fusion bonded to a glass lid. Compared to top-down planar processing of silica or silicon substrates, sol-gel nanoimprint drastically reduces the number of process steps, and thus the fabrication costs, while preserving the excellent material properties of silica.

4.3.1 Imprint process

The process for imprint of sol-gel material was developed based on previous works in which MTES precursors were used [58, 86, 108]. As mentioned in Sec. 4.1, permeable PDMS stamps are typically used for imprint of sol-gel materials. However, the flexibility of a PDMS stamp causes pronounced bending of the stamp at interfaces between micro- and nanostructures [37]. As described in the supplementary information of Paper 1, see App. C, for fabrication of the nanofluidic device, severe stamp bending resulted in uneven imprinted surfaces that could no be bonded to a lid.

For the fabrication by nanoimprint of a fluidic device featuring both micro- and nanochannels, it was therefore necessary to develop a process for imprinting of sol-gel material with a rigid silicon stamp. As shown in Fig. 4.2, water is released during the condensation reaction. Due to the non-permeability of silicon, the water vapor produces

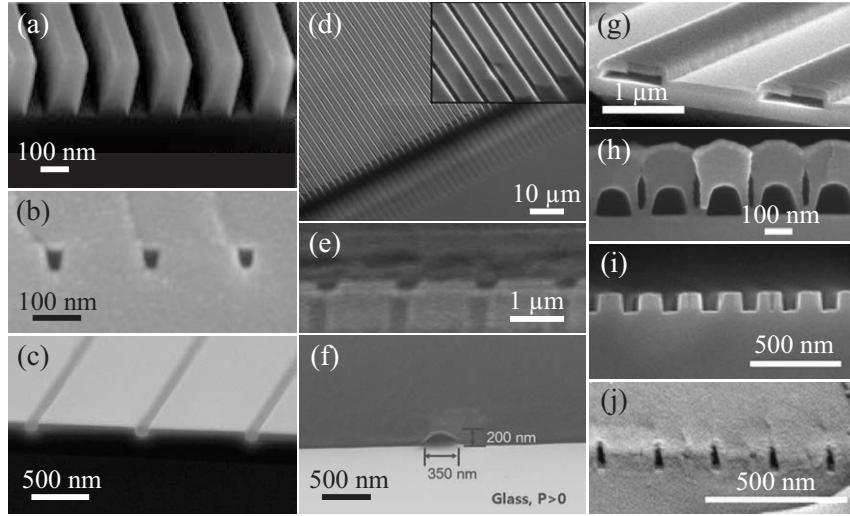


Figure 4.4: SEM images of examples of fluidic nanochannels fabricated using (a–c) reactive-ion etching (RIE) and silica fusion bonding, (d–f) polymer imprint/molding and thermal bonding, and (g–j) sacrificial polymer/RIE and SiO_2 -deposition. (a) Fused silica nanochannels made by NIL and RIE [7]. (b) Fused silica nanochannels made by RIE-etching and fusion bonding [100]. (c) RIE-etched channels in thermally grown SiO_2 on silicon substrate [101]. (d) Micro- and nanochannels hot-embossed in thermoplastic polymer [59]. (e) Nanochannels made by injection molding and thermal polymer bonding [94]. (f) Nanochannels created by controlled collapse of elastomeric PDMS during bonding to glass substrate [97]. (g–h) Sacrificial polymer nanochannels covered by PECVD deposition of SiO_2 and thermally decomposed at 440°C [102]. (i–j) RIE-etched silica nanochannels sealed by angled deposition of SiO_2 [103].

defects in the imprinted surface as described in the supplementary information of Paper 1, see App. C. However, it was found that a reduction of the water content by storage in nitrogen atmosphere and thermal pre-treatment of the sol-gel material before imprint solved the problem. The decreased water content is seen in the FTIR spectrum in Fig. 3.7. Fast storage in dry nitrogen atmosphere appeared to be crucial for the reproducibility of the imprint process.

As explained in the previous chapter, heating of the gel film increases the condensation rate. The thermal pre-treatment, which is necessary in order to avoid defects from water vapor, thus increases the material viscosity, which must be low in order for good imprints to be made. The solution to this problem was imprinting at increased temperature, 60°C in stead of room temperature, in order to use the thermoplastic properties of the gel, see Sec. 3.2.5. At 60°C , however, the condensation rate is still low enough [86] to allow the gel time enough to flow into the cavities of the stamp.

Using a multi-level, rigid silicon stamp, as presented by Thamdrup *et al.* [59], stamp bending was reduced and very good replication of both micro- and nanostructures with uneven density of pattern features was obtained as shown in Fig. 4.6. Fluidic channels of different depths can thus be produced in a single process step. After imprint, annealing of the structured sol-gel material at 600°C in oxygen atmosphere calcinates the organics and

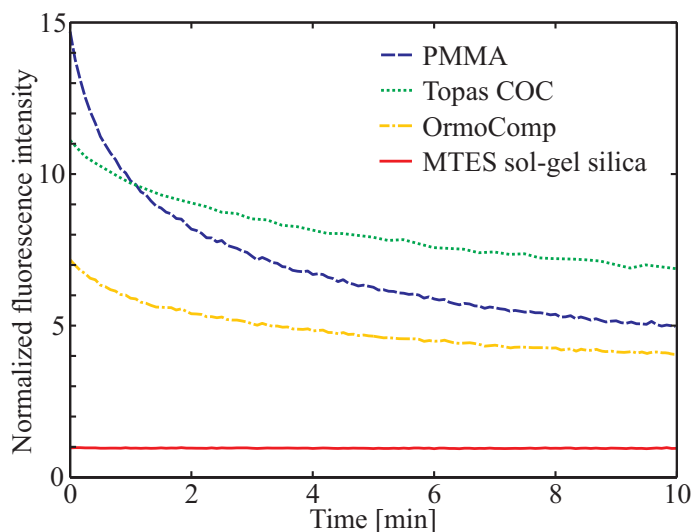


Figure 4.5: Autofluorescence as function of time for 300 nm films of PMMA (75k, Micro Resist Technology), Topas (cyclic olefin copolymer, grade 9506, Topas Advanced Polymers), OrmoComp (Micro Resist Technology), and annealed MTES sol-gel silica on fused silica substrates. Fluorescence intensities were measured using a FITC filter cube, see Paper 1, and are normalized to that of a clean fused silica substrate. High levels of fluorescence intensity with a decrease over time, *i.e.*, bleaching, are seen for the organic and hybrid materials. In comparison, the annealed sol-gel silica film has a constant level of autofluorescence, identical to that of the substrate alone. Figure from Paper 1.

produces a purely inorganic silica material, which can be fusion bonded to a thin glass cover slip to seal the channels. A detailed description of the imprint process is found in Paper 1, see App. B.

4.3.2 Device assembly

After annealing of the imprinted sol-gel silica, the nanofluidic device is assembled as sketched in Fig. 4.7. The inlet holes are made by powder blasting with $110\ \mu\text{m}$ Al_2O_3 particles through a mask of self-adhesive tape [106]. The channels are sealed by a $157\ \mu\text{m}$ thick polished cover slip, which is fusion bonded to the imprinted surface [109]. Figure 4.8 shows optical images of the final device together with SEM images of the fabricated nanochannels. A SEM image of a bonded silica nanochannel of approximately $390\ \text{nm}$ by $170\ \text{nm}$ cross-sectional dimensions, which was produced by imprint of a $150\ \text{nm}$ by $170\ \text{nm}$ stamp protrusion, is shown in Fig. 4.8e.

In order to show that the sol-gel silica device is suitable for studies of DNA molecules, experiments with DNA confined in the fabricated nanochannels were performed. These experiments are described in Sec. 5.3.

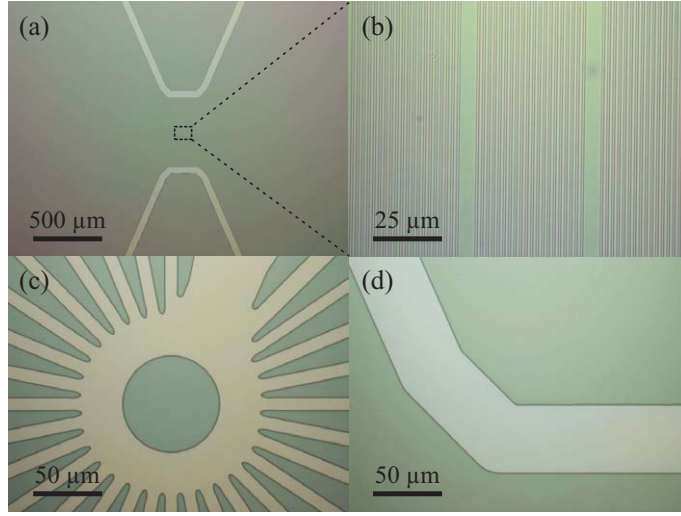


Figure 4.6: Microscope images of (a) inlet channels and (b) nanochannels imprinted in sol-gel silica using multi-level stamp. (c-d) Details of inlet structures imprinted using silicon stamp. Figure from Paper 1.

4.3.3 Material deformation during annealing

The examples of previous works on sol-gel imprint shown in Fig. 4.1 have in common that free-standing nanostructures with a high density of free surfaces were produced. For imprinted channel structures, however, the free-surface density is very low, and this has a considerable impact on the structure deformation that takes place during the calcination process. This is shown in Fig. 4.9, where 100 nm wide, 100 nm high protrusions with a period increasing from 145 nm to 3 μm were imprinted in a 700 nm sol-gel silica film. The SEM images in the top panel show cross-sections of the resulting channel structures after calcination, and it is seen that channel width depends strongly on the structure period. For structures of small period, where the density of free surfaces is large, deformation is small and a high degree of dimensional control is maintained during the annealing. For structures of large period, where the density of free surfaces is small, the deformation is much more pronounced, and the produced channels are considerably wider than the stamp protrusion. The bottom panel of Fig. 4.9 shows the channel widths measured at top and bottom as function of the period. It is seen that the data are excellently fitted by error functions, as shown by the dashed lines in the graph. For periods larger than 1.5 μm, the channel width is constant. The deformation of the gel during calcination is further described in the supplementary information of Paper 1, see App. C.

4.4 Chapter summary

In this chapter, a process for fabrication of micro- and nanofluidic silica devices by nanoimprint of a sol-gel material was presented. Using a multi-level stamp, channels of different depths were produced in a single process step and costly high-vacuum processes, such

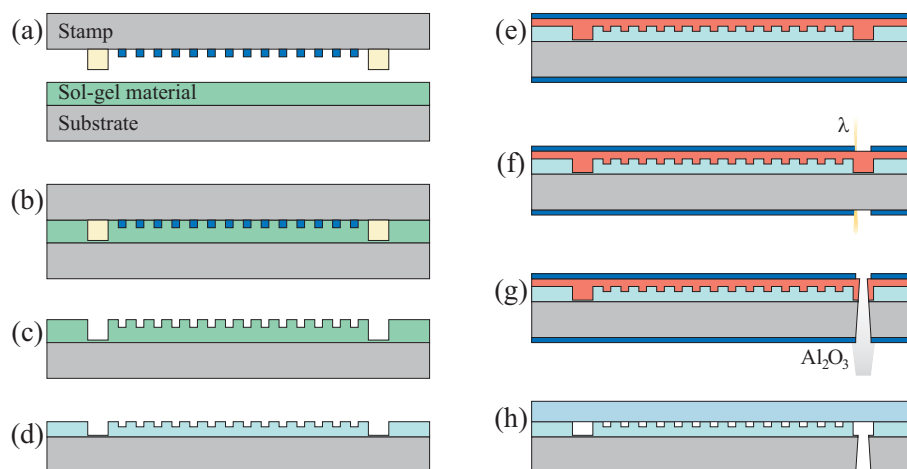


Figure 4.7: Cross-sectional sketches of the process flow. (a) Imprint of multi-level hybrid stamp in spin-coated gel film. (b) Heating during imprint to cross-link the gel material. (c) Demolding of stamp. (d) Thermal annealing of gel at 600°C in oxygen atmosphere calcinates organics and produces pure silica. (e) Spin-coating of protective resist layer and application of self-adhesive masking tape (Nitto, SWT-20). (f) Laser marking tape using CO_2 -laser. (g) Powder blasting of inlet holes using $110\ \mu\text{m}$ Al_2O_3 particles [106]. (h) The sol-gel silica chip and a $157\ \mu\text{m}$ thick cover slip are cleaned in RCA 1 and RCA 2, whereby the surfaces are activated by hydroxyl groups. When pressed together, the imprinted sol-gel silica surface and the cover slip will spontaneously bond together. Subsequent thermal annealing strengthens the bonding [109].

as electron beam lithography and reactive-ion etching, were avoided. This makes the fabrication much simpler and cheaper than top-down processing of fused silica or silicon substrates. Annealing of the imprinted hybrid sol-gel material in oxygen atmosphere produced a purely inorganic silica material, which had very low autofluorescence and could be fusion bonded to a glass lid.

A rigid stamp was required in order to imprint both micro- and nanostructures, and due to the release of water during condensation of the sol-gel silica, a novel process had to be developed, in which the water content was reduced before imprint, to allow imprint with a non-permeable silicon stamp.

Using this imprint process, high-quality, bonded silica nanochannels of $390\ \text{nm}$ by $170\ \text{nm}$ cross-sectional dimensions were produced. It was found that the deformation of imprinted structures during annealing depends on the periodicity of the channels in a way that is well described by an error function. For structures of small periodicity, and hence high density of free surfaces, a high degree of pattern fidelity was observed. However, for bonding of the imprinted device, a certain periodicity of the channels is required, which puts a limit to how small channels can be produced. For use of sol-gel material in fluidic devices, cracking of films thicker than approximately $400\ \text{nm}$ put constrictions on the design regarding channel depth. Extension measurements of DNA molecules confined in the fabricated nanochannels are presented in the following chapter.

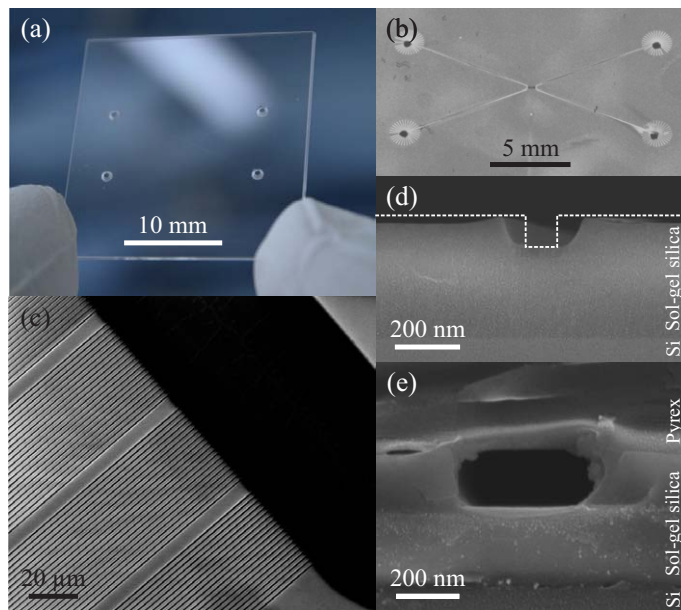


Figure 4.8: Bonded sol-gel silica device on (a) fused silica substrate and (b) silicon substrate. $50\ \mu\text{m}$ wide inlet channels lead from powder-blasted inlet holes to the nanochannel array in the center. (c) SEM image of imprinted and calcinated sol-gel silica device. Interface between inlet channel and arrays of imprinted nanochannels is shown. (d) Cross-sectional SEM image of imprinted and calcinated sol-gel silica nanochannel. Dashed line show cross-sectional profile of the imprinted $100\ \text{nm}$ stamp protrusion for comparison. (e) Cross-sectional SEM image of sol-gel silica nanochannel, approx. $390\ \text{nm}$ by $170\ \text{nm}$ dimensions, bonded to a pyrex lid. The bonded device was cut with a saw, causing some material smear. A thin layer of gold was sputtered on samples before SEM imaging. Figure from Paper 1.

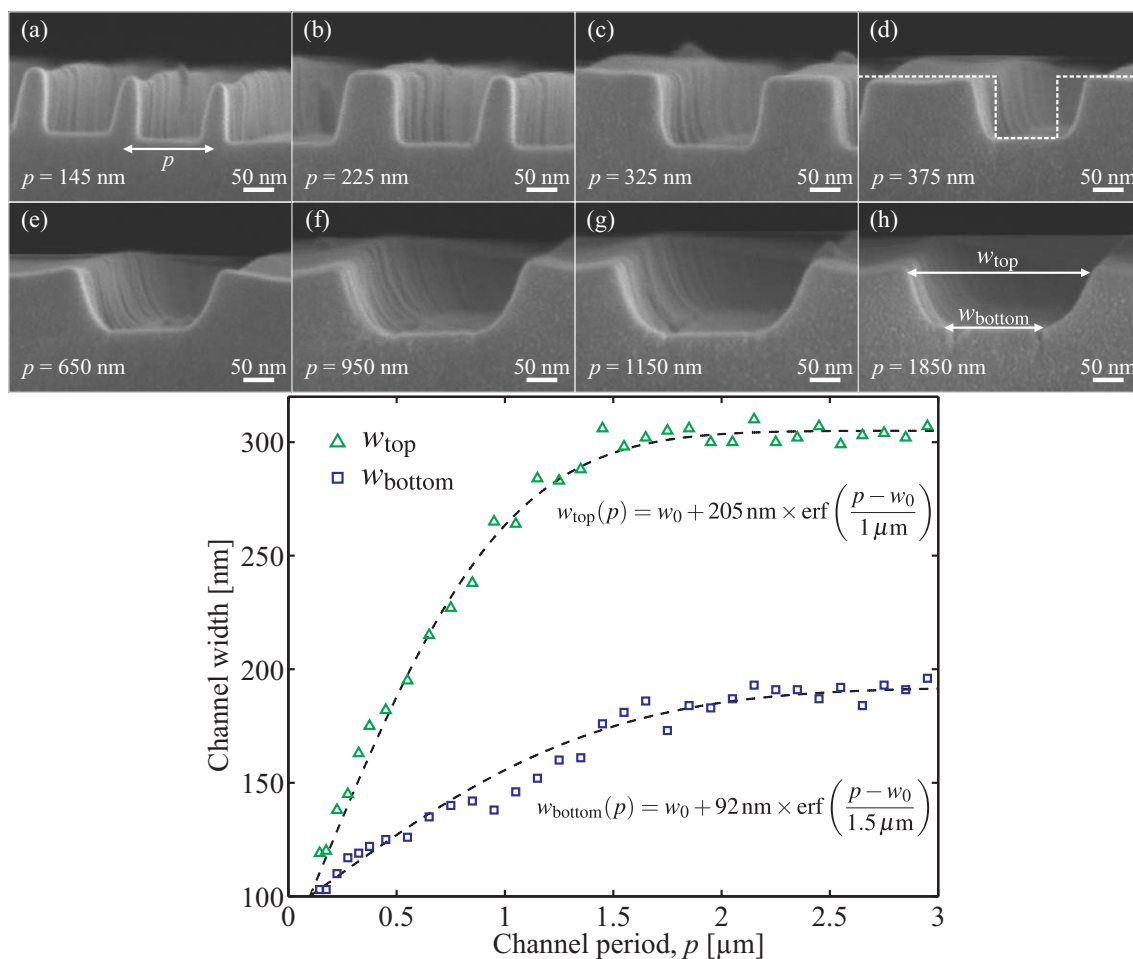


Figure 4.9: SEM images (a-h) show cross-sectional views of calcinated imprints of $w_0 = 100$ nm wide, $h_0 = 100$ nm deep structures with increasing period p from (a) through (h). Dashed line in (d) shows cross-sectional profile of the stamp structure for comparison. The width of imprinted channels is seen to depend strongly on the period due to the deformation of sol-gel silica that takes place during the annealing process. The graph shows values of w_{top} and w_{bottom} , measured on the SEM images, as indicated in (h). The data are excellently fitted by the inserted error functions, which are shown with dashed lines. Figure from Paper 1.

Chapter 5

DNA in nanoconfinement

5.1 Introduction to DNA

The information that governs the production and folding of proteins in living organisms is stored in the cell nucleus in long polymeric chains called deoxyribonucleic acids (DNA). Double-stranded DNA consists of two negatively charged phosphate backbones that are intertwined in a double helical structure, and on each of the backbones, four different bases, or nucleotides, adenine (A), thymine (T), cytosine (C), and guanine (G), are bound in a specific sequence. The two backbones are kept together by the bases, which pairwise bind together by hydrogen bonds, forming a basepair (bp), such that A always binds to T, and C binds to G. The sequences of bases on the two backbones are therefore complementary. Consisting of up to several hundred million basepairs, DNA molecules can have lengths of the order of centimeters while the width is only $w_0 = 2$ nm. The total length of the human genome is approximately 1.8 m, but coiled up and compacted in chromosomes, it fits into the cell nucleus.

Knowledge of the base sequence of a specific DNA molecule provides information that can be used, e.g., for diagnosing diseases [110], detection of bacteria or viruses [111], or even understanding of the functioning of proteins [112], and it is therefore highly valuable information.

5.1.1 DNA sequencing and separation

Sanger sequencing [113], developed in 1977, was the first method for fast reading of the sequence of bases in DNA molecules. Using repeated DNA polymerase, this method results in four solutions of DNA fragments of varying length, one solution for each of the four bases. Size-separation of these fragments, with a resolution of a single basepair, is performed using gel electrophoresis [114], in which the charged molecules are electrophoretically transported through a gel. Molecules of different lengths have different mobilities, and based on the positions of DNA fragments in the gel after a given time, the length of the fragments, and hence the base sequence can be constructed. Size-separation for measuring lengths of DNA fragments is thus an essential tool in DNA analysis.

Polymerase is performed during continuous thermal cycling between three different

temperatures [115], which is slow unless very small sample volumes are used, and gel electrophoresis is only suitable for relatively short DNA fragments. This complicates and slows down the sequencing process. Though sequencing techniques have been optimized and automated, the sequencing speed is only a few Mbp per day, and sequencing of the entire human genome thus takes approximately one year [116]. In order to unleash the enormous potential of the information hidden in DNA, the sequencing speed thus constitutes an important bottleneck.

5.1.2 Lab-on-a-chip systems for DNA analysis

The problem of increasing sequencing speed has been approached in several different ways. Sanger sequencing in a microfluidic chip has been demonstrated by Blazej *et al.* [117]. In the microfluidic chip, very low reaction volumes make thermal cycling fast, and correspondingly low consumption of chemicals makes sequencing cheap. On-chip gel electrophoresis was used for separation. While this device may not improve the speed for sequencing of entire genomes, it may serve as a point-of-care system for fast detection of very specific DNA sequences, which is very useful in diagnostics.

In order to improve separation, nanofabricated 'artificial gels' can be made in lab-on-a-chip devices, which essentially constitutes a nano-sized obstacle course that provides size-based separation of DNA and proteins in a continuous-flow by entropic trapping [92, 93, 118, 119]. The advantage of a designed nanotopography, compared to the randomly oriented gel network, is that the nanofabricated structures can be tuned to a specific application, such that fast separation of molecules in any size-range can be performed. Gel separation works primarily for short DNA molecules (< 40 kbp) [92].

In this chapter, such a nanofluidic separation device is presented, which provides both size- and topology-dependent separation of DNA molecules.

Confinement of DNA in nanochannels also provides a platform for analysis of single molecules [14]. This has the advantage that time consuming amplification [115] of the DNA is not necessary, since information can be extracted from a single molecule. By stretching of genomic length DNA in nanochannels, Tegenfeldt *et al.* [7] demonstrated fluorescence-based single-molecule sizing with a resolution of a few hundred base pairs obtained within a minute.

In this chapter, such DNA sizing is described in Sec. 5.3, where DNA molecules of different lengths are stretched in the nanochannels of the sol-gel silica device presented in Chap. 4.

In single-molecule studies of confined DNA, information of the base sequence can be extracted, e.g., by restriction mapping [88], where restriction enzymes are used to cut the DNA strand at locations where specific sequences occur. The number of cut sites and their position can then be determined due to the linear mapping of contour along the confinement-stretched molecule. Another way of mapping the positions of specific sequences is enzymatic fluorescent labeling [120], where fluorescent enzymes bind to specific sites, which then become visible in a fluorescence microscope. Furthermore, denaturation mapping [90], in which the local concentration of A-T and C-G basepairs is fluorescently monitored, can be used to create a molecular barcode. These methods do not provide

the complete sequence of DNA, but they produce molecular fingerprints, which enable recognition of specific molecules. This may be very useful in diagnostics.

A method that may have the potential to enable direct reading of the base sequence of single DNA molecules, is sequencing through a nanopore. During translocation by electrophoresis of a DNA molecule through a nanometer-sized pore, monitoring of the electrical current through the pore could provide a way of probing the sequence of single linear molecules [121–123]. However, sequencing has not yet been demonstrated using this method.

In the development of such platforms, it is important to understand how DNA behaves in confinement. This is described in the following section after a brief introduction to polymer physics.

5.2 Modeling of confined DNA

A DNA molecule can be modeled as a polymer, but while the biological properties of a DNA molecule are very complex, the physical properties involved in the molecule dynamics can be described by only three parameters [124]: contour length L_C , persistence length l_P , and effective width w_{eff} . The contour length is the total length of the DNA molecule when fully stretched, to which each basepair contributes 0.34 nm. The rigidity of a real polymer is defined as the characteristic length scale l_P over which the correlation between the orientation of different parts of the molecule is decreasing [125]. On length scales smaller than l_P , a DNA molecule is considered rigid, while it is considered flexible on length scales larger than l_P . The persistence length of DNA is approximately $l_P = 50$ nm. The intrinsic width of DNA is $w_0 = 2$ nm, but due to the molecule interacting with the solvent surrounding it and repulsion between different parts of the molecule that approach each other in space, an excluded volume around the polymer chain exist, in which other monomers are not allowed to enter. This gives an effective width of the DNA molecule, which is much larger than the intrinsic width. At the experimental conditions used in this project, the effective width is estimated to be $w_{\text{eff}} = 12$ nm. Both the persistence length and the effective width depends on the ionic strength of the buffer solution in which the DNA is found [126].

5.2.1 Freely-jointed chain model

In the simplest model of a polymer, the chain is modeled as a number of rigid links connected by freely jointed hinges, see Fig. 5.1. However, for such a simple model to fit a real polymer, the length of the rigid links must be adjusted to capture the rigidity of the polymer. An equivalent chain is therefore constructed, where sections of the chemical monomers are substituted with rigid Kuhn segments of length b . For a semiflexible DNA molecule, the Kuhn length is twice the persistence length, $b = 2l_P \approx 100$ nm.

As sketched in Fig. 5.1, the total number of $N + 1$ monomers in the equivalent chain are connected by N freely jointed hinges of length b to form a linear polymer with contour length $L_C = Nb$. The hinges are allowed to rotate and bend at any angle, and any difference in probability of different torsion and bending angles is ignored. Any interactions

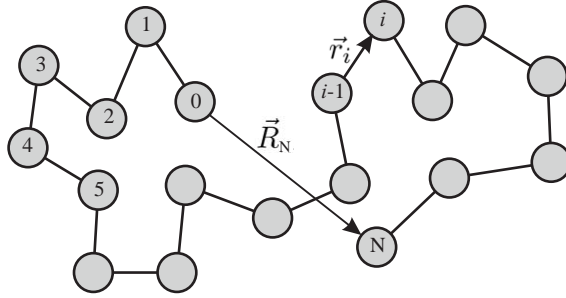


Figure 5.1: Using the freely-jointed chain model, a polymer chain can be described as a random walk with N steps of length b .

between monomers that are far apart along the chain, even if they approach each other in space, are thus ignored. A chain obeying this over-simplified model is not realizable since real chains interact both with the solvent and with themselves. However, the freely-jointed chain model provides a good starting point for the understanding of polymer physics since it allows the polymer polymer conformation to be described by a simple random walk with a step size of b , as sketched in Fig. 5.1.

Most often polymers are not stretched to the full contour length, so the end-to-end distance provides information on the actual size of the molecule conformation. The end-to-end vector of a specific polymer \vec{R}_N is the sum of all the N bond vectors \vec{r}_i in the molecule [125]

$$\vec{R}_N = \sum_{i=1}^N \vec{r}_i. \quad (5.1)$$

When dealing with very long molecules, with a huge number of degrees of freedom, it is useful to treat the behavior by statistical quantities. The mean-square average of all the end-to-end vectors of an ensemble of molecules describes the average polymer conformation and is given as [125]

$$\langle R^2 \rangle = Nb^2. \quad (5.2)$$

The radius of gyration R_g gives a measure of the average extension of a polymer chain, and for an ideal linear chain it is defined as [125]

$$R_g^2 \equiv \frac{1}{N} \sum_{i=1}^N (\vec{R}_i - \vec{R}_{\text{cm}})^2, \quad (5.3)$$

where \vec{R}_i is the position vector of the i^{th} monomer and \vec{R}_{cm} is the position vector of the polymer's center of mass. For an ideal linear chain in a bulk solution, the radius of gyration simplifies to [125]

$$\langle R_g^2 \rangle = \frac{\langle R^2 \rangle}{6}. \quad (5.4)$$

5.2.2 Entropic energy of a polymer chain

In order to introduce the concepts of confinement stretching and entropic trapping, the freely-jointed equivalent chain is used for a short derivation of entropic free energy.

The entropic energy of a polymer is related to the number of possible conformations that the chain can have. A polymer that is stretched to the full contour length will have only one possible conformation, and it thus has a very high entropic energy. When the end-to-end distance of a polymer is lower than the contour length, the molecule can be shaped in many different ways while still having a fixed end-to-end distance, and the entropic energy is low.

Using 3D random walk statistics, the probability distribution for end-to-end vectors \vec{R} can be calculated for $|\vec{R}| \ll L_C$ [125]

$$p_{3D}(N, \vec{R}) = \left(\frac{3}{2\pi Nb^2}\right)^{3/2} \exp\left(-\frac{3\vec{R}^2}{2Nb^2}\right) = \frac{\Omega(N, \vec{R})}{\int \Omega(N, \vec{R}) d\vec{R}}, \quad (5.5)$$

where $\Omega(N, \vec{R})$ is the total number of conformations of a freely-jointed chain of N monomers with end-to-end vector \vec{R} . The integral over $\Omega(N, \vec{R})$ is the total number of conformations for all end-to-end vectors. By applying Boltzmann's law for the entropy S as function of the number of possible conformations $S = k_B \log \Omega(N, \vec{R})$, the entropy of a molecule with a specific end-to-end vector \vec{R} can be found [125]

$$S(N, \vec{R}) = -\frac{3}{2}k_B \frac{\vec{R}^2}{Nb^2} + S(N, 0), \quad (5.6)$$

where $S(N, 0)$ is the entropy of the chain with both ends at the same point. The Helmholtz free energy is given as $F = U - TS$, where U is the internal energy of the system, which for an ideal chain is independent of the end-to-end vector, since the monomers have no interaction energy. The entropic free energy is thus [125]

$$F(N, \vec{R}) = \frac{3}{2}k_B T \frac{\vec{R}^2}{Nb^2} + F(N, 0), \quad (5.7)$$

where $F(N, 0)$ is the free energy of the chain with both ends at the same point. The entropic force required to keep a chain at a fixed end-to-end vector \vec{R} is then [125]

$$\vec{f} = \frac{\partial F(N, \vec{R})}{\partial \vec{R}} = \frac{3k_B T}{Nb^2} \vec{R}. \quad (5.8)$$

The entropic energy scales with the square of the end-to-end vector, and the entropic free energy can thus be considered equivalent to Hooke's law for short end-to-end distances $|\vec{R}| \ll L_C$. The proportionality constant between \vec{f} and \vec{R} is hence called the entropic spring constant.

In conclusion, it is seen that by deformation of a polymer from its equilibrium state, the free energy is increased, and deformation from the equilibrium conformation thus requires a force. Equally, when a DNA molecule is confined to a space smaller than its bulk conformation, the free energy of the molecule is increased.

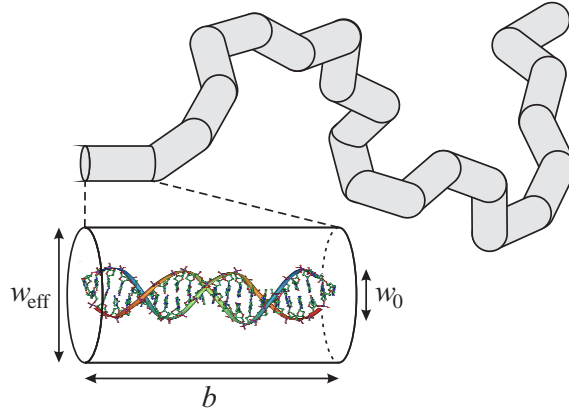


Figure 5.2: DNA modeled as a series of N connected Kuhn segments of length b . The segments have an effective width w_{eff} , which is larger than the intrinsic width w_0 , due to electrostatic effects and self-exclusion.

5.2.3 Excluded volume interactions

As mentioned in the beginning of the chapter, a real polymer chain will take up a finite volume of space. In contrast to the freely-jointed polymer model, the real monomers occupy an excluded volume around themselves where other monomers cannot enter due to steric hindrance and electrostatic repulsion. In the Flory model [125, 127], this is modeled by assigning an effective width w_{eff} to the polymer, as illustrated in Fig. 5.2. When taking self-interaction into account, the polymer radius is given by

$$R_g \simeq (l_p w_{\text{eff}})^{1/5} L_C^{3/5}. \quad (5.9)$$

The electrostatic interactions between different segments of the polymer chain depend on the ionic strength of the buffer in which the molecule is found. In a buffer solution, the intrinsic charge of a polymer chain is screened by counter-ions over a characteristic length scale, the Debye length. At low ionic strength, the Debye length is large, and self-avoidance is increased. This results in an increased effective width w_{eff} [126]. In the $0.5\times$ TBE buffer used in this work, w_{eff} is estimated to be 7.4 nm [59].

5.2.4 Confined polymers

In confined spaces, where the dimension D of the confining structures is smaller than R_g , the number of available configurations for a polymer chain is reduced. This leads to an increase in the free energy ΔF , as explained in Sec. 5.2.2. Depending on the size of D in relation to persistence length l_p , two confinement regimes have been shown to exist [100].

In the limit of $D \gg l_p$, a molecule is free to coil in the nanochannel, see Fig. 5.3a, and the molecule conformation stretches due to excluded volume interactions between parts of the molecule that are largely separated along the contour. This limit was described by de Gennes [128], and is known as the de Gennes regime. In this regime of D , coiling of the molecule may be envisioned as being broken up into a series of *blobs*, as illustrated in

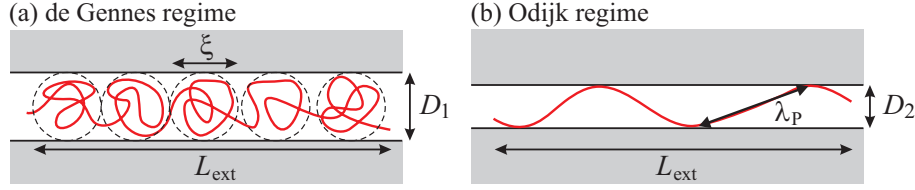


Figure 5.3: (a) In the de Gennes regime, the channel dimension $D_1 \gg l_p$ is large enough for the molecule to be able to make several loops. This can be envisioned as coiling of the molecule to form adjacent blobs of size ξ in the channel. (b) In the Odijk regime, the stiffness of the molecule prevents it from looping in the channel of dimension $D_2 \ll l_p$. The length of an Odijk segment λ_p is the average length between the deflections of the molecule.

Fig. 5.3a. Inside each blob, the confinement force is only a weak perturbation, and the polymer retains bulk properties, but for length scales larger than the blob diameter ξ , the molecule acts as a string of independent blobs. The extension of the molecule L_{ext} is the number of blobs times the blob extension and, using the Flory description of the polymer, de Gennes found that

$$L_{\text{ext}} \simeq L_C \left(\frac{w_{\text{eff}} l_p}{D_{\text{av}}^2} \right)^{1/3}, \quad (5.10)$$

where $D_{\text{av}} = \sqrt{hw}$ is the geometrical average of the height h and width w of a nanochannel. The confinement free energy is of the order of $k_B T$ per blob [128]

$$\Delta F \simeq k_B T \frac{L_{\text{ext}}}{\xi} \simeq k_B T \frac{(w_{\text{eff}} l_p)^{1/3}}{D_{\text{av}}^{5/3}} L_C. \quad (5.11)$$

In the limit of $D \ll l_p$, confinement is very strong due to the rigidity of the molecule on the length scale smaller than l_p , and the molecule is not able to loop in the nanochannel, see Fig. 5.3b. This limit was described by Odijk [129], and is thus known as the Odijk regime. In this regime of D , the molecule is stretched due to the deflection of the molecule on the channel walls. The average length between these deflections is of the order of the Odijk length $\lambda_O \simeq (D^2 l_p)^{1/3}$ [129]. The extension along the channel of each segment is given by $\lambda_O \cos \theta$, where θ is the angle between the channel wall and the deflected segment. By Taylor expansion of the cosine [130], it can be shown that the extension of the molecule is

$$L_{\text{ext}} = L_C \left[1 - \beta \left(\frac{D}{l_p} \right)^{2/3} \right], \quad (5.12)$$

where β is a proportionality factor. In a rectangular channel it has been estimated to 0.36 [100]. The energy is of the order of $k_B T$ per Odijk segment

$$\Delta F \simeq \frac{k_B T}{l_p^{1/3} D^{2/3}} L_C. \quad (5.13)$$

Figure 5.4 shows experimental work by Reisner *et al.* [100] where the extension of DNA was measured in nanochannels of different dimensions. In the region of $60 \text{ nm} <$

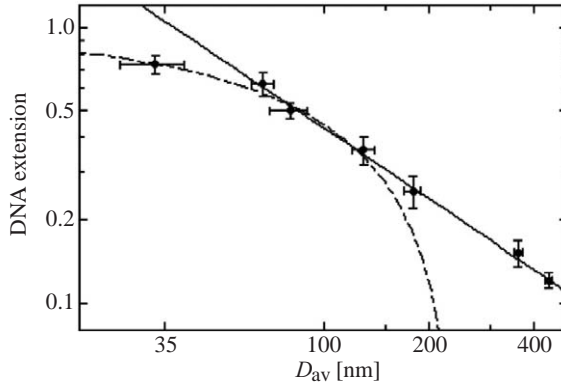


Figure 5.4: Log-log plot of relative extension $L_{\text{ext}}/L_{\text{dye}}$ of λ phage DNA as function of channel dimension D_{av} . The solid line shows a power-law fit to the de Gennes relation Eq. 5.10, resulting in an exponent of 0.85 ± 0.05 instead of $2/3$. The dashed line shows a fit of the Odijk relation Eq. 5.12 with $\beta = 0.36$ and $l_p = 52 \pm 5$ nm. Figure from Ref. [100].

$D_{\text{av}} < 140$ nm, both the de Gennes (Eq. 5.10) and the Odijk (Eq. 5.12) models apply to the experimental data. Below 60 nm, only Odijk theory applies, and above 140 nm, only de Gennes theory fits. The behavior at the cross-over between the de Gennes and Odijk confinement regimes is thus shown.

5.3 Extension measurements

In Eq. 5.9, it was found that DNA in bulk solution coils up in a spherical conformation with a characteristic radius of gyration R_g proportional to $L_C^{3/5}$. For λ phage DNA (48.5 kbp) in $0.5 \times$ TBE buffer, $R_g \approx 1.3 \mu\text{m}$. In this spherical conformation, it is difficult to extract precise information on contour length, and mapping of specific sequences in the molecule is not possible due to the random coiling. Confined in a nanochannel, however, the average extension of DNA along the channel scales linearly with L_C , according to Eqs. 5.10 and 5.12. By elongation of the single molecule, it is possible to measure the contour length with much higher precision using optical techniques. Furthermore, the stretching establishes a one-to-one mapping between the spatial position along the polymer and the position within the molecule [7], which enables optical mapping of the positions of specific sequences in the molecule [88, 89]. An advantage of stretching DNA using confinement is that the molecule remains in its equilibrium configuration, and the presence of a known external force is not required [7]. This facilitates continuous measuring of the extension length L_{ext} .

Thermal fluctuations will cause the molecule extension to vary around the average extension $\langle L_{\text{ext}} \rangle$ with a standard deviation, which for the de Gennes regime is given by [7]

$$\sigma_{\text{ext}} \simeq \sqrt{\frac{4L_{\text{dye}}}{15} (w_{\text{eff}} P_{\text{dye}} D)^{1/3}}. \quad (5.14)$$

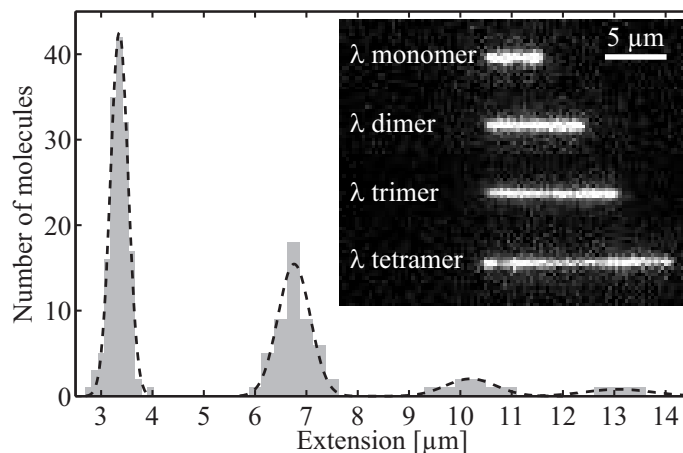


Figure 5.5: Histograms of measured average extension of concatemers of λ phage DNA in sol-gel silica nanochannels. Dashed lines show Gaussian fits. Each measurement is based on 500 fluorescence images recorded at a frame rate of 10 Hz. Monomers (48.5 kbp, 156 molecules) are stretched to $\langle L_{\text{ext},1\lambda} \rangle = 3.37 \pm 0.17 \mu\text{m}$, dimers (97.0 kbp, 50 molecules) to $\langle L_{\text{ext},2\lambda} \rangle = 6.76 \pm 0.31 \mu\text{m}$, trimers (146 kbp, 4 molecules) to $\langle L_{\text{ext},3\lambda} \rangle = 10.20 \pm 0.49 \mu\text{m}$, and tetramers (194 kbp, 2 molecules) to $\langle L_{\text{ext},4\lambda} \rangle = 13.09 \pm 0.46 \mu\text{m}$. Fluorescence images of confined concatemers of λ phage DNA are inserted. Figure from Paper 1.

It is seen that an increase in the confinement reduces the fluctuations and thus increases the precision. However, since the uncertainty of the average extension is given as $u(\langle L_{\text{ext}} \rangle) = \sigma_{\text{ext}}/\sqrt{M}$, where M is the number of independent measurements of L_{ext} , it is possible to determine $\langle L_{\text{ext}} \rangle$ with arbitrary precision by continuously measuring the extension over a long time period. Using fluorescence microscopy, Tegenfeldt *et al.* [7] demonstrated measurements of contour length of confined DNA with a standard deviation of 130 nm, corresponding to approximately 400 bp, in 1 min.

5.3.1 Results from Paper 1

As presented in Paper 1, see App. B, DNA molecules were confined in sol-gel silica nanochannels like the one shown in Fig. 4.8e. For this experiment, λ phage DNA (48.5 kbp, New England Biolabs), which has a monomer contour length $L_C = 16.5 \mu\text{m}$, was used. Due to single-stranded complementary segments at the ends of the λ phage DNA, concatemers, which have contour lengths that are multiples of the monomer length, occur naturally in the DNA solution. This enabled measurement of the extension lengths of DNA of different contour lengths.

In order to observe confined DNA using fluorescence microscopy [131], the DNA was fluorescently labeled using the cyanine dye YOYO-1 (Molecular Probes). A YOYO-1 dye molecule binds to DNA by intercalation of two aromatic rings between the basepairs, thereby causing the DNA molecule to extend. At a dye ratio of 1 dye molecule per 5 base pairs, persistence and contour lengths are increased by 24% [59]. For λ phage DNA, the dye-adjusted persistence and monomer contour lengths amounts to $l_{\text{P,dye}} = 62 \text{ nm}$ and

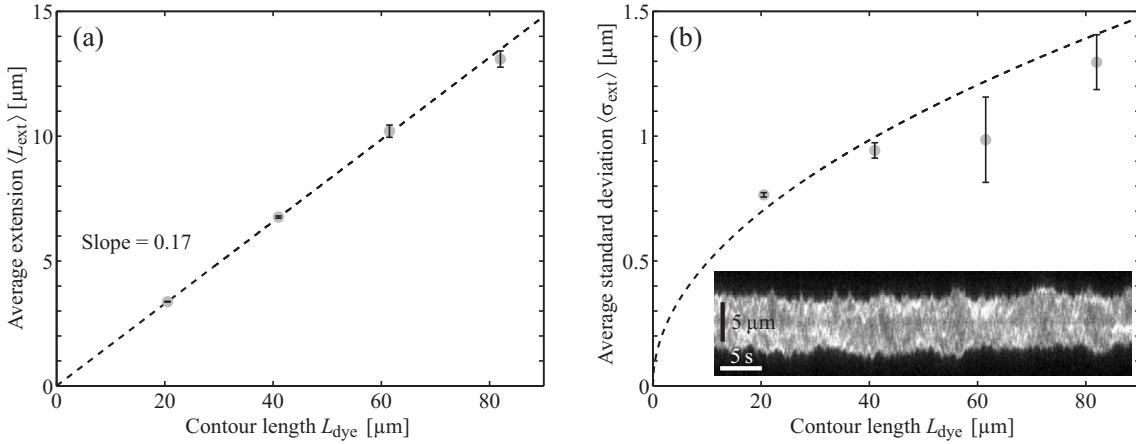


Figure 5.6: Average extension $\langle L_{\text{ext}} \rangle$ of concatemers of λ phage DNA as function of the dye-adjusted contour length L_{dye} . Data from the Gaussian fits in Fig. 5.5. The extension is seen to be 17% of the contour length. Error bars show standard deviation of mean. (b) Average standard deviation $\langle \sigma_{\text{ext}} \rangle$ for the extension measurements of each molecule as function of the contour length L_{dye} . Error bars show standard deviation of the mean. Dashed curve shows a fit of Eq. 5.14 with a prefactor of 1.36. Insert shows time evolution of fluorescence intensity stripe for a λ phage dimer. Figure from Paper 1.

$L_{\text{dye}} = 20.5 \mu\text{m}$, respectively.

The experimental setup for sizing experiments of DNA, as described in App. B, consists of a fluorescence microscope equipped with a cooled EMCCD camera, which recorded movies of the stretched molecules at a frame rate of 10 Hz. In every frame, the molecule extension was measured by fitting a function to the fluorescence intensity profile, as described by Tegenfeldt *et al.* [7].

Figure 5.5 shows histograms of the measured average extension of mono-, di-, tri-, and tetramers of λ phage DNA in sol-gel silica nanochannels of 390 nm by 170 nm cross-sectional dimension. As seen in Fig. 5.6a, the stretching scales linearly with the contour length and corresponds to 17% of the dye-adjusted contour length. This is in good agreement with the 19% stretching predicted by Eq. 5.10. Figure 5.6b shows average standard deviation $\langle \sigma_{\text{ext}} \rangle$ for the extension measurement of each molecule as function of the contour length L_{dye} . The average standard deviation is seen to follow Eq. 5.14 with an additional prefactor of 1.36.

The experiment thus verifies Eqs. 5.10 and 5.14 and it shows that the nanofluidic device described in Chap. 4 is suitable for experiments with confined DNA.

5.4 Entropic trapping and separation

When a DNA molecule is squeezed into confinement, as described in Sec. 5.2.2, the entropy of the molecule is decreased due to the lower number of possible configurations that the molecule can assume, and the decrease in entropy is associated with an increase in free energy.

In a nanochannel with alternating deep and shallow regions, different degrees of confinement will be experienced by a molecule traveling through the channel. This creates a global entropy variation and hence free energy gradients that can trap the molecule in the deep regions. Such traps are called *entropic traps*, since it requires a decrease of the entropy in order to overcome the free-energy barrier and escape into the shallow region. Escape from an entropic trap thus requires an external force, which in a nanofluidic system is most often provided by electrophoresis, which exerts an electric force on the negatively charged molecule, or by pressure-driven flow, which exerts a hydrodynamic drag force on the molecule. Since both forces act on the molecule in the same way, they are considered equivalent [132].

Size-dependent separation of DNA molecules by entropic trapping was first demonstrated by Han and Craighead [133] in a fluidic slit channel with alternating deep ($d_g = 650$ nm) and shallow ($d_s = 90$ nm) regions, through which DNA was electrophoretically driven. A cross-sectional sketch of the device is shown in Fig. 5.8e. The deep channel regions of this device were large enough for the DNA to coil up in its bulk equilibrium conformation with radius $R_g \approx d_g$. In the shallow slits, however, where $R_g > d_s > l_p$, the molecule was confined according to the de Gennes scaling. When no electric field was applied to the device, the molecules were entropically trapped in the deep regions, and as the electric field was increased, the escape probability, and hence the mobility of the molecules, was increased.

For this system, it was shown that the escape rate scales with the number of basepairs in direct contact with the nanoslit [118]. Since the DNA molecule is coiled up in a sphere in the deep region, the number of basepairs abutting the slit scales with the radius of the sphere R_g , which for an ideal chain scales with the square root of the molecule length [119]. Larger molecules thus have increased probability of escaping the traps compared to smaller molecules, since larger coils abut a greater surface of the slit and hence have a greater probability of forming herniations into the slit that lead to escape [118, 119].

Using the device geometry with alternating bulk and de Gennes confinement regions, size-separation of DNA in the 5–164 kbp range was performed [92], and it was demonstrated that an entropic trapping device may work as a fast alternative to pulsed field gel electrophoresis for separation of long DNA molecules.

5.4.1 Results from Paper 2

In Paper 2, see App. D, a device is demonstrated which combines a stretched DNA conformation with entropic trapping. This device consists of an array of 150 nm deep and 75 nm to 600 nm wide nanogrooves in the bottom of an open slit, see Fig. 5.7. The depth of the slit ($d_s = 50$ nm) is less than the groove depth ($d_g = 150$ nm), so that in equilibrium a molecule is both extended along a groove and entropically trapped in it. A pressure-driven buffer flow is used to transport DNA through the device, and as a molecule is only entropically confined in the nanogroove, at sufficient buffer flow, it will be driven out of the groove and into the slit.

By stretching the molecule in front of the nanoslit, the area of the molecule that abuts the slit scales linearly with contour length, according to Eqs. 5.10 and 5.12 and the results

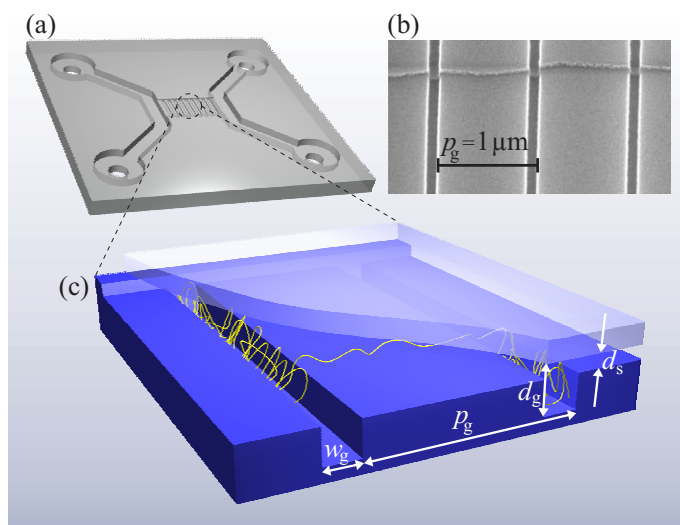


Figure 5.7: (a) Cartoon of the fluidic device showing inlet reservoirs and microchannels leading to the $450\ \mu\text{m}$ long and $50\ \mu\text{m}$ wide nanoslit. (b) SEM micrograph showing edge of nanoslit and transverse nanogrooves. (c) Cartoon of nanogroove channel with stretched DNA being transported from one groove to the next. Slit depth $d_s = 50\ \text{nm}$, groove depth $d_g = 150\ \text{nm}$, groove width w_g is varied from $75\ \text{nm}$ to $600\ \text{nm}$, and periodicity p_g is varied between $1\ \mu\text{m}$ and $2.6\ \mu\text{m}$. Figure from Paper 2.

shown in Fig. 5.6. However, in contrast to what might be expected from the results of Han and Craighead, the stretching does not just lead to a linear scaling of the mobility with contour length. Instead, the extension of the molecule in the entropic trap, gives rise to qualitatively different transport physics. A comparison of the nanogroove device to the device of Han and Craighead is shown in Fig. 5.8.

In the nanogroove geometry, a self-organized dynamical behavior of single molecules is observed in which the DNA molecules alternate between two states of motion: a state where the extended molecule make slow stochastic hops based on escape of its free ends, which we call the 'sidewinder' (Fig. 5.8c–d), and a compact highly folded state where the molecule propagates at constant velocity, which we call the 'tumbleweed' (Fig. 5.8b). Each of these states exhibits a size-independent velocity at fixed buffer velocity, however, longer molecules are more likely to enter the fast tumbleweed state, due to their increased number of degrees of freedom, and the dynamic interplay between the two states thus creates a size-dependent velocity that may be utilized for separation. As shown in Fig. 5.9a, T4 GT7-DNA ($165.6\ \text{kbp}$) propagated with a velocity of up to the order of 500 times faster than λ -DNA ($48.5\ \text{kbp}$) in a nanogroove device of $75\ \text{nm}$ groove width.

An interesting aspect of the nanogroove device is its sensitivity to polymer topology: linear and topologically circular DNA molecules of the same size propagate at different velocities in the nanogroove arrays. This is a feature, which is unique to the nanogroove geometry. As seen in Fig. 5.9b, circular 9-42 charomid DNA ($42.2\ \text{kbp}$) propagated up to 8 times faster than linear molecules of the same contour length.

5.5 Chapter summary

In this chapter, the physics of confined polymers was introduced, and it was explained how the conformation of a DNA molecule is stretched when the molecule is confined in a nanochannel. The stretching enables measurement of the contour length using fluorescence microscopy, as demonstrated using imprinted sol-gel silica nanochannels. This experiment also demonstrated the applicability of the sol-gel silica device for DNA experiments.

The dynamics of linear and circular DNA molecules was studied under pressure driven flow in a slit channel with arrays of transverse nanogrooves. In the nanogrooves, the DNA was both stretched and entropically trapped, and as the buffer flow was increased, escape of the DNA into the slit channel, initiated by either an end or a hernia of the molecule, was enabled. It was found that the molecule transport through the device occurred through two states of propagation: a slow, stepwise groove-to-groove translation called the 'sidewinder' and a fast, continuous tumbling across the grooves called the 'tumbleweed'. Dynamical transitions between the two states cause DNA molecules to exhibit both size- and topology-dependent velocities that may be utilized for DNA separation, molecule filtering, or sample preparation.

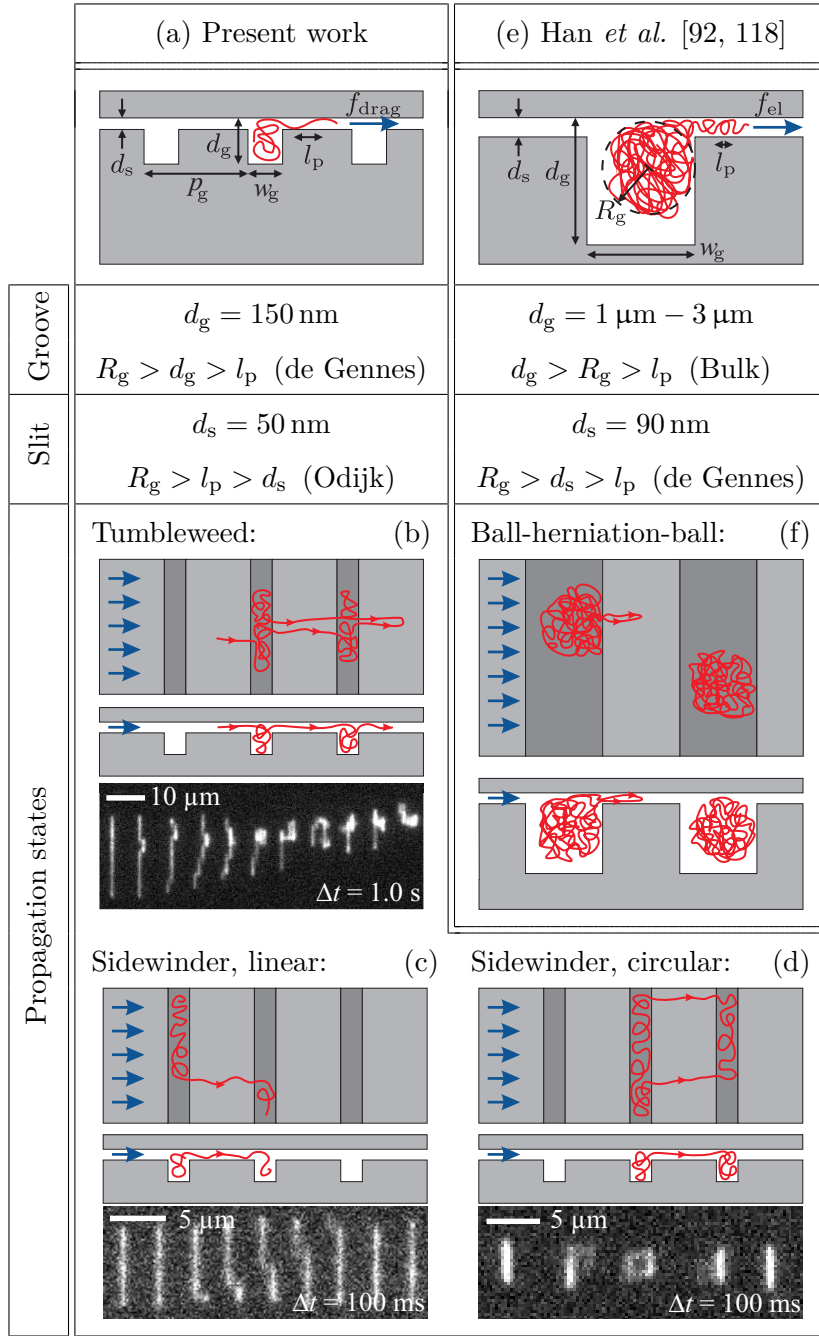


Figure 5.8: Propagation states of DNA in various geometries. Arrowheads on DNA (red lines) indicate direction of motion of DNA that flows in response to buffer flow shown as blue arrows. (a) Alternating de Gennes and Odijk confinement regimes [100] stretch DNA in front of the slit, which gives rise to two distinct propagation states: the folded 'tumbleweed' state (b), and the stretched 'sidewinder' state in case of (c) linear DNA and (d) circular DNA. This contrasts with the single propagation state (f) seen in Han and Craighead's device (e), in which alternating bulk and de Gennes regimes allow DNA to coil in a ball conformation in front of the slit, and transport through the slit is initiated by herniation from the ball. l_p is persistence length and R_g gyration radius. Figure from Paper 2.

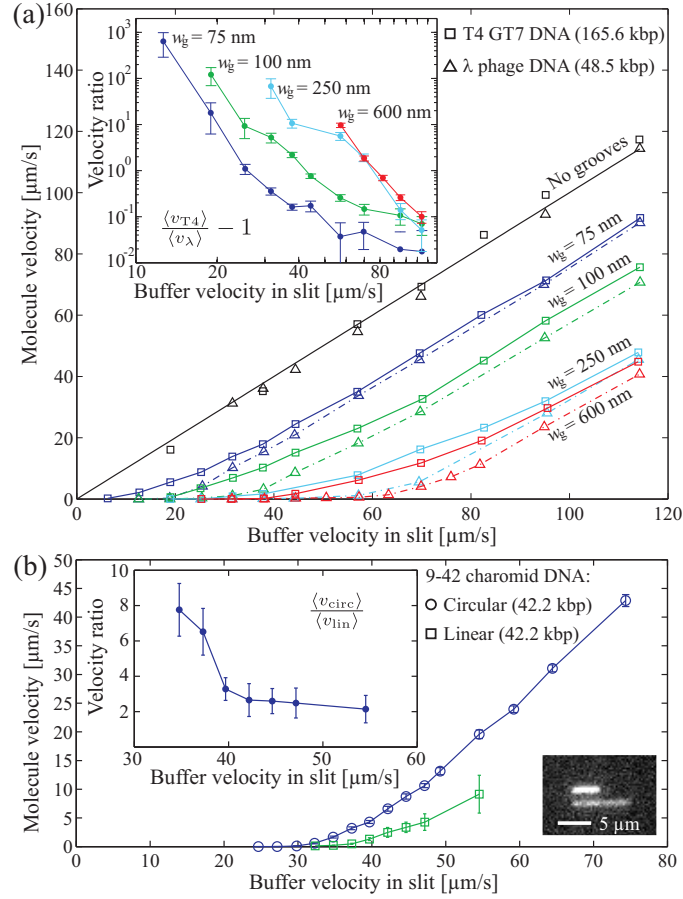


Figure 5.9: (a) Molecule velocity as function of buffer velocity in groove arrays of different width w_g . Groove period $p_g = w_g + 2 \mu\text{m}$. Insert shows velocity ratio between T4 GT7-DNA and λ -DNA $\langle v_{T4} \rangle / \langle v_{\lambda} \rangle - 1$ in a double-logarithmic plot. Velocity ratios of the order of 100 are seen for 75 nm grooves. Data based on movies of 1702 λ -DNA and 1460 T4 GT7-DNA molecules. Buffer velocity measured as the average molecule velocity in a groove-free region of the slit channel. (b) Molecule velocity as function of buffer velocity for circular (intact) and linear (broken once) 9-42 charomid DNA. Fluorescence image shows circular DNA (top) and linear DNA (bottom) trapped in adjacent grooves. $w_g = 100$ nm and $p_g = 2 \mu\text{m}$. Inserted graph shows velocity ratio of circular and linear molecules $\langle v_{\text{circ}} \rangle / \langle v_{\text{lin}} \rangle$. Data based on movies of 479 circular and 69 linear 9-42 charomid DNA molecules. Figure from Paper 2.

Chapter 6

Reconfigurable optically functional surface topography

6.1 Optical reconfigurability by electrophoresis of nanoparticles

As introduced in Chap. 1, the use of fluidics in optical systems makes it possible to reconfigure optical properties [1–5]. Examples of such optofluidic reconfigurability include devices where an electrically controlled refractive index change of liquid crystals is used to reconfigure diffraction gratings or photonic crystals [13, 134–136]. Other examples are reconfigurable gratings made using multiphase droplets in a microfluidic channel [137] and microfluidic gratings that can be reconfigured by exchange of liquids of different refractive index [11].

In this chapter, a reconfigurable optofluidic device is presented, which exploits that the effective refractive index n_{eff} of a solution of sub-wavelength-sized latex particles depends on the particle concentration: At low concentration, the refractive index is close the refractive index of the liquid, whereas, at high concentration, the refractive index approaches that of the particles.

Using charged latex particles, electrophoresis [138, 139] can be used to reversibly collect the particles on a surface, thereby locally increasing the refractive index on the surface. A 4% w/v solution of polystyrene ($n = 1.60$) latex dispersed in water ($n = 1.33$) has effective refractive index $n_{\text{eff}} = 1.34$. If the particles are concentrated, e.g., to 80%, the effective refractive index is locally increased to $n_{\text{eff}} = 1.55$, and tuning of 0.2 refractive index units (RIU) is thus possible.

This principle can be used to reconfigure an optically functional surface topography, such as a grating. Furthermore, if the material of the surface topography is index-matched to the particle solution in either the disperse or the concentrated state, the optical functionality of the surface may be switched on/off. In the case of index-matching, the surface topography is invisible and does not affect the light passing through. When the device is switched, the refractive index at the surface is modulated and the topography becomes optically functional.

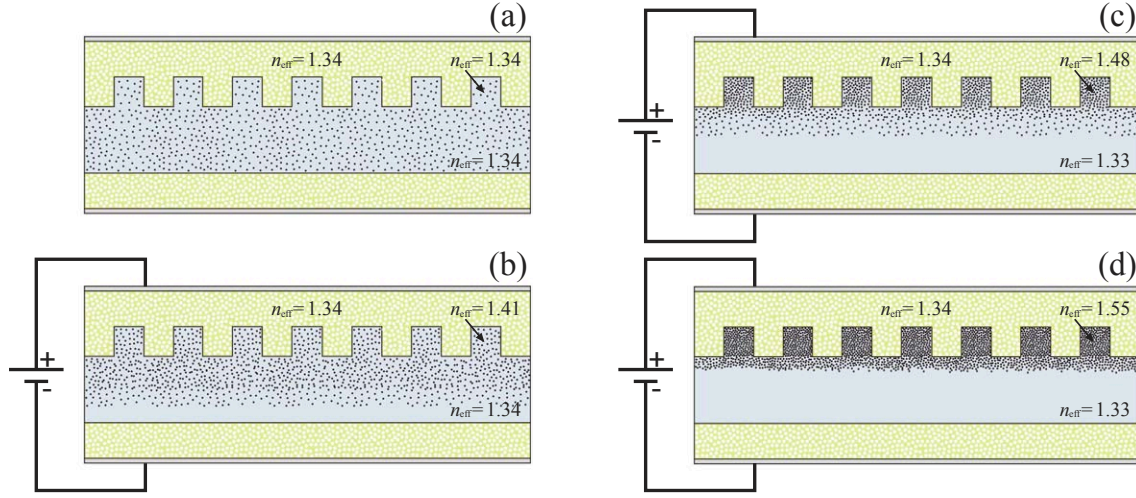


Figure 6.1: Cross-sectional sketch of the reconfigurable device. (a) Off-state. The latex particles are homogeneously dispersed in the liquid, and index-matching makes the grating invisible. (b) An applied potential electrophoretically actuates the negatively charged particles and move them towards the positive electrode behind the structured surface. (c) The refractive index at the surface increases as the particles are concentrated. (d) On-state. The increased refractive index at the structured surface turns on the optical functionality. When the electric field is removed, the particles will diffuse away from the structured surface, and the device returns to the off-state. This is accelerated if the electric field is reversed.

In Fig. 6.1, a *default-off* device is sketched, where the refractive index of a grating is tuned to the disperse particle solution surrounding it. Initially, in the off-state of the device, the refractive index is everywhere the same, and the device has no optical functionality. In the on-state of the device, when a positive potential is applied to the transparent electrode behind the structured surface, the negatively charged latex particles are electrophoretically moved to the surface. Figure 6.1 sketches how the refractive index is locally increased as the particles are concentrated. The index modulation at the structured surface turns the optical functionality of the grating on. Using a low-index diffraction grating fabricated by nanoimprint of sol-gel silica, the functioning of such a device is experimentally demonstrated in this chapter, and the feasibility of the method of tuning an optically functional surface topography by electrophoretic concentration of nanoparticles is shown.

6.1.1 Applications for reconfigurable optical device

Besides the diffraction grating sketched in Fig. 6.1, the method of reconfigurability can be applied to other diffractive surface structures as well, such as a photonic crystal, but it may also work with refractive surface structures, such as a Fresnel lens, a blazed grating, a corner reflector, or a diffusive surface. Furthermore, the optically functional structures may be placed on both electrodes, thus giving the device three different states: Two optically functional states, when the particles are located at either electrode, and an off-

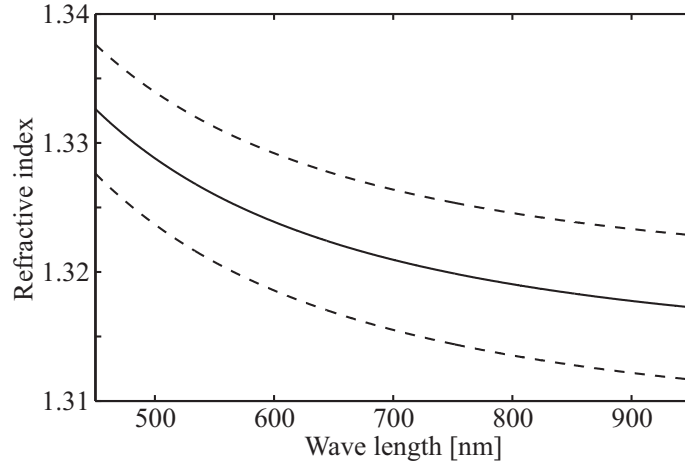


Figure 6.2: Dispersion curve of porous sol-gel silica film made by a precursor mixing ratio MTES:TEOS of 3:2. The film has 25% porosity templated by 77 nm PMMA latex particles. Dashed lines show standard deviation on mean for measurements performed in different locations on the film. Measured by ellipsometry.

state, when the particles are dispersed in the liquid by diffusion. This behavior is unique to this kind of device.

Such reconfigurable optical devices may find use, e.g., in spectrometers, where switching between two grating periods would be possible. Another possible application is reconfigurability of *daylighting* window glass [134, 140–144]. Daylighting windows improve the efficiency of natural lighting in a room by spreading the light going through the window, so that part of the light is redirected to the ceiling and further into the room. For daylighting windows using an optically functional surface topography, the daylighting functionality may be reconfigured or switch on/off.

As it is possible to electrophoretically actuate charged metal nanoparticles [145–147], the principle of the reconfigurable device might also work for making a switchable wire grid polarizer [148], which would be able to switch between two different on-states and an off-state.

6.2 Fabrication of reconfigurable device

The reconfigurable grating device consists of a sandwich structure of glass substrates with transparent electrodes surrounding the optically functional surface topography and the liquid, as sketched in Fig. 6.1.

Since liquids have low refractive indices, addition of a low concentration of polymer particles does not change it much. A *default-off* device thus requires a material with an index comparable to that of liquids. By integrating sub-wavelength structures of low index, e.g. air, in a material of higher index, the effective refractive index of the material can be lowered [24]. Examples of such low-index materials are nanoporous polymers [149, 150], glass nanorods [151], and porous sol-gel silica [25, 152].

Of particular interest is a latex-templated porous sol-gel silica presented by Guillemot *et al.* [25], since it provides a closed porosity that is not infiltrated by water and can be structured using imprint lithography as described in Sec. 4.1. This sol-gel material is based on TEOS precursors, see Tab. 3.1. However, in order to obtain an imprintable material, MTES precursors must be added as well. A mixture of sols based on TEOS and MTES precursors is therefore used to produce the low-index grating. A latex solution of 77 nm PMMA particles is used for templating a porosity of 25% in order to obtain a low effective refractive index [25]. Figure 6.2 shows the refractive index of such a porous film as function of wavelength. At 532 nm, the index is measured to $n_{\text{eff}} = 1.327 \pm 0.005$.

6.2.1 Charged latex particles for electrophoresis

Silica surfaces become negatively charged when in contact with water [153], so in order to avoid adhesion of latex particles to the charged silica surface, the particles must be negatively charged as well to create electrostatic repulsion. Adhesion of a monolayer of particles will not hinder the device functionality, but it may decrease the efficiency.

For electrophoresis, hydrophilic, negatively charged, carboxylate modified (CML) polystyrene latex particles of 24 ± 3 nm diameter (Molecular Probes, C37231) were used. The particles were supplied in a 4.0% w/v solution in surfactant-free medium of water of pH 4.5. To first order approximation, the refractive index of the latex solution can be calculated as the volume-weighted average of the individual refractive indices of water and polystyrene. Water has refractive index of 1.33, and polystyrene has refractive index of 1.60 and a density of 1.05 g/cm^3 . The index of the 4.0% w/v latex is thus 1.34.

The latex particles are electrosterically stabilized by highly charged surfaces with sulfate ($42.4 \text{ } \mu\text{eq/g}$) and carboxyl ($715 \text{ } \mu\text{eq/g}$) functional groups. The carboxyl groups have a pK of 4.9, so the surface charge is pH-dependent, and it is only at pH 10 that all carboxyl groups are ionized [154, 155]. To obtain the highest surface charge, and hence the largest electrophoretic mobility of the particles, pH of the solution should thus be 10. The negative surface charge density of silica is also increased at large pH, which improves the repulsion of particles from the silica surfaces and prevent adhesion of particles [153].

6.2.2 Device fabrication

Gratings of $2 \text{ } \mu\text{m}$ period, 450 nm line width were made in a fused silica substrate by electron lithography and reactive-ion etching to a structure depth of 280 nm. An anti-stiction layer of FDTS (CAS no. 78560-44-8) was deposited by molecular vapor deposition. Polydimethylsiloxane (PDMS, CAS no. 63148-62-9) stamps were made by casting of the fused silica master.

The nanoporous sol-gel material was made as a mixture of sols based on TEOS and MTES precursors. The TEOS sol was prepared in a closed vial by mixing TEOS and pH 2.5 HCl at a molar mixing ratio TEOS:H₂O of 1:18. Before use, the TEOS sol was aged for 14–18 hours while vigorously stirred. In another vial, MTES was mixed with pH 2.5 HCl at a molar mixing ratio MTES:H₂O of 1:14. The MTES sol was aged for 3 hours while vigorously stirred.

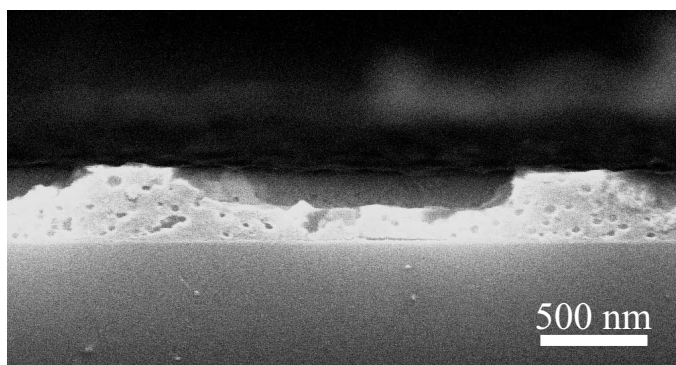


Figure 6.3: Cross-sectional SEM image of nanoporous grating imprinted in sol-gel silica. The grating has $2\ \mu\text{m}$ period, $450\ \text{nm}$ line width, $175\ \text{nm}$ grating depth, and $155\ \text{nm}$ residual layer.

PMMA latex particles with average diameter of $77\ \text{nm}$ were used as sacrificial templates to create porosity as described by Guillemot *et al.* [25]. For a silica film of 25% porosity to be made, PMMA latex must be added to obtain a volume fraction of 25% compared to the total volume of solids. The sol was made by mixing $1.40\ \text{g}$ of aged TEOS sol with $1.75\ \text{g}$ of aged MTES sol, $0.20\ \text{g}$ PMMA latex, and $1.04\ \text{g}$ of pH 2.5 HCl. This solution was stirred for 2 min before spin-coating.

The sol containing the PMMA latex was spin-coated at 2000 rpm for 30 s on a $50\ \text{mm}$ square, $1.1\ \text{mm}$ thick glass substrate with a sputtered layer of indium tin oxide (ITO). HCl etches ITO, but at pH 2.5, corresponding to approximately $3\ \text{mM}$, the etch rate is very low [156], thus allowing the sol to be coated directly on top of the ITO. In order to enable later electrical contact to the electrode, pieces of tape were used to protect parts of the substrate from being covered by sol-gel material.

The PDMS stamp was imprinted in the freshly spin-coated gel film at room temperature at 1 bar pressure. After 1 min imprint time, the temperature was ramped at approximately $10^\circ\text{C}/\text{min}$ to 100°C , where it was kept for 15 min in order to accelerate condensation of the gel and obtain a hard material. After cooling to 50°C , the pressure was released, the PDMS stamp was demolded, and the tape protecting parts of the ITO electrode was removed.

The imprinted device was annealed at 500°C in ambient atmosphere to fully condense the material and calcinate the organics. During this process, the PMMA latex particles disappear, producing voids in the material of the same size as the templating particle [25]. Figure 6.3 shows a cross-sectional SEM image of the imprinted and annealed grating. The film thickness is $330\ \text{nm}$ with a grating depth of $175\ \text{nm}$.

The reconfigurable device was assembled using $75\ \mu\text{m}$ thick self-adhesive PVC tape (SWT 20+, Nitto Denko) to separate the two substrates. Pieces of tape were applied to the area around the imprinted grating, and a drop of the latex solution was deposited on top of the grating. The backside electrode, which was made by unstructured sol-gel silica on an ITO substrate, was put on top, and the two glass substrates clamped together with mechanical screws. The thickness of the liquid film between the two substrates was hence

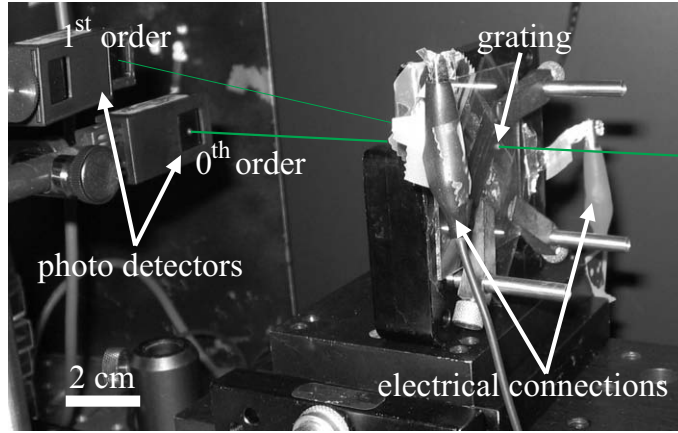


Figure 6.4: Photo of setup. The two glass substrates are clamped together, separated by a $75\ \mu\text{m}$ tape spacer, and placed horizontally. Electrical connections to the ITO electrodes are made using self-adhesive conducting aluminum tape. The beam path of the laser is shown with green lines.

controlled by the thickness of the tape. Electrical connections to the ITO electrodes were made using self-adhesive conducting aluminum tape.

6.3 Results

As shown in Fig. 6.4, the reconfigurable device was mounted vertically in the beam path of a 500 mW 532 nm diode-pumped laser (CrystaLaser). Two photo diodes (PD-300, Ophir) connected to a PC-interface (Pulsar, Ophir) were used to make time resolved measurements of the intensities of the zeroth and first orders of the light diffracted by the grating.

In Fig. 6.5, the measured relative intensities of the zeroth and first diffraction orders are shown as function of time. At $t = 1\ \text{min}$, a potential of 5 V was applied to the electrodes, corresponding to a field strength of $E = 70\ \text{kV/m}$. The negatively charged particles were electrophoretically moved to the positive electrode behind the grating and collected on the structured surface. After a few minutes, the intensity of the first order increased, as a sign of increased grating efficiency due to higher refractive index at the structured surface. At $t = 9\ \text{min}$, the intensity had increased by a factor of 167, corresponding to 22 dB, compared to when no potential was applied.

At $t = 10\ \text{min}$, the potential was reversed, and the charged particles moved away from the structured surface. The refractive index at the structured surface decreased, causing the intensity of the first diffraction order to decrease as well.

In Tab. 6.1, different technologies for reconfigurable gratings are compared to the results of this work. It is seen that the intensity modulation of the first diffraction order demonstrated in this work is a lot higher than what has previously been shown. The expected refractive index modulation is the same as what can be obtained using liquid crystals. The draw back of this device, however, is the very long switching time, but as

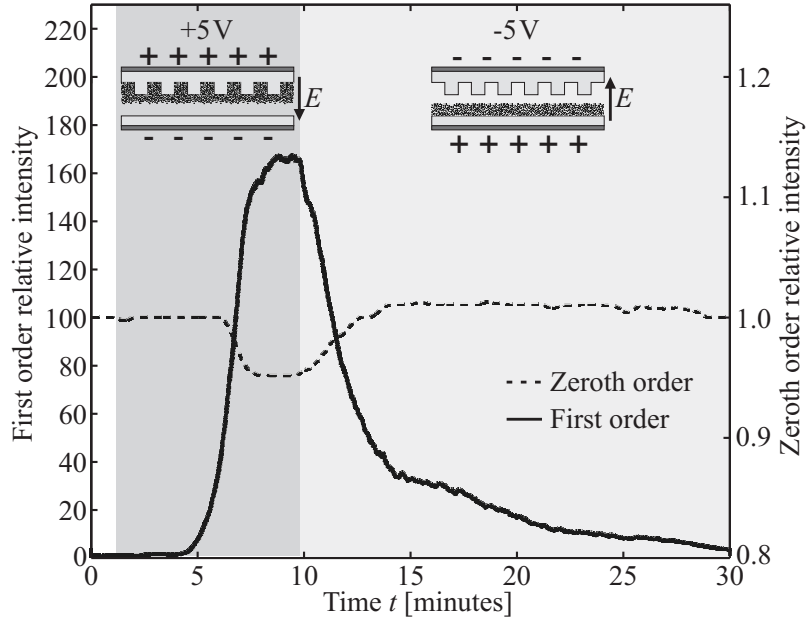


Figure 6.5: Intensities of the zeroth (right axis) and first (left axis) diffraction orders, relative to the intensities at zero electrode potential, as function of time t . Inserts show sketches of the reconfigurable device at forward bias ($1 \text{ min} < t < 10 \text{ min}$), when a positive potential of 5 V was applied to the electrode behind the imprinted grating, and reverse bias ($t > 10 \text{ min}$), when a negative potential of 5 V was applied. At zero electrode potential ($t < 1 \text{ min}$), 1.85 mW was measured for the zeroth order and 297 nW for the first order. When the forward bias was applied, the intensity of the first order increased by a factor 167 to 49.7 μW . As the bias was reversed, the first order intensity decreased again.

discussed in the following section, it may be improved.

6.4 Discussion

6.4.1 pH of latex solution

The result in Fig. 6.5 was obtained using the pure latex solution with pH 4.5. As mentioned above, this was not the optimal condition for having high surface charge of the latex particles and large electrostatic repulsion from the silica surface. However, adjusting the pH by adding a basic solution increases the ionic strength of the latex solution, and hence also the conductivity, which is not convenient for electrophoresis. Initially, pH was adjusted to 8.5 using tris base (CAS no. 77-86-1), but dissolution of the ITO electrodes was observed when the 5 V potential was applied. Besides proving that the conductivity was too high, it also indicated that the electrodes were not well enough isolated using the porous sol-gel silica. This may either be caused by open porosity or imperfections of the material, such as dust particles creating a hole during annealing. The problem may be circumvented by depositing a protective silica film on the ITO before spin-coating of

Evaluation parameter	Electrophoresis of nanoparticles (this work)	Pressure-driven fluid exchange [11]	Electrostatic actuation of liquid crystals [13]
Demonstrated refractive index modulation	0.20 RIU	0.036 RIU	0.20 RIU
Max demonstrated intensity modulation of diffraction orders	22 dB	20 dB	17 dB
Demonstrated switching speed	10 min	50 ms	8–15 ms
Voltage used	5 V	n/a	3–15 V

Table 6.1: Comparison of reconfigurable gratings.

sol-gel. Another option is to improve the sol-gel material to make sure that the porosity is indeed closed.

A long response time is seen in Fig. 6.5 when the potential was applied to the device; it took 4 min before the first order intensity started increasing significantly. The reason for this is that the potential had been reversed before the experiment started. The particles were thus not equally dispersed in the liquid and had to travel through most of the $75\ \mu\text{m}$ water film to reach the grating surface. In order to improve the response time, the charge density can be improved by adjusting pH from 4.5 to 10, as mentioned above. Doing so, a factor of eight increase in the charge density may be possible [155]. Reducing the thickness of the liquid film or increasing the potential will also help to improve the mobility.

Initially, when the potential was reversed in Fig. 6.5, at $t = 10$ min, the first order intensity decreased as fast as it rose. However, at $t = 13$ min, when the intensity had decreased to a quarter of the maximum level, the decrease slowed down. This may be due to particles adhering to the silica surface. Running the device at optimal pH, as discussed above, may improve on this due to the increased electrostatic repulsion between latex particles and silica surfaces and the increased electrophoretic mobility.

Silica is dissolved by water, as seen in Fig. 3.2, with a dissolution rate [60, 157, 158] and a solubility [159] that strongly depend on pH and temperature. For the reconfigurable device to have a long life time, it would therefore be advantageous to use acidic or neutral pH of the latex solution. Under these conditions, polystyrene latex particles with sulfate surface groups, which are negatively charged with a surface charge density that is independent of pH [153, 160], would be a good choice.

6.4.2 Closed porosity

In order to index-match the porous sol-gel silica to the surrounding water, it is important that the porosity of the material is closed, meaning that the pores are isolated voids without connection. Otherwise, in the case of an open network of pores connected to the surface, water replenishes the pores by capillary filling or condensation due to the hydrophilic silica surfaces of the pores. The exchange of air in the pores with water increases the effective refractive index of the porous material to a value higher than that

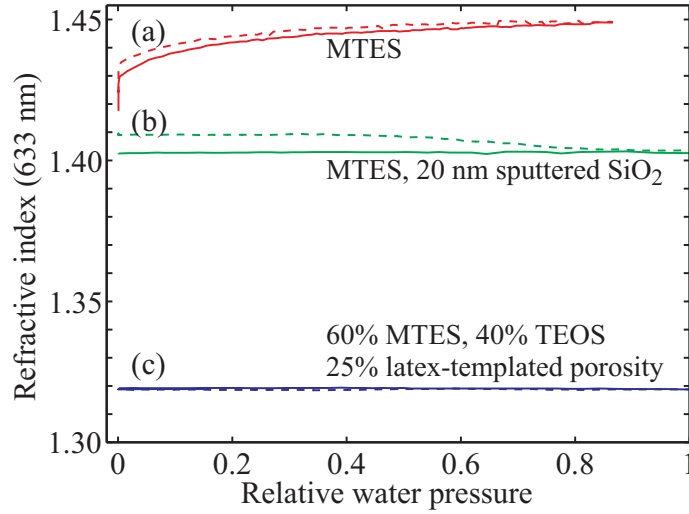


Figure 6.6: Refractive indices of different silica surfaces measured as function of relative humidity. Full lines show adsorption, dashed lines show desorption. (a) Sol-gel silica based on MTES precursors alone. (b) The same material, but with conformal low-vacuum sputter deposition of 20 nm silicon dioxide to close the surface. (c) Sol-gel silica based on 60% MTES and 40% TEOS precursors. A refractive index that is independent of the humidity is sign of a closed porosity [81].

of water.

As described in Paper 1, see App. B, the MTES sol-gel silica annealed at 600°C has an inherent open nanoporosity of 5.9%, which causes the refractive index to depend on relative humidity due to capillary condensation [81]. This is seen in Fig. 6.6, which shows ellipsometric measurements of the refractive indices of different silica surfaces as function of relative humidity. The constant refractive indices in the figure show that a closed porosity is obtained by mixing MTES and TEOS precursors and that closing of the surface is obtained by conformal low-vacuum sputter deposition of 20 nm silicon dioxide.

The imprinted grating that was used for the experiment in Fig. 6.5 was characterized using refractive index-matched liquids (Cargille Labs). Using the setup shown in Fig. 6.4, the zeroth and first diffraction orders were measured at three wavelengths with liquids of different refractive index deposited on the grating under a glass cover slip. Thorough cleaning with methanol and drying with compressed nitrogen was performed before deposits of the different liquids. The result is shown in Fig. 6.7. A minimum is seen for all wavelengths at $n = 1.4$, where the intensity of the first order has decreased by more than two orders of magnitude compared to the intensity at $n = 1.0$. This indicates that the effective refractive index of the grating material is 1.4. However, the ellipsometric measurement of an unstructured surface of the same material, as seen in Fig. 6.2, showed an index of 1.327 ± 0.005 at 532 nm wavelength.

The most likely explanation for this discrepancy is that the porosity of the grating is *not* closed, despite the experiment in Fig. 6.6 showing that mixed MTES and TEOS precursors should result in closed pores. SEM images like the one in Fig. 6.3 show no sign of aggregation of the PMMA latex particles, however, there may still be the inherent

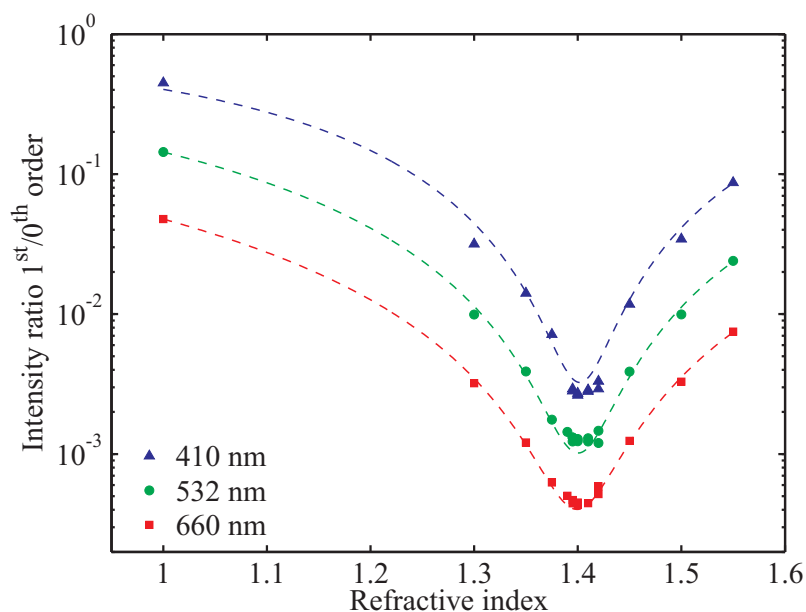


Figure 6.7: Characterization of imprinted porous grating, see Fig. 6.3, using different refractive index-matched liquids. The ratio between the intensities of the first and zeroth diffraction orders are shown for three different wavelengths as function of the refractive index of the liquid surrounding the grating. Cauchy-distributions have been fitted to the data to guide the eye. The experiment was performed using the setup shown in Fig. 6.4.

nanoporosity that connects the voids templated by the PMMA latex. Hence, when a liquid is deposited on the grating, it enters the pores and increases the effective index of the grating. The intensity minimum in Fig. 6.7 at $n = 1.4$ shows that at least some of the pores are dry, since, otherwise, the minimum would have occurred at the index of silica at $n = 1.46$. The reason for the open porosity of the imprinted grating may be that solvent evaporation and condensation are different when the material is in contact with a stamp, compared to a material film which is not imprinted, and hence the collapse of pores may be different as well.

Beside the question about whether the porosity is open or closed, also the distribution of PMMA latex particles in the material is important for the uniformity of the effective refractive index throughout the imprinted structure. During imprint, it is important the PMMA particles flow together with gel when the cavities of the stamp are filled. If the gel flows faster than the particles, the concentration of particles will be smaller in the stamp cavities, which leads to less porosity and hence higher effective index in those regions of the material. A non-uniform pore distribution may thus be another explanation for the apparent higher refractive index of the grating. However, the particle distribution after imprint has not been studied in this work.

6.5 Chapter summary

In this chapter, reconfigurability of a diffraction grating was demonstrated using electrophoresis of charged sub-wavelength nanoparticles. A low-index silica grating was fabricated by imprint of a sol-gel material with PMMA latex particles to template a porosity. The low index of the grating was used to enable index-matching of the silica structures to a solution of latex particles. By electrophoretic concentration of charged latex nanoparticles on the structured surface, it was shown that the intensity of the first diffraction order of the grating could be increased by a factor 167. This is higher than what has previously been demonstrated by other methods of making reconfigurable gratings. Long switching times of the device were experienced, but it is believed that improvement of the electrode insulation and adjustment of pH of the latex solution will ameliorate the performance of the device.

Chapter 7

Controlled deposition of sol-gel sensor material using hemiwicking

7.1 Sol-gel-based optical sensors

Sol-gel material, as introduced in Chap. 3, can be used as a solid matrix for immobilization of, e.g., particles or molecules, which are easily dispersed in the liquid sol and during cross-linking of the gel become immobilized inside the material [22, 63, 64, 161]. For example, optical sensor materials can be fabricated by immobilization of analyte-sensitive dye molecules in a silica xerogel, which, due to its porosity, is permeable to the analyte while steric confinement of the dye molecules prevents leaching. This kind of sensor material is used in reagent-based optical sensing systems, where a change in the optical response of the analyte-sensitive dye molecule is used to monitor the analyte concentration. In liquid form, sol-gel-based materials can be coated on a wide range of substrates, which makes this kind of optical sensor materials very versatile [63].

In biotech applications such as, e.g., cell culturing [163], constant monitoring of pH and dissolved oxygen is of great importance. Sol-gel-based sensor materials for measuring these analytes [164, 165] enable fabrication of cheap optical sensors, which can be integrated in disposable lab ware, such as cultivation bags, shake flasks, and petri dishes. Using

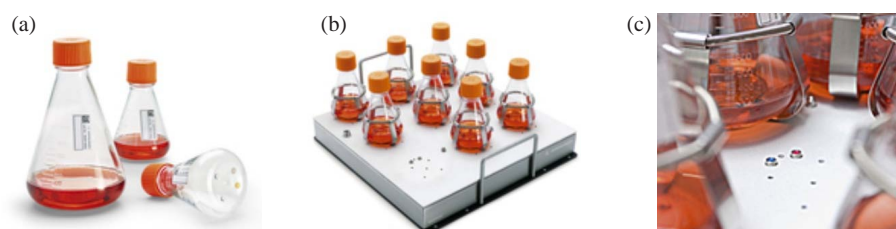


Figure 7.1: Sartorius SENSOLUX[®] sensor system. (a) Single-use shake flasks with sensor spots in the bottom. The shaker platform (b) has built-in optics (c) for reading of the sensor spots. Images adapted from [162].

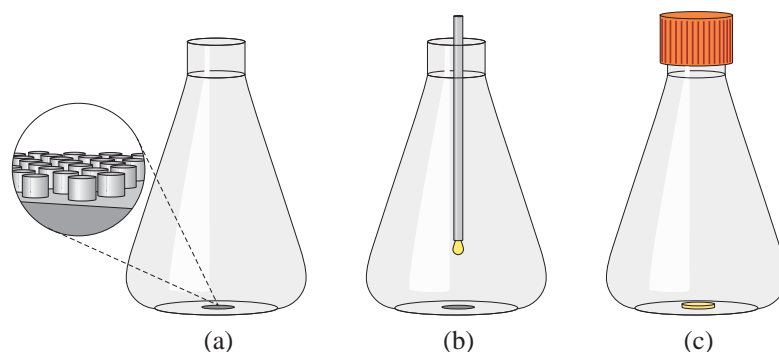


Figure 7.2: Sketch of the deposition of sol-gel sensor material on microstructures inside a container. On an array of microstructures in the bottom of a shake flask (a), a small drop of liquid sensor material is deposited (b). The material is spread, guided by the structures, to produce a uniform film on the surface, and after evaporation of solvents and thermal cross-linking at 110°C , fabrication of the sensor spot is finished (c).

integrated sensors, invasive probes are avoided and sources of contamination are reduced, since the sensors are disposable and optically read from outside of the container. An example of such a sensor system is shown in Fig. 7.1.

Coatings of sol-gel material can be produced using dip-, spray-, or spin-coating [68–70], and homogeneous thin films of sol-gel sensor material, which are required for getting fast and uniform response times of the optical sensors, have been demonstrated on dip-coated substrates [165]. However, for deposition of sensor material on the inside of containers, or when several different sensor materials are to be deposited in separate areas on the same surface, these coating methods are not feasible. In present commercial applications of this sensor technology [162, 166], patches with sensor material are fabricated and manually glued to the inside of containers.

In this chapter, a novel method for fabrication of such sensor spots is presented. The method enables deposition of liquid sensor material in a homogeneous layer on a well-defined region of a surface. By decorating the surface with periodic micropillars and using the principle of *hemiwicking* [167], a drop of liquid material that is deposited on the microstructured surface will spread, guided by the structures, to homogeneously fill the volume between the structures. Spreading of the liquid is governed by the geometry of the microstructures and surface energy, and the thickness of the deposited film is determined by the height of the micropillars and is thus independent of the volume of the deposited drop. This enables easy and reproducible deposits of spots of sol-gel sensor material of precise thickness to be made on plastic surfaces inside containers, and it simplifies the fabrication of optical sensors in disposable lab ware. A sketch of the deposition process is shown in Fig. 7.2.

Microstructuring of the inside of blow-molded plastic containers, such as shake flasks, may be performed using Step & Stamp imprint lithography [47], and for plastic components produced by injection molding, microstructures can be integrated directly in the mold [94]. Both of these fabrication methods are suited for large-scale industrial production.

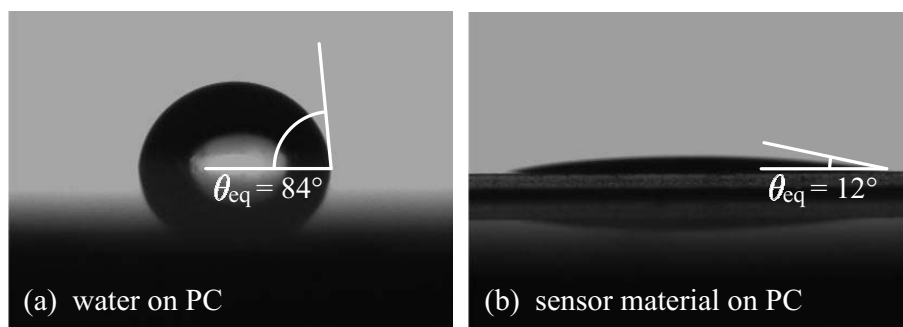


Figure 7.3: Optical measurements of equilibrium contact angles of drops of (a) MilliQ water and (b) ETEOS-based sol-gel oxygen sensor material [165] on polycarbonate foil. Measurements performed using Krüss DSA 10 drop shape analyzer.

In the following sections, it is explained how the spreading of a liquid on a surface is controlled by surface energy and how it is influenced by periodic microstructures on the surface.

7.2 Wetting of a surfaces

7.2.1 Surface energy

Surface energy can be described from a molecular point of view considering an interface between liquid and gas. In bulk liquid, a molecule gains binding energy by forming chemical bonds with the neighboring molecules. However, at the interface to the gas, at the surface, a molecule cannot form as many bonds, since the molecule density is very low in the gas. This lack of chemical bonds results in a higher energy of molecules at the interface. It thus costs energy to increase the area of the surface. The surface energy density, or surface tension, γ of an interface between different phases is defined as the Gibbs free energy \mathcal{G} per area \mathcal{A} for constant pressure and temperature [33]

$$\gamma \equiv \left(\frac{\partial \mathcal{G}}{\partial \mathcal{A}} \right)_{p,T}. \quad (7.1)$$

7.2.2 Contact angle θ_{eq}

When a drop of liquid is deposited on a solid material, solid-gas, solid-liquid, and liquid-gas interfaces are produced between the three different phases. These different kinds of interfaces have associated different surface energy densities γ_{sg} , γ_{sl} , and γ_{lg} . In equilibrium, the surface areas of the interfaces will be arranged so that the lowest possible total energy of the system is reached. This affects the equilibrium contact angle θ_{eq} , which is the angle that appears between the solid-liquid and the liquid-gas interfaces at the contact line where the three phases meet. Figure 7.3 shows contact angles for water and sol-gel material on a polycarbonate substrate.

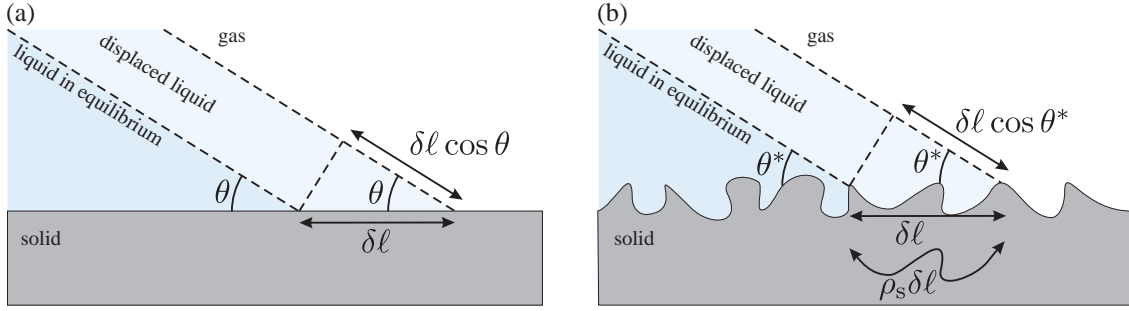


Figure 7.4: Cross-sectional views of the contact line where three different phases meet in the cases of (a) a flat solid surface and (b) a rough solid surface where the surface area has been increased by a factor of ρ_s relative to the horizontal projection of the surface. Figures adapted from [33] and [167].

Figure 7.4a shows a sketch of the contact line for liquid on a flat solid surface. For an infinitesimal displacement of the contact line δl from equilibrium, it can be seen from Fig. 7.4a that the changes of the interface areas are proportional to $-\delta l$, δl , and $\delta l \cos \theta$ for the solid-gas, solid-liquid, and liquid-gas interfaces, respectively. In order for the system to stay in equilibrium, it is required that the free energy is unchanged, and hence that $\partial \mathcal{G} = -\gamma_{sg} \delta l + \gamma_{sl} \delta l + \gamma_{lg} \delta l \cos \theta = 0$. Rearranging gives Young's equation for the equilibrium contact angle [33]

$$\cos \theta_{\text{eq}} = \frac{\gamma_{sg} - \gamma_{sl}}{\gamma_{lg}}. \quad (7.2)$$

For systems where $\gamma_{sg} > \gamma_{sl}$, it is favorable to have a large solid-liquid interface and a smaller solid-gas interface, and hence $0^\circ < \theta_{\text{eq}} < 90^\circ$. The liquid will wet a large area of the solid surface, which is then said to be wetting, or hydrophilic in the case of water. For systems where $\gamma_{sg} < \gamma_{sl}$, it is favorable to have a small solid-liquid interface and a larger solid-gas interface, and hence $90^\circ < \theta_{\text{eq}} < 180^\circ$. The liquid will wet a small area of the solid surface which is then said to be antiwetting, or hydrophobic in the case of water.

7.2.3 Wetting of rough surfaces

Surface topography can change the wettability of a surface. This is illustrated in Fig. 7.4b where the contact line for liquid on a rough solid surface is sketched. Compared to the flat surface, the area of the rough surface has been increased by a factor of ρ_s . For an infinitesimal displacement of the contact line δl , the wetted surface area is thus increased by $\rho_s \delta l$. Following the same arguments as in the derivation of Young's equation, the Wenzel relation is found, [167]

$$\cos \theta^* = \rho_s \cos \theta_{\text{eq}}, \quad (7.3)$$

where θ^* is the apparent contact angle that is measured macroscopically as in Fig. 7.3. Equation 7.3 predicts that roughness enhances the hydrophilicity of a hydrophilic surface, and similarly, the hydrophobicity of a hydrophobic surface. However, this relation is only

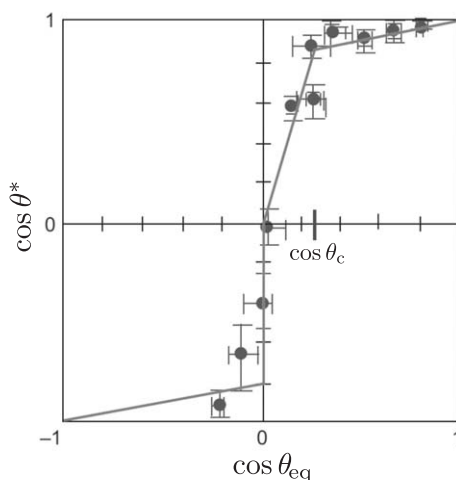


Figure 7.5: Plot of the apparent contact angle θ^* of a liquid on a structured surface as function of the contact angle θ_{eq} of the liquid on a flat surface of the same material. Different liquids are used to vary θ_{eq} . Figure adapted from [167].

valid for $\cos \theta_{\text{eq}}$ smaller than a critical angle $\cos \theta_c$ [167], which is defined in the following section.

Figure 7.5 shows the results of an experiment by Shibuichi *et al.* [168] where the apparent contact angle θ^* of a liquid on a structured surface is shown as function of the contact angle θ_{eq} of the liquid on a flat surface of the same material. A somewhat linear relation, as predicted by Eq. 7.3, is seen for $\cos \theta_{\text{eq}} < \cos \theta_c$. Above $\cos \theta_c$, the scaling is different due to wetting of the microscopic surface texture, as is described below. Figure 7.5 demonstrates that the hydrophilicity or hydrophobicity of surfaces can be largely enhanced by microstructuring the surfaces [167, 169]. Such superhydrophilic ($\theta^* < 5^\circ$) or superhydrophobic ($\theta^* > 150^\circ$) surfaces find use in applications where, e.g., self-cleaning [18–20] or antifogging [170] surface properties are wanted.

7.3 Hemiwicking

On a wetting solid surface, liquids can be imbibed and spread by a surface texture in a process that is similar to capillary wicking in textile or paper [167]. The surface texture may be either a natural roughness or an artificial, microfabricated pattern. In wicking, a solid-gas interface is exchanged by a solid-liquid interface as the solid material imbibes the liquid. However, when solid surface structures imbibe a liquid, it is not wicking that occurs, since a liquid-gas interface is produced as the liquid film progresses, and the phenomenon is hence called hemiwicking [171].

7.3.1 Critical angle θ_c

Figure 7.6 sketches a liquid film propagating inside a forest of micropillars of height h , radius r , and period $d = l + 2r$. For a hexagonal lattice of pillars, the pillar density

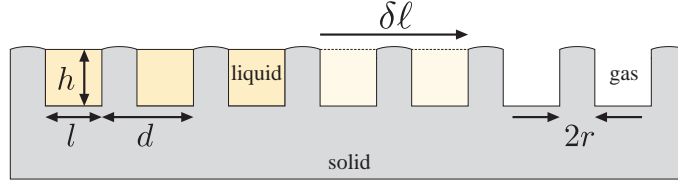


Figure 7.6: Cross-sectional sketch of a liquid film propagating inside a forest of micropillars of height h , radius r , and period $d = l + 2r$. When the film propagates the distance $\delta\ell$, the area of the solid-liquid interface is increased by $(\rho_s - \phi_s)\delta\ell$ and the area of the liquid-gas interface is increased by $(1 - \phi_s)\delta\ell$, where ρ_s is the roughness and ϕ_s is the pillar density.

$\phi_s = 4\pi r^2/(\sqrt{3}d^2)$ and the surface roughness is $\rho_s = 1 + 4\pi r h/(\sqrt{3}d^2)$. When the film propagates a distance $\delta\ell > d$, the increase of the solid-liquid interface is proportional to $(\rho_s - \phi_s)\delta\ell$, whereas the increase of the liquid-gas interface is proportional to $(1 - \phi_s)\delta\ell$. For this progression to be favorable, free energy must be gained, and hence

$$\partial\mathcal{G} = (\gamma_{sl} - \gamma_{sg})(\rho_s - \phi_s)\delta\ell + \gamma_{lg}(1 - \phi_s)\delta\ell < 0. \quad (7.4)$$

By rearranging and inserting Eq. 7.2, it is found [171] that the progression is only favorable for

$$\cos\theta_{\text{eq}} > \frac{1 - \phi_s}{\rho_s - \phi_s} \equiv \cos\theta_c, \quad (7.5)$$

which defines the critical angle θ_c below which hemiwicking may occur.

7.3.2 Spreading of liquid by hemiwicking

When a drop of liquid is deposited on a microstructured wetting surface, some of the liquid will penetrate into the surface texture to wet it, while the remaining drop lies as a spherical cap on top of the microstructures. The front of the penetrating liquid will continue to propagate within the surface texture, minimizing surface energy, until it reaches the edges of the drop. However, if θ_{eq} is smaller than θ_c , hemiwicking is favorable, and the liquid front will continue to spread within the surface texture beyond the extent of the drop. A liquid film is thus formed over the surface, between the microstructures, while the drop is drained. This is sketched in Fig. 7.7a in the case of a surface with a periodic array of micropillars.

Surface structures can pin a contact line [172], and for disconnected structures like the array of pillars, the liquid front must be activated to continue the progression. For wetting liquids, this is made possible via the meniscus forming around each pillar. In order for the contact line to continue the progression, the meniscus must be able to extend from one row of pillars to the next [173]. Assuming zero mean curvature of the meniscus, the condition for sufficient extension is $h/l > \tan\theta_{\text{eq}}$ on an array of micropillars of height h , radius r , and period $d = l + 2r$, as sketched in Fig. 7.7b. Before attaining the equilibrium contact angle, the advancing contact line will thus reach the next row of pillars, which will be wetted, and the liquid front will continue to propagate on the other side. This will proceed until the drop, which was initially on top of the pillars, has been drained

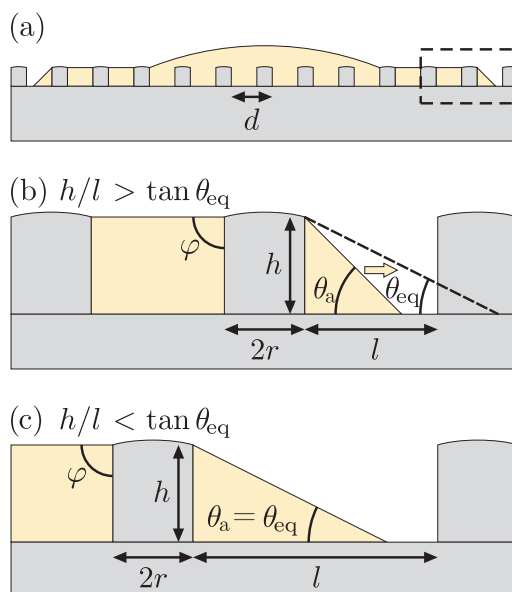


Figure 7.7: (a) Cross-sectional sketch of a drop of liquid deposited on a two-dimensional array of micropillars of height h , radius r , and period $d = l + 2r$. Driven by surface energy, a liquid film self-propagates within the microtexture, spreading the liquid and draining the drop, which lies as a spherical cap on top of the pillars. (b) Enlarged view of the dashed box in (a) showing the liquid front in the case of $h/l > \tan \theta_{eq}$. The contact angle of the advancing liquid front θ_a is larger than the equilibrium contact angle θ_{eq} , and the liquid front will reach the next row of pillars before attaining θ_{eq} . The next row of pillars will thus be wetted, and the propagation continues on the other side. In (c), the same situation is shown for a different geometry with $h/l < \tan \theta_{eq}$. In this case, the liquid front is pinned when $\theta_a = \theta_{eq}$ and the propagation is stopped. At the top of the pillars, the contact line is pinned by the corner, and surface energy forces $\varphi = 90^\circ$, producing a flat air-liquid interface. Figure from Paper 3.

completely and all the liquid has been imbibed by the microstructure, provided that the inter-pillar volume is large enough to contain the drop volume.

The contact line at the top of the pillars is pinned by the corner, so that the contact angle φ is not limited to θ_{eq} but can take a wide range of values [167, 174]. For narrow structures, surface energy forces $\varphi = 90^\circ$, thus producing a flat liquid-gas interface [175]. The pillar height h thus exclusively determines the thickness of the deposited liquid layer. The volume of the deposited drop controls the size of the wetted area, but it does not affect the deposited material thickness. Hemiwicking can thus be used for producing liquid films of precise thickness [167].

In the case of a geometry with $h/l < \tan \theta_{eq}$, as sketched in Fig. 7.7c, the liquid front gets pinned when the advancing contact angle θ_a equals θ_{eq} , and propagation stops before the next row of pillars is reached [176]. The same situation is found when a spreading liquid reaches the edge of the structured area. However, propagation may continue in other directions on the structured surface, and filling of the surface structure is hence not sensitive to alignment as long as the liquid is deposited inside the patterned area.

To create a uniform film of sensor material by hemiwicking, it is required that solvent evaporation of the deposited sol-gel material happens much slower than the spreading of the material. Otherwise, evaporation during spreading will result in inhomogeneous sensor spots. The propagation speed of the spreading liquid film increases with h/l [176], and hence the geometry of the surface structures can be optimized to minimize the spreading time.

7.4 Results from Paper 3

In order to find the optimal surface structures for uniform spreading of sol-gel sensor material, depositions of the material were made on a series of 7 mm diameter arrays of pillars of different dimensions and periods, which were fabricated by thermal imprint lithography on polycarbonate foil. Polycarbonate was chosen since it is a common material for laboratory bottles. As shown in Fig. 7.3b, the contact angle of the ETEOS-based sol-gel oxygen sensor material described by Higgins *et al.* [165] was measured to $\theta_{\text{eq}} = 12^\circ \pm 3^\circ$ on a flat polycarbonate surface. Pillar radii and periods were chosen to make ratios of h/l ranging from 0.06 to 5. For all geometries $\theta_{\text{eq}} < \theta_c$.

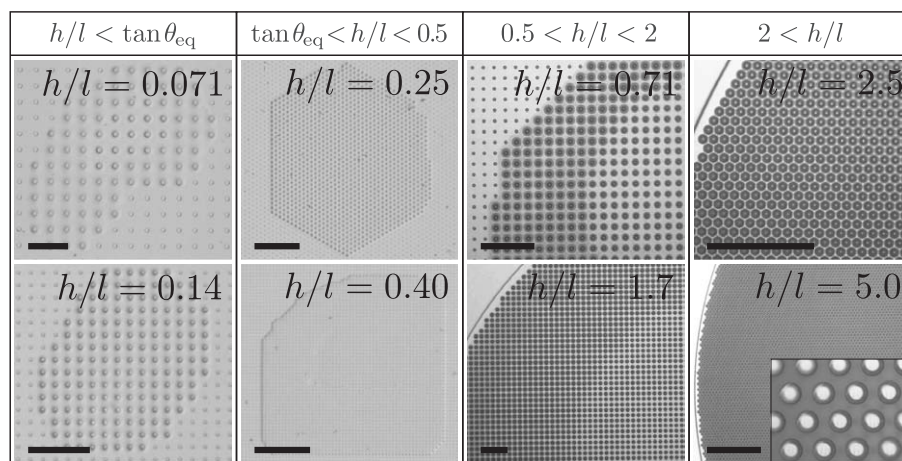


Figure 7.8: Top-view of sol-gel sensor material deposited on polycarbonate foil with regions of different pillar geometries. The deposition results are grouped into four regimes, depending on the ratio of h/l in relation to $\tan\theta_{\text{eq}} \approx 0.2$. Homogeneous spreading of the sensor material is only obtained for surface structures with $h/l > 2$, as shown in the bottom row. Scale bars show 500 μm . Figure from Paper 3.

Figure 7.8 shows examples of depositions of the sensor material on microstructures of different geometry. Like Courbin *et al.* [176] and Extrand *et al.* [175], we found that the ability of a given geometry to homogeneously spread the sensor material mainly depends on the ratio of h/l , and for structures of equal h/l , it is relatively independent of pillar height and lattice pattern, i.e., rectangular or hexagonal. As shown in Fig. 7.8, the deposition results can therefore be grouped into four regimes of h/l in relation to the equilibrium contact angle $\tan\theta_{\text{eq}} \approx 0.2$:

- For $h/l < \tan \theta_{\text{eq}}$, the liquid front gets pinned as sketched in Fig. 7.7c, and propagation beyond the drop is not possible. Evaporation causes uneven material distribution with ring deposits as described in Ref. [177].
- For $\tan \theta_{\text{eq}} < h/l < 0.5$, metastable pinning by the pillars happens easily, and propagation is slow and very sensitive to the lattice pattern. This favors formation of polygonal shapes of the deposited material, as described in Ref. [176]. Unless the deposited volume is small, spreading is incomplete and material is left on top of the surface structures.
- For $0.5 < h/l < 2$, the deposited material spreads independently of the lattice pattern to form a round deposition area. This is in correspondence with Ref. [176] for increased h/l . However, the material distribution is uneven, with the deposit being homogeneous in the center but denser at the perimeter. The inhomogeneity diminishes as h/l is increased.
- For $2 < h/l$, very homogeneous layers are produced.

Figure 7.8 shows that the homogeneity of the deposited film increases as the ratio of h/l is increased. We explain this tendency by the increasing propagation speed for increasing h/l [176]: For small h/l , the spreading time is large, and much of the solvent evaporates while the material is spreading. The solid content of the liquid material thus increases as the film progresses, resulting in an inhomogeneous deposition. Evaporation-induced redistribution of material, as described by Deegan *et al.* [177], may also play a role. At high h/l , the spreading time is small, and less solvent evaporates during spreading. Most of the solvent thus evaporates from the material after a uniform film has been made. Uniform evaporation rates over the film result in homogeneous material deposition, considering length scales larger than period d of the pillars. Between the pillars, on length scales smaller than d , non-uniform evaporation may cause redistribution of material [177].

Evaporation time depends on the volatility of the solvents and the thickness of the liquid film, and spreading time depends on the distance, the contact angle, and the liquid viscosity. Therefore, the mentioned regimes of h/l are only valid for the specific surface structures and materials. Based on the uniformity of the depositions of sensor material on different surface structures and the sensing performance of the fabricated sensor spots, the best results were obtained with a hexagonal lattice with $h = 23 \mu\text{m}$, $r = 9.5 \mu\text{m}$, $d = 30 \mu\text{m}$, and $h/l = 2.1$.

Figure 7.9 shows cross-sectional SEM images of condensed sol-gel sensor material on the $23 \mu\text{m}$ high, $19 \mu\text{m}$ wide polycarbonate structures. The thickness of the sensor material is measured to $5 \mu\text{m}$ at the center between the pillars. It is seen that the vertical sidewalls have been coated by a layer of sensor material with a thickness of the order of a few hundred nanometers, and at the bottom between the pillars, the surface is meniscus-shaped. The material thickness is thus inhomogeneous within each unit cell of the pillar array. However, this inhomogeneity is repeated in every unit cell, so when averaging over length-scales larger than the period $d = 30 \mu\text{m}$, the material distribution can be considered homogeneous.

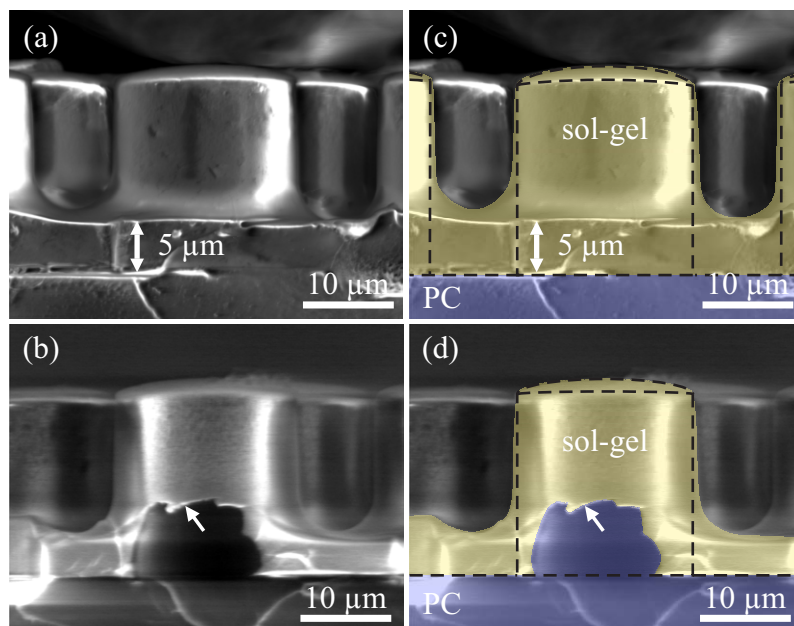


Figure 7.9: (a,b) Cross-sectional SEM images of condensed sol-gel oxygen sensor material deposited on $23\ \mu\text{m}$ high, $19\ \mu\text{m}$ wide pillars imprinted in polycarbonate (PC) foil. (c–d) show same images as (a–b), but with overlaid colors to highlight the PC substrate and pillars (blue) and the sol-gel coating (yellow). Dashed lines show outline of the front-row of pillars. (a,c) After evaporation of solvents, the thickness of the deposited sensor material is $5\ \mu\text{m}$. Between the pillars, menisci are seen. (b,d) The fracture shows that a thin film of sensor material has been deposited on the vertical side walls of the pillars, indicated by the arrow. Due to the ductility of the PC foil, cleavage was difficult and could only be performed during immersion in liquid nitrogen. Figure from Paper 3.

7.4.1 Sensor characterization

Sensor spots for pH and oxygen sensing were fabricated by depositing the two different sensor materials on polycarbonate foil with the optimized $7\ \text{mm}$ diameter pillar-arrays of $h = 23\ \mu\text{m}$, $r = 9.5\ \mu\text{m}$, and $d = 30\ \mu\text{m}$. The performance of the sensors was evaluated as described by Wencel *et al.* [164] and Higgins *et al.* [165].

Five pH sensor spots were characterized by measuring the intensity ratio between fluorescence at $460\ \text{nm}$ and $408\ \text{nm}$ wavelengths as function of pH. By fitting of a sigmoidal function, the $\text{p}K_{\text{a}}$ was estimated to 6.43 ± 0.08 . This value corresponds well to the $\text{p}K_{\text{a}}$ of 6.28 ± 0.02 given in Ref. [164], which was made using five different films produced by dip-coating, and the small uncertainty indicates good spot-to-spot reproducibility.

Equally, on the oxygen sensor spots, the excited-state life time τ was measured on 38 different spots in oxygen-free atmosphere τ_0 and ambient air of 20.9% oxygen. The Stern-Volmer constant $K_{\text{SV}} = ((\tau_0/\tau) - 1)/[\text{O}_2\%]$, where $[\text{O}_2\%]$ is the concentration of O_2 in percentages, was calculated.

In Tab. 7.1 the results of the sensor characterization are tabulated together with the results obtained in Refs. [164] and [165] on dip-coated films. The excited-state life time

	This work	Dip-coating [164, 165]
pK_a	6.43 ± 0.08	6.28 ± 0.02
$\tau_0 [\mu\text{s}]$	6.061 ± 0.024	$4.91 \pm 10\%$
$K_{\text{SV}} [\text{O}_2\%]^{-1}$	0.080 ± 0.002	0.072 ± 0.002

Table 7.1: Comparison of sensor characteristics for pH and oxygen sensors fabricated by hemiwicking (this work) and dip-coating.

in oxygen-free atmosphere τ_0 is seen to be larger than for the dip-coated sensors, which is most likely caused by the ten-fold thicker layer of sensor material deposited on the microstructured surface. The thicker material layer may also explain the slightly larger value of K_{SV} . However, it is worth noticing that the standard deviation of τ_0 is only 0.40% compared to the much larger 10% stated in Ref. [165]. The standard deviations of K_{SV} are of equal magnitude for the two deposition methods.

7.5 Chapter summary

In this chapter, it was shown that microstructures on a surface can be used to guide the spreading of a liquid material to form a thin film with a thickness that is determined by the height of the microstructures. This principle enables liquid films of very precise thickness to be made, and it was used to produce optical sensors by spreading of a liquid sol-gel sensor material on a microstructured polycarbonate surface. For a surface with micropillars, it was found that the ability to uniformly spread a liquid mainly depends on the ratio h/l , and through a series of depositions on different pillar geometries, the optimal structure dimensions were found for spreading of sol-gel sensor material. After evaporation of the solvents, the condensed sensor material was uniformly distributed over the structured surface. The sensing performance of sensor spots fabricated by hemiwicking was characterized and found to be very reproducible and in good correspondence with the performance of sensors fabricated by dip-coating of the same sensor material. An improved method for fabrication of cheap optical sensors, which can be integrated in disposable lab ware, was thus demonstrated.

Chapter 8

Conclusions and outlook

In this thesis, optofluidic applications of sol-gel material were presented along with a study of the dynamics of DNA molecules in a nanofabricated entropic trap device.

A process for fabrication of all-silica lab-on-a-chip devices by nanoimprint of a sol-gel material was presented. Using a multi-level stamp, channels of different depths were produced in a single process step, and costly high-vacuum processes were avoided. This makes the fabrication much simpler and cheaper than top-down processing of fused silica or silicon substrates. Annealing of the imprinted hybrid sol-gel material in oxygen atmosphere produced a purely inorganic silica material, which had very low autofluorescence and could be fusion bonded to a glass lid.

A rigid stamp was required in order to imprint both micro- and nanostructures. To allow imprint with a non-permeable silicon stamp, a novel process was developed, in which the water content was reduced before imprint. Using this imprint process, high-quality, bonded silica nanochannels of 390 nm by 170 nm cross-sectional dimensions were produced, and their applicability to DNA experiments was demonstrated by extension measurements of DNA molecules confined in the fabricated nanochannels.

Sol-gel imprint was found particularly suitable for imprint of high-density nanostructures with low residual layer thickness, which has a high density of free surfaces. For such structures, a high pattern fidelity was obtained. This makes it an ideal method for fabrication of photonic devices, such as gratings or photonic crystals.

For future work on fabrication of nanofluidic devices by imprint of sol-gel silica, it is recommended that a thorough study of the deformation during annealing is carried out. In particular, it should be studied how the deformation depends on different parameters, such as residual layer thickness, imprint conditions, and annealing temperature profile. Such a study will help making a device design that is easily fabricated. Furthermore, it could be investigated how dummy structures or a templated porosity, as described in Chap. 6, can reduce the material shrinkage by increasing the density of free surfaces in the material.

The ability to spin-coat sol-gel materials may enable another easy method for fabrication of nanochannels. By coating of the sol-gel material on top of sacrificial polymer structures, sol-gel silica nanochannels may be obtained by calcination of the sacrificial polymer,

as demonstrated by Li *et al.* [102] using PECVD deposition of silica, see Fig. 4.4g–h.

The dynamics of linear and circular DNA molecules was studied under pressure driven flow in a slit channel with arrays of transverse nanogrooves. In the nanogrooves, the DNA was both stretched and entropically trapped, and as the buffer flow was increased, escape of the DNA into the slit channel, initiated by either an end or a hernia of the molecule, was enabled. It was found that molecule transport through the device occurred through two states of propagation: a slow, stepwise groove-to-groove translation called the 'sidewinder' and a fast, continuous tumbling across the grooves called the 'tumbleweed'. Dynamical transitions between the two states caused DNA molecules to exhibit both size- and topology-dependent velocities that may be utilized for DNA separation, molecule filtering, or sample preparation. In the nanogroove device, the velocity of T4 GT7-DNA (165.6 kbp) was up to 500 times faster than the velocity of the shorter λ -DNA (48.5 kbp). For 9-42 charomid DNA (42.2 kbp), circular molecules propagated up to 8 times faster than linear molecules of the same contour length.

For future work on entropic trapping of DNA, experiments should be made with several different molecule lengths in order to estimate the resolution of the separation device. The very high relative velocity, which was observed between T4 GT7-DNA and λ -DNA, suggests that the device may be used as a tunable filter through which only molecules above a certain length can pass.

The escape of a polymer end or hernia into a cavity, which was considered in this work, is a general issue in polymer physics [178]. It would thus be interesting to study the escape mechanism further, for example, by staining the molecule ends with different fluorophores and recording movies at a higher frame rate.

Reconfigurability of a diffraction grating was demonstrated using electrophoresis of charged sub-wavelength nanoparticles. A low-index silica grating was fabricated on transparent electrodes by imprint of a sol-gel material with PMMA latex particles to template a porosity. The low index of the grating was used to enable index-matching of the silica structures to an aqueous solution of charged PS latex particles. By electrophoretic concentration of the charged latex particles on the structured surface, it was shown that the intensity of the first diffraction order of the grating could be increased by a factor 167. This is higher than what has previously been demonstrated by other methods for making reconfigurable gratings. Long switching times of the device were experienced, but it is believed that improvement of the electrode insulation and adjustment of pH of the latex solution will ameliorate the performance of the device.

For future work on the reconfigurable device, it is essential to find the right process for obtaining a closed porosity of the silica material, and hence obtain a stable refractive index which is independent of the surrounding medium. This may possibly be obtained by adjusting the chemistry of the material or the imprint and annealing conditions. Otherwise, closing of the surface by sputter-deposition of silica may be a possibility.

Low-index materials are highly interesting for optofluidic devices, and sol-gel silica materials with tunable refractive index thus have potential for very high impact. A low-index silica may for example be used as cladding material to obtain light-guiding in liquids [179, 180]. Using a fluidic channel as waveguide, a very large interaction-volume between light and analytes dispersed in the liquid can be obtained, and the sensitivity for optical

sensing of the analytes is thereby increased.

Uniform spreading of liquid sol-gel sensor material by hemiwicking on a microstructured surface was demonstrated, and it was shown that surface microstructures can guide a liquid material to form a thin film with a thickness that is determined by the height of the microstructures. This method enables liquid films of very precise thickness to be made, and it was used to produce optical sensors on a microstructured polycarbonate surface. For a surface with micropillars, it was found that uniform spreading by hemiwicking mainly depends on the ratio h/l , where h is the pillar height and l is the inter-pillar distance. By depositing the sensor material on a series of different pillar geometries, the optimal structure dimensions for spreading of the sensor material were found. The sensing performance of sensor spots fabricated by hemiwicking was characterized and found to be very reproducible and in good correspondence with the performance of sensors fabricated by dip-coating of the same sensor material. An improved method for fabrication of cheap integrated optical sensors was thus demonstrated.

For future work on hemiwicking, modeling of the process would be beneficial in order to improve the understanding of material flow, especially with respect to solvent evaporation. Once a substrate surface has been microstructured, the process of deposition of sensor material is easily integrated in a large-scale industrial process train, and the developed method is therefore likely to be used for mass-production of integrated optical sensors.

Hemiwicking may also work for controlled spreading of liquids on nanostructures [181], e.g., by down-scaling the surface structures used in this work by a factor of hundred. This will enable coating of surfaces by sub-micron liquid films. For example, on photonic crystals, the photonic surface structures could work as liquid guides, and coating of the device with active materials for sensing or optical reconfigurability would thus be possible. The method would also enable uniform spreading of, e.g., biomolecules on the surface of a nanostructured optofluidic sensor.

Appendix A

List of publications

Peer-reviewed journal papers

- **Paper 1:** Morten Bo Mikkelsen, Alban A. Letailleur, Elin Søndergård, Etienne Barthel, Jérémie Teisseire, Rodolphe Marie, and Anders Kristensen, All-silica nanofluidic devices for DNA-analysis fabricated by imprint of sol-gel silica with silicon stamp, *Lab on a Chip* **12**, 262-267 (2012). DOI:10.1039/C1LC20689C
- **Paper 2:** Morten Bo Mikkelsen, Walter Reisner, Henrik Flyvbjerg, and Anders Kristensen, Pressure-driven DNA in nanogroove arrays: Complex dynamics leads to length- and topology-dependent separation, *Nano Letters* **11**, 1598-1602 (2011). DOI:10.1021/nl1044764
- **Paper 3:** Morten Bo Mikkelsen, Rodolphe Marie, Jan H. Hansen, Dorota Wencel, Colette McDonagh, Hans Ole Nielsen, and Anders Kristensen, Controlled deposition of sol-gel sensor material using hemiwicking, *Journal of Micromechanics Microengineering* **21**, 115008 (2011). DOI:10.1088/0960-1317/21/11/115008

Conference proceedings

- Morten Bo Mikkelsen, Rodolphe Marie, Jan H. Hansen, Hans Ole Nielsen, and Anders Kristensen, Deposition of sol-gel sensor spots by nanoimprint lithography and hemi-wicking, *Proceedings of SPIE* 8102, 81020N (2011). DOI:10.1117/12.893139

Patent applications

- Jan H. Hansen, Hans Ole Nielsen, Anders Kristensen, Morten Bo Mikkelsen, and, Rodolphe Marie. Method for depositing sensor material on a substrate. Patent number WO/2011/144652.
- Morten Bo Mikkelsen, Jérémie Teisseire, Alban A. Letailleur, Etienne Barthel, Elin Søndergård, and Anders Kristensen, Reconfigurability of optically functional surface topography. Patent application in preparation.

Appendix B

Paper 1

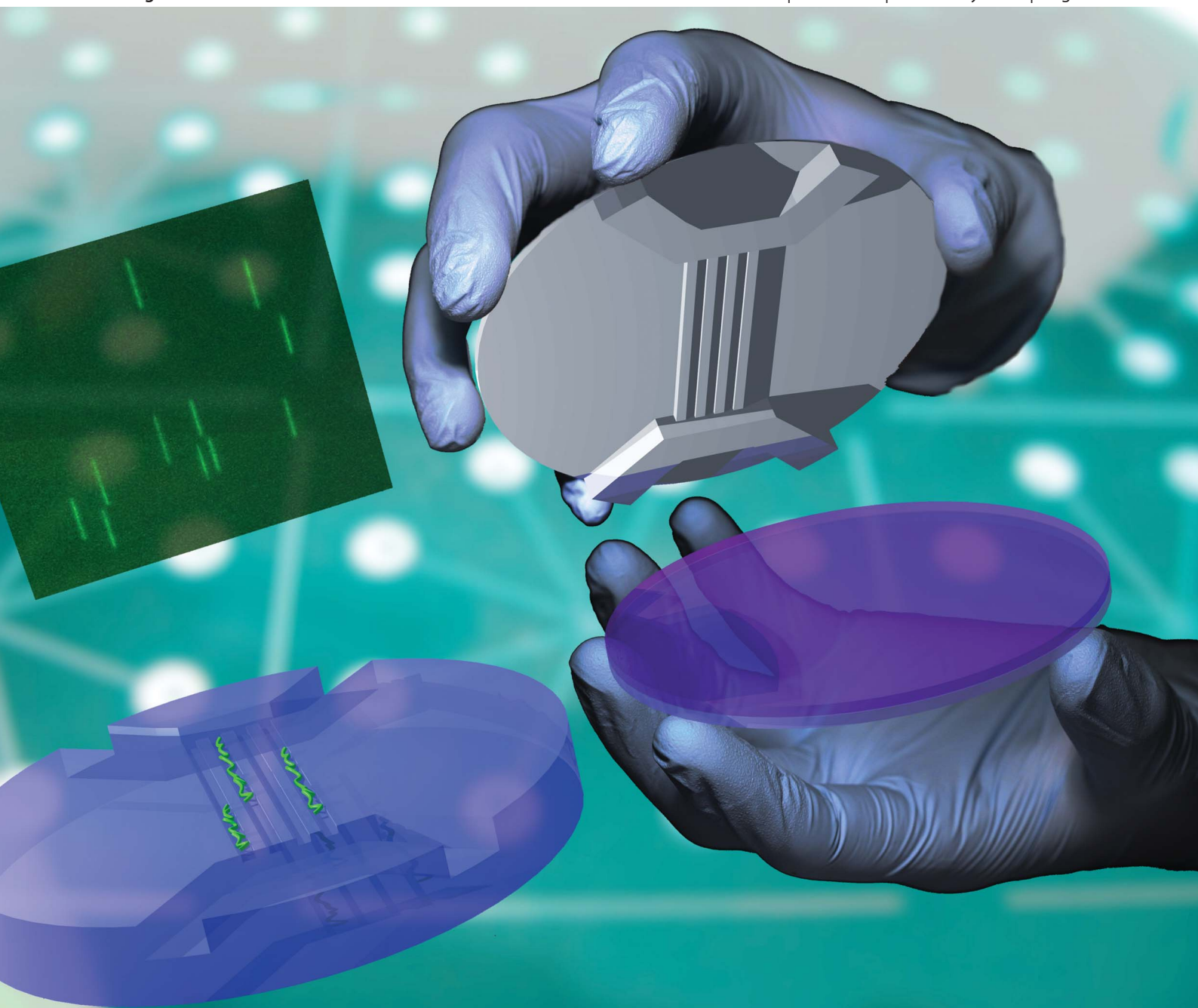
All-silica nanofluidic devices for DNA-analysis fabricated by imprint of sol-gel silica with silicon stamp

Lab on a Chip

Miniaturisation for chemistry, physics, biology, materials science and bioengineering

www.rsc.org/loc

Volume 12 | Number 2 | 21 January 2012 | Pages 229–402



ISSN 1473-0197

RSC Publishing

PAPER

Kristensen *et al.*

All-silica nanofluidic devices for DNA-analysis fabricated by imprint of sol-gel silica with silicon stamp

Cite this: *Lab Chip*, 2012, **12**, 262

www.rsc.org/loc

PAPER

All-silica nanofluidic devices for DNA-analysis fabricated by imprint of sol–gel silica with silicon stamp†

Morten Bo Mikkelsen,^a Alban A. Letailleur,^b Elin Søndergård,^b Etienne Barthel,^b Jérémie Teisseire,^b Rodolphe Marie^a and Anders Kristensen^{*a}

Received 26th July 2011, Accepted 11th October 2011

DOI: 10.1039/c1lc20689c

We present a simple and cheap method for fabrication of silica nanofluidic devices for single-molecule studies. By imprinting sol–gel materials with a multi-level stamp comprising micro- and nanofeatures, channels of different depth are produced in a single process step. Calcination of the imprinted hybrid sol–gel material produces purely inorganic silica, which has very low autofluorescence and can be fusion bonded to a glass lid. Compared to top-down processing of fused silica or silicon substrates, imprint of sol–gel silica enables fabrication of high-quality nanofluidic devices without expensive high-vacuum lithography and etching techniques. The applicability of the fabricated device for single-molecule studies is demonstrated by measuring the extension of DNA molecules of different lengths confined in the nanochannels.

1 Introduction

Confinement of DNA molecules in nanoengineered fluidic devices provides a powerful platform for single-molecule studies. When a DNA molecule is forced into a fluidic nanochannel with dimensions below its radius of gyration, the static conformation of the molecule will be extended perpendicular to the confinement axis.^{1,2} This extension of the molecule enable extraction of information, which is not accessible in its coiled-up conformation in bulk solution, such as physical mapping of fluorescently stained single DNA molecules.^{3–5} Nanotopography in fluidic channels can also create entropic traps that lead to separation of DNA molecules of different length or topology.^{6–8}

Such nanofluidic lab-on-a-chip devices for DNA-analysis have conventionally been fabricated by top-down planar processing of fused silica^{1–6} or silicon^{7,8} substrates due to high quality of processing and low autofluorescence of the materials.⁹ Anisotropic etching of fused silica or silicon provides very good dimensional control, but most of the required lithography and etching techniques are expensive high-vacuum processes, and many process steps are needed to produce nanofluidic channels of different depths in the same device.

Polymer devices for DNA-analysis have been made by imprint lithography¹⁰ and injection molding,¹¹ and elastomeric polydimethylsiloxane (PDMS) devices have been made by casting.¹² These fabrication processes have the advantage of enabling channels of different depths to be produced in a single process step, requiring only subsequent bonding of a lid to complete the device. Easy fabrication and low-cost materials make such nanofluidic devices very cheap to produce, but swelling and deformation of the soft materials during bonding reduce the control of channel dimensions.^{9,13–15}

For fluorescent imaging of single molecules, silica devices have a number of advantages compared to similar devices fabricated from polymers: the low autofluorescence of the device material increases the fluorescence signal-to-noise ratio,^{16,17} possibility of fusion bonding enables accurate control of channel dimensions,¹⁸ and the high stability and the hydrophilic character of silica make the devices compatible with numerous chemicals used in biology. Silica surfaces are therefore easily functionalized by grafting organic compounds, enabling control of the adhesion of biomolecules.¹⁹

By introducing a new class of materials for fabrication of lab-on-a-chip devices, we present a method that captures the best from both silica and polymer fabrication technologies: imprinting a sol–gel silica material,²⁰ we are able to fabricate all-silica fluidic devices, featuring both micro- and nanochannels, without use of any high-vacuum processes. Compared to top-down planar processing of silica or silicon substrates, sol–gel nanoimprint drastically reduces the number of process steps, and thus the fabrication costs, while preserving the excellent material properties of silica.

During imprint, thermally activated condensation of the hybrid sol–gel material leads to long-term stability. This

^aDTU Nanotech, Technical University of Denmark, DK-2800 Kongens Lyngby, Denmark. E-mail: anders.kristensen@nanotech.dtu.dk

^bLaboratoire Surface du Verre et Interfaces, Unité Mixte CNRS/Saint-Gobain, 39 quai Lucien Lefranc, F-93303 Aubervilliers Cedex, France. E-mail: elin.sondergard@saint-gobain.com

† Electronic supplementary information (ESI) available: Details on imprint process, characterization of imprinted sol–gel silica, and a study of structure deformation during annealing. See DOI: 10.1039/c1lc20689c

condensation process releases water from the material, and permeable stamps, *i.e.* PDMS,^{20,21} are typically used to allow diffusion of water vapor, which would otherwise produce defects.† The flexibility of a PDMS stamp, however, causes pronounced bending of the stamp at interfaces between micro- and nanostructures,²² which results in uneven imprinted surfaces that cannot be bonded to a lid.† Therefore, we have developed a process for imprinting of sol–gel materials with a rigid silicon stamp. The non-permeable stamp requires a thermal pre-treatment of the sol–gel material in order to reduce the water content before imprint. Using the silicon stamp, stamp bending is reduced and very good replication of both micro- and nanostructures with uneven density of pattern features is obtained. After imprint, annealing of the structured sol–gel material at 600 °C in an oxygen atmosphere calcinates the organics and produces a purely inorganic silica material, which can be fusion bonded to a thin glass cover slip to seal the channels.

Nanoimprint of sol–gel silica thus provides a cheap and easy way to produce high-quality silica nanofluidic devices for DNA-analysis.

2 Device fabrication

Previous works on nanostructuring thin films of sol–gel material include both direct imprint^{20,23} and reverse printing²⁴ techniques using PDMS stamps. Silicon stamps have previously been used for imprinting SiO₂–TiO₂ gel.²⁵ After imprint and condensation, the hybrid sol–gel material may be used as is²³ or it can go through a calcination process^{20,24,25} to obtain an inorganic material. For the DNA device, calcination is required in order to get low autofluorescence and enable fusion bonding.

These examples of previous work on sol–gel imprint have in common that free-standing nanostructures with a high density of free surfaces were produced. For imprinted channel structures, however, the free-surface density is very low, and this has a considerable impact on the structure deformation that takes place during the calcination process. This is further discussed in the ESI.†

As sketched in Fig. 1a, the fluidic device consists of an array of nanochannels, which is connected to four inlet holes by deeper microchannels in order to facilitate fluid transport in the device. The channels of different depths are fabricated in a single process step by imprinting a multi-level, hybrid stamp, as presented by

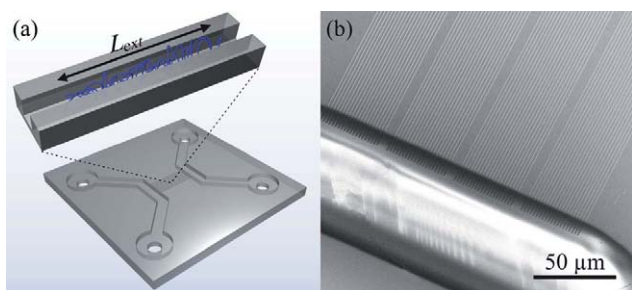


Fig. 1 (a) Cartoon of the fluidic device. Microchannels lead from four inlet holes to the array of nanochannels in the center. Confined in the nanochannels, DNA molecules stretch to the length L_{ext} along the channel. (b) Tilted SEM image of the hybrid stamp showing OrmoComp protrusion for imprint of microchannel (bottom) and SiO₂ protrusions for imprint of nanochannels (top).

Thamdrup *et al.*,¹⁰ in the sol–gel film. The hybrid stamp, which contains four devices, consists of a 500 μm thick 4-inch silicon substrate where nanostructures (100–250 nm line width) are defined by electron lithography and reactive-ion etching of thermally grown oxide (100 nm or 170 nm), and microstructures are made by UV-lithography of OrmoComp (micro resist technology), see Fig. 1b. OrmoComp protrusions of 600 nm height were made as a compromise between sufficient buffer flow in the final device and mechanical integrity of the silica films.† Molecular vapor deposition of FDTS (CAS no. 78560-44-8) prevents the sol–gel silica from sticking to the stamp.

The imprint process was developed to replicate the mixed micro- and nanostructures while maintaining a plane, bondable surface. A sketch of the process flow is found in the ESI.†

2.1 Preparation of sol–gel solution

Methyltriethoxysilane (MTES, CAS no. 2031-67-6) was mixed with a pH 2.0 HCl solution at a molar mixing ratio MTES : H₂O of 1 : 14 in a closed vial. At this acidity, hydrolysis of MTES is fast and condensation of the hydrolyzed precursor is rather slow.²¹ The two-phase system was vigorously stirred at 21 °C. After 5 min, a clear monophasic solution was obtained due to the hydrophilic character of hydrolyzed MTES. The sol–gel solution was left stirring for 4 h. During this aging, condensation between hydrolyzed precursors leads to formation of large oligomers and then of a gel network.²⁶

2.2 Spin-coating

Spin-coating of the sol–gel solution was performed in humidity-controlled clean room environment, and homogeneous coatings were obtained for solutions aged for 4 ± 0.5 h. Reproducible results were obtained for coatings performed within 15 min time-frames. Using a syringe, 2 ml of sol–gel solution was deposited on 4-inch fused silica or silicon substrates through a 0.2 μm polytetrafluoroethylene (PTFE) filter. Spinning at 2000 rpm, 500 rpm s⁻¹ acceleration, for 50 s produced high-quality 630 nm films with a wafer-scale standard deviation of 4 nm, measured by ellipsometry. The spin-coating process appeared to be sensitive to humidity: at 45% relative humidity (RH), the coated films were liquid (verified by the scratch-test method²¹), whereas, at 25% RH, the films were brittle after coating. Humidity monitoring and control is therefore advantageous to obtain reproducible coatings.

2.3 Drying and storage

After spin-coating, each substrate was immediately stored in a dry atmosphere to prevent material swelling, and hence increased condensation. This proved to be important for reproducibility. A nitrogen flow-box brought the relative humidity to 0.0% in a minute, and the coated substrates were dried for at least 30 min before imprint. Reproducible material properties were obtained for substrates stored at 0.0% RH for 30 min to 5 h.

2.4 Prebake

Before imprint, 5 min prebake of the coated substrates was performed at 90 °C to further dry and pre-cure the material.

Together with the dry storage, this process step is highly important for imprint of sol-gel with a non-permeable stamp. Films stored up to 5 h showed excellent reproducibility. Besides removal of water, the prebake is used to reach the correct gel state for adequate viscosity.^{21,27} A harder material may be convenient for imprint of, *e.g.*, very low protrusion coverage nanostructures. A gel film stored longer than 5 h in a nitrogen atmosphere may still be imprintable, but it needs a shorter prebake time. Correspondingly, a gel film that was not dried in nitrogen after spin-coating needs a longer precuring time to remove the water. However, both water content and condensation influence material flow during imprint.

2.5 Imprint

Imprint was performed using an EV Group 520 Hot Embosser. In order to get a reproducible temperature profile, the hot plates were preheated to the imprint temperature of 60 °C. At this temperature, compared to room temperature imprint, viscosity is decreased, but condensation is still low.²¹ Higher temperature thus improves material flow, despite the precuring. 0.5 mm graphite sheets were used as compliance layers on both sides of the imprint stack to homogeneously distribute the pressure. After loading the imprint stack, 2 min temperature equalization assured homogeneous temperature in stamp and substrate and allowed time for vacuum to be established in the chamber before 1.3 MPa pressure was applied. After 5 min imprint time, the stack was heated to 120 °C at 7 °C min⁻¹. The temperature was kept at 120 °C for 20 min to increase the degree of cross-linking of the material before cooling to 60 °C and releasing of pressure. This process allowed correct imprint of both micro- and nanostructures, see Fig. 2.

2.6 Demolding

Imprinted sol-gel material on silicon substrates was easily released from the stamp with a razor blade. However, triboelectric charging²⁸ during separation makes demolding of

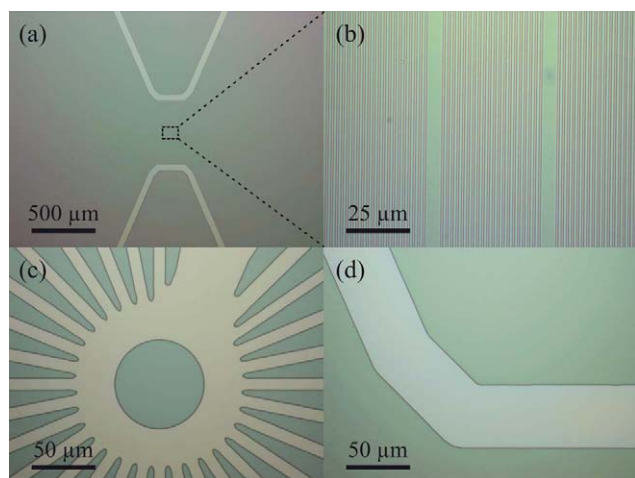


Fig. 2 Microscope images of (a) inlet channels and (b) nanochannels imprinted in sol-gel silica using hybrid stamp. (c-d) Details of inlet structures imprinted using silicon stamp.

insulating substrates more difficult due to electrostatic attraction. When imprinting gel films in the right state, the anti-sticking coating of the stamp is very durable: more than 75 imprints were made using the same FDTS coating on a silicon stamp. However, if imprinting too wet a gel film, self-assembly defects²⁹ may cause material to stick to the stamp. In this case, the hybrid stamps can be cleaned in Microposit Remover 1165 (*N*-methyl-2-pyrrolidone, CAS No. 872-50-4) with ultra sound, unless the gel is too condensed.

2.7 Annealing

After imprint, the sol-gel material is still a hybrid material, consisting of a silica matrix with one methyl and some hydroxyl side groups.

Annealing was carried out in a high-temperature furnace with an oxygen atmosphere. First, the material was heated at 1 °C min⁻¹ to 200 °C and held at that temperature for 2 h to fully condense the material and avoid reflow.^{27,30} Then it was heated at 5 °C min⁻¹ to 600 °C and held at that temperature for 4 h. Above 450 °C, the organics are calcinated. Using Fourier transform infrared spectroscopy, this can be seen as an extinction of the Si-CH₃ peak at 1250 cm⁻¹ in the spectrum shown in Fig. 3. After calcination, a purely inorganic silica material is left, indicated by the Si-O-Si peak at 1100 cm⁻¹. Condensation and the removal of organics cause a large volume reduction of the material. An unstructured film shrinks to 56% of its initial thickness.[†] Since the film of sol-gel silica adheres to the substrate, large compressive stress is induced. At high temperature, sintering also takes place, which causes some relaxation of the stress.²⁶

Reflow, shrinkage, and sintering thus cause a complex deformation of the imprinted structures. For imprinted nanochannels, the vertical channel dimension was almost unchanged during annealing, see Fig. 6d, whereas the horizontal channel dimension

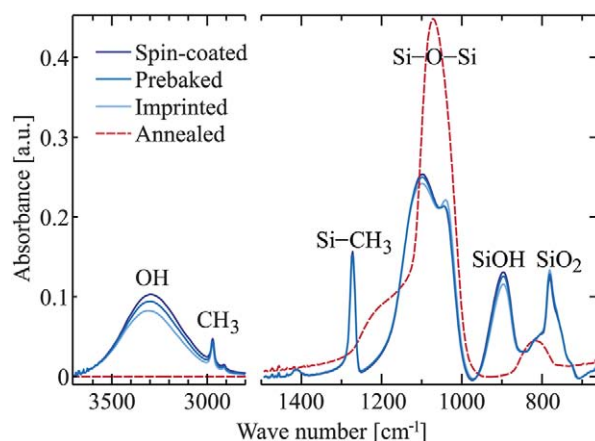


Fig. 3 Fourier transform infrared spectra of sol-gel silica at various stages of the imprint process. Decrease of the OH peak at 3300 cm⁻¹ shows reduction of water content during prebake. Condensation is seen as a decrease in the Si-OH peak at 900 cm⁻¹. Extinction of both of these peaks are seen after annealing. Calcination of the methyl side groups is seen as an extinction of the Si-CH₃ peak at 1250 cm⁻¹. After calcination, a pure silica material is left, indicated by the Si-O-Si peak at 1100 cm⁻¹.

appeared to depend strongly on the pattern density. Imprint depth and residual layer thickness also influence the channel deformation. The bonded nanochannel shown in Fig. 6e, of approximate dimensions of 390 nm by 170 nm, is the result of 150 nm wide, 170 nm high protrusions of 2 μm period imprinted in a 700 nm gel film. The inlet channels imprinted by 600 nm protrusions had shrunk to 350 nm depth after annealing.

A study of channel dimensions after annealing as function of pattern density is presented in the ESI.† The channel width as function of period is described by an error function. By increasing the pattern density, and hence increasing the density of free surfaces, the structure deformation during annealing is largely decreased and nearly vertical channel walls are obtained. Addition of dummy structures can thus improve the dimension control of the imprinted channels during annealing. Too large pattern density will, however, prevent the bonding of a lid from propagating on the imprinted surface. Another way to improve pattern replication could be to increase the free-surface density by adding a closed porosity to the sol-gel material.³¹ Despite a large degree of shrinkage, the structure deformation is very uniform for imprinted channels of equal period and dimensions. The standard deviation of channel widths measured by SEM was found to be less than 5%.

2.8 Device characterization

After annealing, the MTES sol-gel silica has an open microporosity. In order to characterize this porosity, ellipsometric measurements of refractive index were performed as a function of water partial pressure, see Fig. 4. By fitting a modified Kelvin equation to the data (Winelli 2 software, Sopralab), the average pore size was found to be below 2 nm. The porous volume fraction V_p was calculated using the Lorentz-Lorenz equation³²

$$V_p = 1 - \frac{(n_f^2 - 1)(n_s^2 + 2)}{(n_f^2 + 2)(n_s^2 - 1)}, \quad (1)$$

where n_f is the measured refractive index of the film and n_s is the refractive index of the skeleton. At zero water partial pressure, $n_f = 1.429$, see Fig. 4. Assuming that the refractive index of the

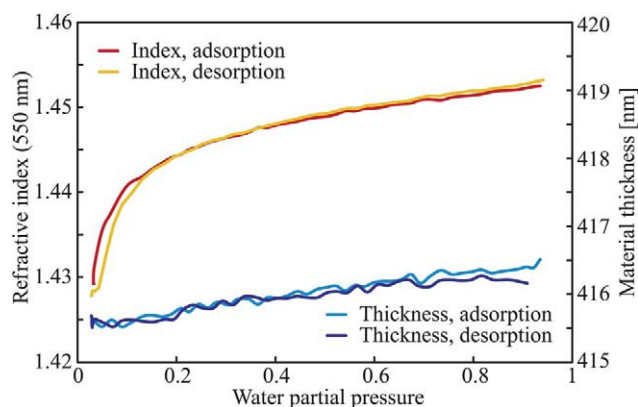


Fig. 4 Ellipsometric measurements of refractive index and thickness of annealed sol-gel silica film as function of water partial pressure.

skeleton is that of fused silica at 550 nm wavelength, $n_s = 1.460$, the porous fraction is calculated to be $V_p = 5.9\%$.

The imprinted device has a very smooth surface. Using atomic force microscopy (2 nm curvature radius SSS-NCH tip, NanoWorld), the surface roughness of imprinted and calcinated sol-gel silica was measured to $R_{\text{RMS}} = 1.16$ nm over a 12.5 μm^2 area (8000 data points) between two imprinted channels.

Using the same microscope setup as for the DNA experiments described below, autofluorescence of a 300 nm calcinated sol-gel silica film on a fused silica substrate was measured as a function of time. As seen in Fig. 5, autofluorescence of sol-gel silica did not deviate from what was measured on a fused silica substrate alone, and no time-dependence was observed. Both samples were heated to 600 $^{\circ}\text{C}$ the night before the measurement.

The final device, as shown in Fig. 6a,b, was fabricated by powder-blasting inlet holes in the imprinted substrate and fusion bonding a 157 μm polished cover slip to seal the channels.¹⁸

3 DNA confinement

DNA confinement experiments were performed on λ phage DNA (48.5 kbp, New England Biolabs) with persistence length $P = 50$ nm and monomer contour length $L = 16.5$ μm . Due to single-stranded, complementary segments at the ends of λ phage DNA, concatemers, which have contour lengths that are multiples of the monomer length, occur naturally in the DNA solution. The DNA was stained with YOYO-1 molecules (Molecular Probes) at a dye ratio of 1 dye molecule per 5 base pairs. Bis-intercalation of the dye molecules causes persistence and contour lengths to increase by 24%,¹⁰ yielding dye-adjusted lengths of $P_{\text{dye}} = 62$ nm and $L_{\text{dye}} = 20.5$ μm . The buffer used was 0.5 \times TBE (0.445 M tris-base, 0.445 M boric acid, and 10 mM EDTA) with

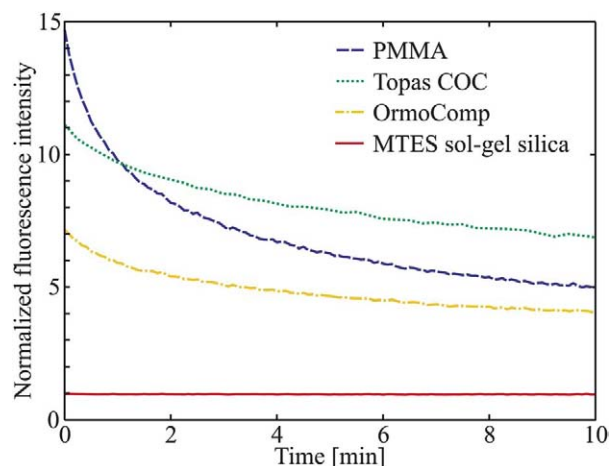


Fig. 5 Autofluorescence as a function of time for 300 nm films of PMMA (75k, Micro Resist Technology), Topas (cyclic olefin copolymer, grade 9506, Topas Advanced Polymers), OrmoComp (Micro Resist Technology), and annealed MTES sol-gel silica on fused silica substrates. Fluorescence intensities are normalized to that of a clean fused silica substrate. High levels of fluorescence intensity with a decrease over time, *i.e.*, bleaching, are seen for the organic and hybrid materials. In comparison, the annealed sol-gel silica film has a constant level of autofluorescence, identical to that of the substrate alone.

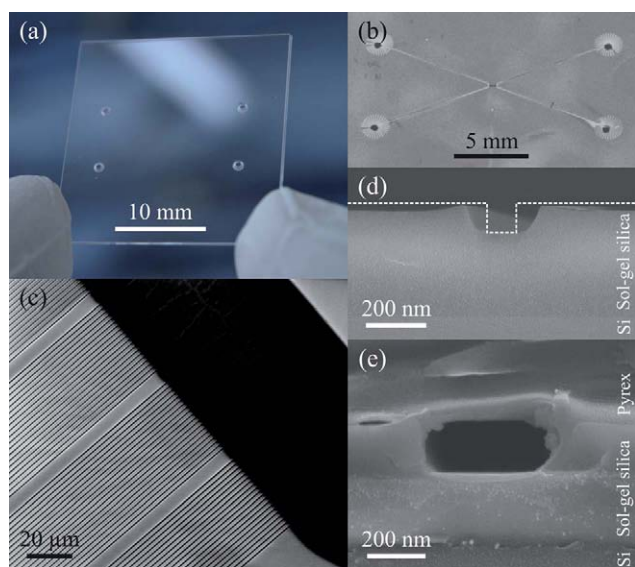


Fig. 6 Bonded sol-gel silica device on (a) fused silica substrate and (b) silicon substrate. 50 μm wide inlet channels lead from powder-blasted inlet holes to the nanochannel array in the center. (c) SEM image of imprinted and calcinated sol-gel silica device. Interface between inlet channel and arrays of imprinted nanochannels is shown. (d) Cross-sectional SEM image of imprinted and calcinated sol-gel silica nanochannel. Dashed line show cross-sectional profile of the imprinted 100 nm stamp protrusion for comparison. (e) Cross-sectional SEM image of sol-gel silica nanochannel, approx. 390 nm by 170 nm dimensions, bonded to a pyrex lid. The bonded device was cut with a saw, causing some material smear. A thin layer of gold was sputtered on samples before SEM imaging.

3% β -mercaptoethanol in order to reduce photodamage of the stained DNA.

In bulk solution, genomic length DNA coils up in a spherical conformation with a characteristic radius of gyration³³ $R_g \cong (P_{\text{dye}} w_{\text{eff}} L_{\text{dye}}^3)^{1/5}$, where w_{eff} is the effective width due to electrostatic repulsion, which is assumed to be 7.4 nm at the given buffer conditions.¹⁰ For λ phage DNA, $R_g \approx 1.3 \mu\text{m}$.

When DNA is confined to a nanofluidic channel of width w and height h , where the geometric average of the channel dimensions $D = \sqrt{wh}$ is smaller than R_g , but larger than the persistence length, the molecule is in the de Gennes confinement regime,³⁴ where the average extension of the molecule along the channel is given by³⁵

$$L_{\text{ext}} \cong L_{\text{dye}} \left(\frac{w_{\text{eff}} P_{\text{dye}}}{D^2} \right)^{1/3} \quad (2)$$

Thermal fluctuations will cause the molecule extension to vary around the average extension with a standard deviation given by¹

$$\sigma_{\text{ext}} \cong \sqrt{\frac{4L_{\text{dye}}}{15} (w_{\text{eff}} P_{\text{dye}} D)^{1/3}} \quad (3)$$

In the fabricated nanofluidic sol-gel silica device, measurements of the extension of confined DNA were performed using a Nikon Eclipse TE2000-U inverted microscope equipped with a 60 \times oil immersion 1.4 N.A. objective and a FITC filter cube (excitation: 465–495 nm, dichroic mirror: 505 nm, emission:

515–555 nm, Nikon). A metal halide light source (200 W, Prior Lumen) provided fluorescence excitation illumination. DNA molecules were transported into the nanochannels by applying air pressure at the device inlets. After letting the molecules relax to their equilibrium conformation, 500-frame movies were recorded at a frame rate of 10 Hz using an EMCCD camera (512 \times 512 pixels, Cascade II, Photometrics). In every frame, the molecule extension was measured by fitting a function to the fluorescence intensity profile, as described by Tegenfeldt *et al.*¹

The top panel of Fig. 7 shows histograms of the measured average extension of mono-, di-, tri-, and tetramers of λ phage DNA in sol-gel silica nanochannels as shown in Fig. 6e. The stretching corresponds to 17% of the dye-adjusted contour length. This is in good agreement with the 19% stretching predicted by eqn (2), calculated using $D^2 = 390 \text{ nm} \times 170 \text{ nm}$.

The bottom panel of Fig. 7 shows average standard deviation $\langle \sigma_{\text{ext}} \rangle$ for the extension measurement of each molecule as a function of the contour length L_{dye} . The average standard deviation is seen to follow eqn (3) with an additional prefactor of 1.36.

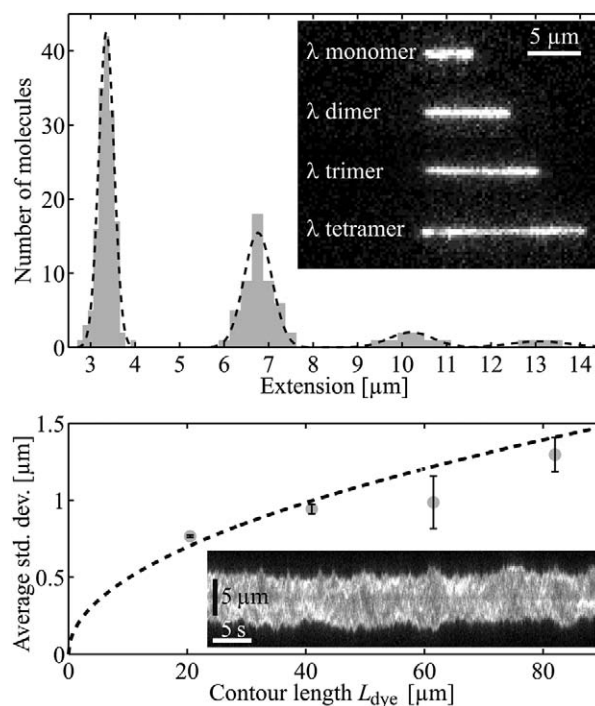


Fig. 7 Top panel shows histograms of measured average extension of λ phage DNA in sol-gel silica nanochannels. Dashed lines show Gaussian fits. Each measurement is based on 500 fluorescence images recorded at a frame rate of 10 Hz. Monomers (48.5 kbp, 156 molecules) are stretched to $\langle L_{\text{ext},1\lambda} \rangle = 3.37 \pm 0.17 \mu\text{m}$, dimers (97.0 kbp, 50 molecules) to $\langle L_{\text{ext},2\lambda} \rangle = 6.76 \pm 0.31 \mu\text{m}$, trimers (146 kbp, 4 molecules) to $\langle L_{\text{ext},3\lambda} \rangle = 10.20 \pm 0.49 \mu\text{m}$, and tetramers (194 kbp, 2 molecules) to $\langle L_{\text{ext},4\lambda} \rangle = 13.09 \pm 0.46 \mu\text{m}$. This corresponds to 17% of the dye-adjusted contour length. Fluorescence images of confined concatemers of λ phage DNA are inserted. Bottom panel shows average standard deviation σ_{ext} for the extension measurements of each molecule as a function of the contour length L_{dye} . Error bars show standard deviation of the mean. Dashed curve shows a fit of eqn (3) with a prefactor of 1.36. Inset shows time evolution of fluorescence intensity stripe for a λ phage dimer.

4 Conclusions

We have demonstrated a method for fabrication of micro- and nanofluidic silica devices by imprinting a sol-gel material with a non-permeable rigid stamp. By imprinting a multi-level stamp, channels of different depths are produced in a single process step and costly high-vacuum processes are avoided, thus making the fabrication much simpler and cheaper than top-down processing of fused silica or silicon substrates. Annealing of the imprinted hybrid sol-gel material in an oxygen atmosphere produces a purely inorganic silica material, which has very low auto-fluorescence and can be fusion bonded to a glass lid. Despite deformation of imprinted structures during annealing, high-quality devices were produced. The deformation is well described by an error function and it can be taken into account during the device design. Furthermore, we have devised methods to improve the pattern reliability during annealing by increasing the density of free surfaces in the material.

Extension measurements of DNA molecules confined in the nanochannels of the fabricated device were performed, and the measured lengths and standard deviations correspond well with theory. We have thus demonstrated that imprinted sol-gel silica devices are applicable for DNA-analysis and competitive to top-down processed silica devices.

Acknowledgements

The authors wish to acknowledge the financial support of the EC-funded project NaPANIL (Contract No. NMP2-LA-2008-214249) and the Danish Council for Technology and Innovation through the Innovation Consortium OCTOPUS. Furthermore, we wish to thank Ole Hansen for fruitful discussions.

References

- 1 J. O. Tegenfeldt, C. Prinz, H. Cao, S. Chou, W. W. Reisner, R. Riehn, Y. M. Wang, E. C. Cox, J. C. Sturm, P. Silberzan and R. H. Austin, *Proc. Natl. Acad. Sci. U. S. A.*, 2004, **101**, 10979–10983.
- 2 D. E. Streng, S. F. Lim, J. Pan, A. Karpusenka and R. Riehn, *Lab Chip*, 2009, **9**, 2772–2774.
- 3 R. Riehn, M. Lu, Y.-M. Wang, S. F. Lim, E. C. Cox and R. H. Austin, *Proc. Natl. Acad. Sci. U. S. A.*, 2005, **102**, 10012–10016.
- 4 Y. M. Wang, J. O. Tegenfeldt, W. Reisner, R. Riehn, X.-J. Guan, L. Guo, I. Golding, E. C. Cox, J. Sturm and R. H. Austin, *Proc. Natl. Acad. Sci. U. S. A.*, 2005, **102**, 9796–9801.
- 5 W. Reisner, N. B. Larsen, A. Silahtaroglu, A. Kristensen, N. Tommerup, J. O. Tegenfeldt and H. Flyvbjerg, *Proc. Natl. Acad. Sci. U. S. A.*, 2010, **107**, 13294–13299.
- 6 M. B. Mikkelsen, W. Reisner, H. Flyvbjerg and A. Kristensen, *Nano Lett.*, 2011, **11**, 1598–1602.
- 7 J. Han and H. G. Craighead, *Science*, 2000, **288**, 1026–1029.
- 8 J. Fu, R. B. Schoch, A. L. Stevens, S. R. Tannenbaum and J. Han, *Nat. Nanotechnol.*, 2007, **2**, 121–128.
- 9 D. Mijatovic, J. C. T. Eijkel and A. van den Berg, *Lab Chip*, 2005, **5**, 492–500.
- 10 L. H. Thamdrup, A. Klukowska and A. Kristensen, *Nanotechnology*, 2008, **19**, 125301.
- 11 P. Utiko, F. Persson, A. Kristensen and N. B. Larsen, *Lab Chip*, 2011, **11**, 303–308.
- 12 Y. Kim, K. S. Kim, K. L. Kounovsky, R. Chang, G. Y. Jung, J. J. dePablo, K. Jo and D. C. Schwartz, *Lab Chip*, 2011, **11**, 1721–1729.
- 13 A. R. Abate, D. Lee, T. Do, C. Holtze and D. A. Weitz, *Lab Chip*, 2008, **8**, 516–518.
- 14 R. Chantiwas, S. Park, S. A. Soper, B. C. Kim, S. Takayama, V. Sunkara, H. Hwang and Y.-K. Cho, *Chem. Soc. Rev.*, 2011, **40**, 3677–3702.
- 15 X. Wang, J. Jin, X. Li, X. Li, Y. Ou, Q. Tang, S. Fu and F. Gao, *Microelectron. Eng.*, 2011, **88**, 2427–2430.
- 16 K. R. Hawkins and P. Yager, *Lab Chip*, 2003, **3**, 248–252.
- 17 A. Piruska, I. Nikcevic, S. H. Lee, C. Ahn, W. R. Heineman, P. A. Limbach and C. J. Seliskar, *Lab Chip*, 2005, **5**, 1348–1354.
- 18 F. Persson, L. H. Thamdrup, M. B. L. Mikkelsen, S. E. Jarlgaard, P. Skafted-Pedersen, H. Bruus and A. Kristensen, *Nanotechnology*, 2007, **18**, 245301.
- 19 R. Marie, J. P. Beech, J. Vörös, J. O. Tegenfeldt and F. Höök, *Langmuir*, 2006, **22**, 10103–10108.
- 20 C. Peroz, C. Heitz, E. Barthel, E. Søndergård and V. Goletto, *J. Vac. Sci. Technol., B: Microelectron. Nanometer Struct.–Process., Meas., Phenom.*, 2007, **25**, L27–L30.
- 21 A. Letailleur, J. Teisseire, N. Chemin, E. Barthel and E. Søndergård, *Chem. Mater.*, 2010, **22**, 3143–3151.
- 22 S. Merino, A. Retolaza, A. Juarros and H. Schift, *Microelectron. Eng.*, 2008, **85**, 1892–1896.
- 23 M. Verschuuren and H. van Sprang, *Materials Research Society Symposia Proceedings*, 2007, **1002**, N03–N05.
- 24 C. Peroz, S. Dhuey, B. Harteneck and S. Cabrini, *Proceedings of the 53rd EIPBN Conference*, 2009.
- 25 M. Li, H. Tan, L. Chen, J. Wang and S. Y. Chou, *J. Vac. Sci. Technol., B*, 2003, **21**, 660–663.
- 26 C. J. Brinker and G. W. Scherer, *Sol-Gel Science: The Physics and Chemistry of Sol-Gel Processing*, Academic Press, San Diego, CA, 1990.
- 27 C. Peroz, V. Chauveau, E. Barthel and E. Søndergård, *Adv. Mater.*, 2009, **21**, 555–558.
- 28 B. Bhushan, *Nanotribology and nanomechanics: An introduction*, Springer-Verlag, Berlin, Heidelberg, 2008.
- 29 H. Schift, L. J. Heyderman, M. Auf der Maur and J. Gobrecht, *Nanotechnology*, 2001, **12**, 173–177.
- 30 J. Teisseire, A. Revaux, M. Foresti and E. Barthel, *Appl. Phys. Lett.*, 2011, **98**, 013106.
- 31 F. Guillemot, A. Brunet-Bruneau, E. Bourgeat-Lami, T. Gacoin, E. Barthel and J.-P. Boilot, *Chem. Mater.*, 2010, **22**, 2822–2828.
- 32 M. Born and E. Wolf, *Principles of Optics: Electromagnetic Theory of Propagation, Interference and Diffraction of Light*, Cambridge University Press, Cambridge, UK, 7th edn, 2005.
- 33 D. W. Schaefer, J. F. Joanny and P. Pincus, *Macromolecules*, 1980, **13**, 1280–1289.
- 34 W. Reisner, K. J. Morton, R. Riehn, Y. M. Wang, Z. Yu, M. Rosen, J. C. Sturm, S. Y. Chou, E. Frey and R. H. Austin, *Phys. Rev. Lett.*, 2005, **94**, 196101.
- 35 P.-G. de Gennes, *Scaling concepts in polymer physics*, Cornell University Press, Ithaca, NY, 1979.

Appendix C

Supplementary information for Paper 1

Supplementary information for: All-silica nanofluidic devices for DNA-analysis fabricated by imprint of sol-gel silica with silicon stamp

Supplementary information for: All-silica nanofluidic devices for DNA-analysis fabricated by imprint of sol-gel silica with silicon stamp

Morten Bo Mikkelsen,^a Alban A. Letailleur,^b Elin Søndergård,^b Etienne Barthel,^b Jérémie Teisseire,^b Rodolphe Marie,^a and Anders Kristensen^{*a}

1 Imprint process

Figure 1 shows the surface profile of imprints in sol-gel silica of equal $50\ \mu\text{m}$ wide, $600\ \text{nm}$ tall stamp protrusions of silicon and polydimethylsiloxane (PDMS) stamps. The flexibility of PDMS causes a much larger bending of the stamp, compared to a silicon stamp, which leads to a non-planar surface that could not be bonded to a glass lid. A rigid silicon stamp is therefore needed to produce surfaces of the right quality.

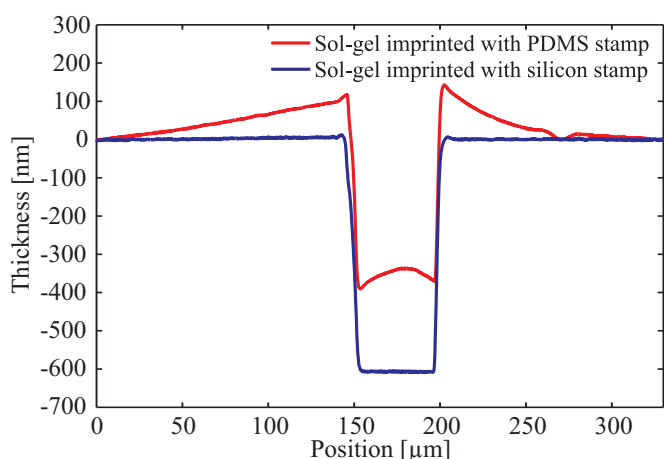


Fig. 1 Imprint of $50\ \mu\text{m}$ wide protrusion with PDMS stamp and silicon stamp.

Imprint of sol-gel silica with a non-permeable stamp is only possible if the water content of the material is reduced before imprint. Imprinting too wet a gel will give defects due to evaporating water and the sol-gel material may stick too the stamp. Surface defects due to evaporating water are shown in Fig. 2a.

However, if the gel is too cured or the water content is too small, viscosity is increased and material flow during imprint

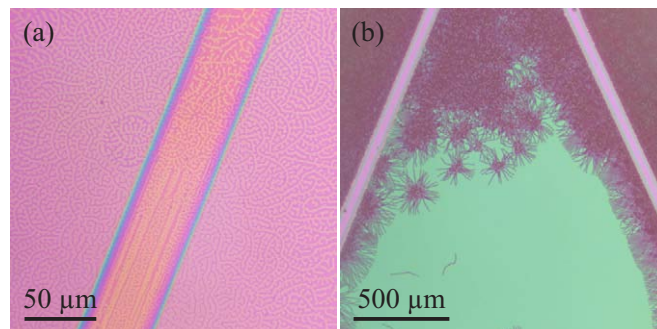


Fig. 2 (a) Too high water content of gel causes one type of surface defects during imprint. (b) Imprinting too cured a gel creates another type of surface defects.

is reduced. Furthermore, self-assembly defects, as shown in Fig. 2b, appear.

2 Deformation during annealing

For sol-gel thin films, which adhere to a substrate, compressive stress limits the thickness that can be obtained without the film cracking¹.

In an experiment, sol-gel silica films of different thickness were spin-coated on silicon substrates and annealed at 600°C in oxygen atmosphere. Figure 3 shows the final thickness after annealing as function of the initial film thickness. A linear shrinkage to 56% of the initial thickness is found.

The markers in Fig. 3 indicate the film quality after annealing. Circles show that films of initial thickness up to $700\ \text{nm}$ are perfectly crack-free. For films of initial thickness between $700\ \text{nm}$ and $1\ \mu\text{m}$, marked by triangles, cracks may occur in the bottom of imprinted structures or around other surface defects that serve as nucleation points, but as the thickness increases, cracks also appear in the middle of large unstructured areas. For films of initial thickness above $1\ \mu\text{m}$, marked by squares, narrow bands of material peel off and coil up, thereby creating glass wool on the substrate surface, as seen

^a DTU Nanotech, Technical University of Denmark, DK-2800 Kongens Lyngby, Denmark. E-mail: anders.kristensen@nanotech.dtu.dk

^b Laboratoire Surface du Verre et Interfaces, Unité Mixte CNRS/Saint-Gobain, 39 quai Lucien Lefranc, F-93303 Aubervilliers Cedex, France. E-mail: elin.sondergard@saint-gobain.com

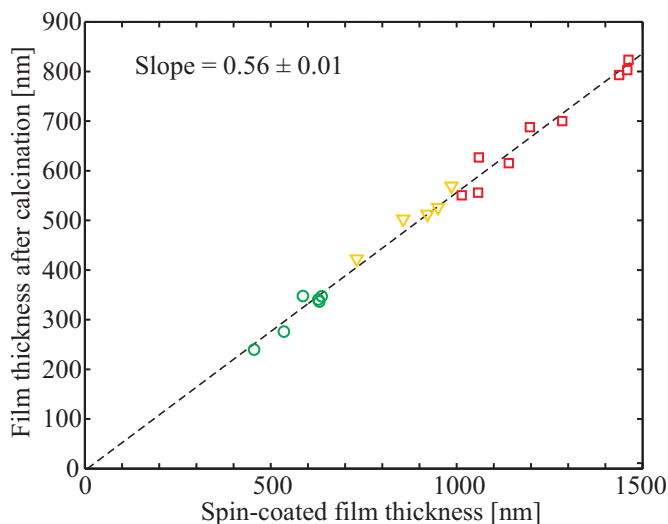


Fig. 3 Thickness of sol-gel silica films on silicon substrates measured after calcination at 600°C as function of the initial spin-coated thickness. A linear reduction of the film thickness to 56% is seen. Circles show crack-free films, triangles show films with few cracks around surface defects and imprinted structures, squares show films that produced glass wool.

in Fig. 4. During the annealing process, the cracking of films start at 400°C and happens during 10 min at 5°C/min temperature ramping. This corresponds well with the fact that calcination of the organics is expected to occur at temperatures above 400°C.

Cracking thus puts a limit to the thickness of sol-gel silica thin films of approximately 700 nm, corresponding to 400 nm final thickness. For sol-gel materials which are not clamped to a substrate, much larger items can be manufactured, since the free surfaces can accommodate for the shrinkage without introducing stress. An example of this is casting of bulk gels².

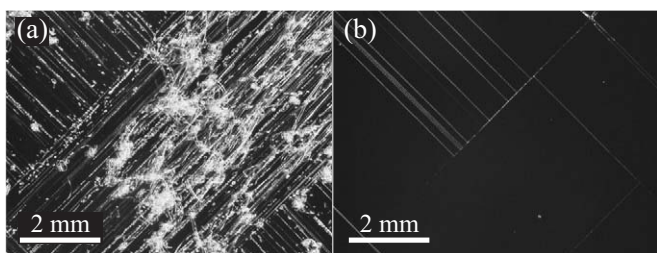


Fig. 4 Optical microscope images of calcinated sol-gel silica films of (a) 2 μm initial thickness and (b) 1 μm initial thickness. In (a), narrow bands of material peel off, following the $\langle 100 \rangle$ -directions of the silicon substrate, and coil up, creating glass wool on the surface. In (b), cracks occur along the same directions, but the material does not peel off. Image bottom lines are parallel to the substrate flats, *i.e.* the $\langle 110 \rangle$ -direction.

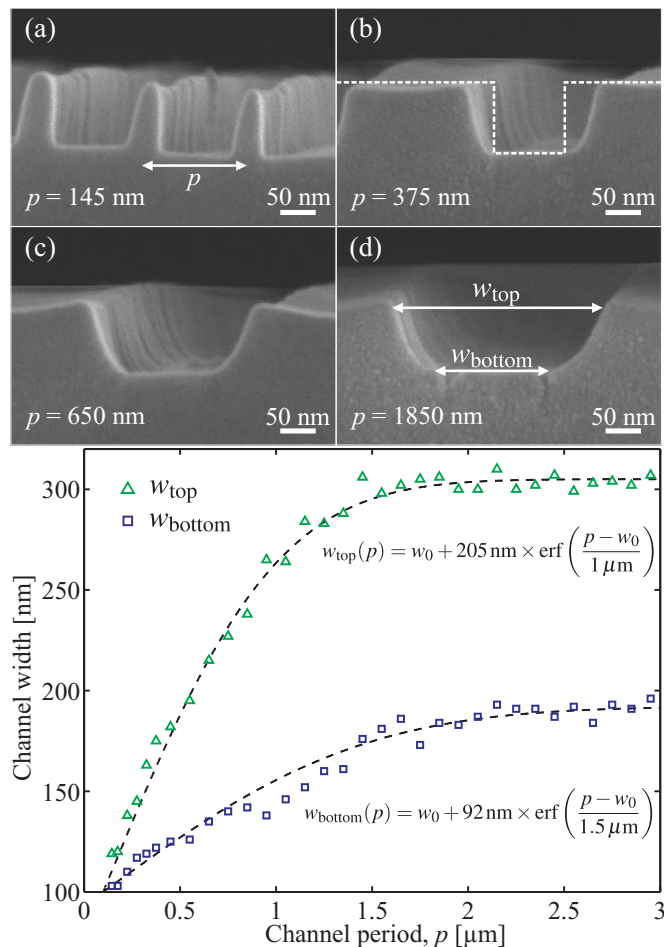


Fig. 5 SEM images (a-d) show cross-sectional views of calcinated imprints of $w_0 = 100$ nm wide, $h_0 = 100$ nm deep structures with increasing period p from (a) through (d). Dashed line in (b) shows cross-sectional profile of the stamp structure for comparison. The width of imprinted channels is seen to depend strongly on the period due to the deformation of sol-gel silica that takes place during the annealing process. The graph shows values of w_{top} and w_{bottom} , measured on the SEM images, as indicated in (d). The data are excellently fitted by the inserted error functions, which are shown with dashed lines.

Cracking of sol-gel silica films occurs equally frequent on silicon and fused silica substrates. However, where cracks on the amorphous fused silica substrate follow random paths, cracks on a $\langle 100 \rangle$ silicon substrate follows the $\langle 100 \rangle$ crystal directions, *i.e.* at a 45° angle to the primary flat, as seen in Fig. 4. This may be caused by an interplay between the anisotropic Young's modulus of silicon³, $E_{\langle 110 \rangle} = 169$ GPa and $E_{\langle 100 \rangle} = 130$ GPa, and the isotropic coefficient of thermal expansion⁴.

In the regions around imprinted channel structures, the deformation is more complex. Away from the surface structures,

all in-plane forces balance each other, and deformation only happens in the direction normal to the free surface. When channels are imprinted, vertical free surfaces are introduced, which will be deformed due to the compressive stress. However, at the bottom of the channel, less deformation is possible than at the top of the channel. The deformation depends on the free-surface density and hence on the amount of material next to the channel. This is shown in Fig. 5, where 100 nm wide, 100 nm deep channels with a period increasing from 145 nm to 3 μm were imprinted in a 700 nm sol-gel silica film and the resulting channel dimensions measured after annealing.

In Fig. 5a, the 100 nm wide channel imprinted at 145 nm average period has bottom width of 100 nm and top width of 115 nm. Next to it, a 25–40 nm wide, 95 nm tall, protruding line is seen, which was imprinted by a stamp cavity designed to be 40 nm by 100 nm. A high degree of dimensional control is thus possible for structures of small period, and nearly vertical side walls of the imprinted channels are obtained. For structures of large period, the deformation is much more pronounced: in Fig. 5d, the same 100 nm channel imprinted at 1850 nm period has bottom width of 166 nm and top width of 299 nm.

The bottom panel of Fig. 5 shows the channel widths measured at top and bottom as function of the period. It is seen that the data are excellently fitted by error functions, as shown by the dashed lines in the graph.

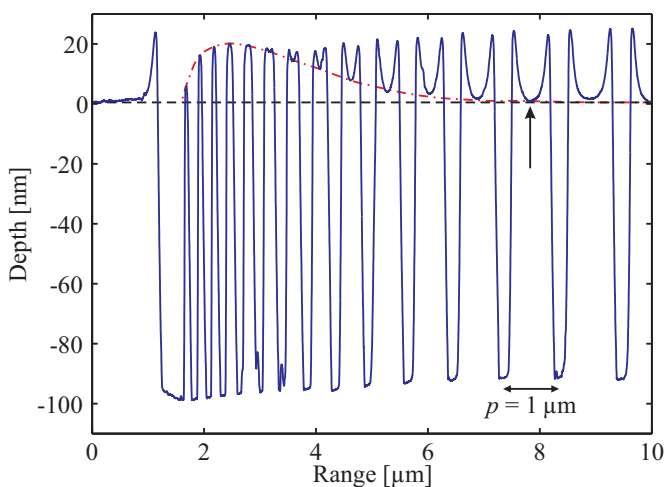


Fig. 6 AFM surface profile of the structures in Fig. 5. Horizontal dashed line indicates the surface level of the unstructured bulk areas of the film. Dash-dotted line shows the level of the centers of the protruding structures separating the channels. For periods $p > 1 \mu\text{m}$, corresponding to a structure widths larger than 900 nm, the level of the center of the structures reach the bulk surface level, as indicated by the arrow. Hence, for $p > 1 \mu\text{m}$, the structure deformation is independent of p , since the deformation of the edges only influences the outer approximately 450 nm of the material.

Figure 6 shows the surface profile, made by atomic force microscopy (AFM), of the same structures as in Fig. 5. It is seen that for periods $p > 1 \mu\text{m}$, corresponding to channel separations larger than 900 nm, the center levels of the protruding structures reach the bulk surface level. Hence, for $p > 1 \mu\text{m}$, the structure deformation is independent of p , since the deformation of the edges only influences the outer approximately 450 nm of the material. This corresponds to the $1 \mu\text{m}$ constant in the fit of $w_{\text{top}}(p)$.

3 Device fabrication

Figure 7 shows cross-sectional sketches of the process flow for fabrication of imprinted nanofluidic sol-gel silica devices. Channels of different depths are defined in the spin-coated gel film by imprinting of a multi-level hybrid stamp. Microprotrusions on the stamp are made by UV-lithography of Ormo-Comp and nanoprotusions are made by electron lithography and reactive-ion etching of thermally grown silicon dioxide⁶.

After demolding and annealing of the the imprinted sol-gel silica, the nanofluidic device is assembled in the same manner as devices fabricated by reactive-ion etching:^{7–9} Powder blasting¹⁰ through a masking tape is used for making inlet holes, and fusion bonding¹¹ is used to seal the channels by bonding of a polished cover slip to the imprinted sol-gel silica surface.

References

- 1 C. J. Brinker and G. W. Scherer, *Sol-Gel Science: The Physics and Chemistry of Sol-Gel Processing*, Academic Press, San Diego, CA, 1990.
- 2 T. Kreuzberger, A. Harnisch, M. Helgert, L. Erdmann and R. Brunner, *Microelectronic Engineering*, 2009, **86**, 1173 – 1175.
- 3 J. J. Wortman and R. A. Evans, *Journal of Applied Physics*, 1965, **36**, 153–156.
- 4 R. B. Roberts, *Journal of Physics D: Applied Physics*, 1981, **14**, L163.
- 5 M. Born and E. Wolf, *Principles of Optics: Electromagnetic Theory of Propagation, Interference and Diffraction of Light*, Cambridge University Press, Cambridge, UK, 7th edn., 2005.
- 6 L. H. Thamdrup, A. Klukowska and A. Kristensen, *Nanotechnology*, 2008, **19**, 125301.
- 7 J. O. Tegenfeldt, C. Prinz, H. Cao, S. Chou, W. W. Reisner, R. Riehn, Y. M. Wang, E. C. Cox, J. C. Sturm, P. Silberzan and R. H. Austin, *Proceedings of the National Academy of Sciences of the United States of America*, 2004, **101**, 10979–10983.
- 8 F. Persson, P. Utiko, W. Reisner, N. B. Larsen and A. Kristensen, *Nano Letters*, 2009, **9**, 1382–1385.
- 9 M. B. Mikkelsen, W. Reisner, H. Flyvbjerg and A. Kristensen, *Nano Letters*, 2011, **11**, 1598–1602.
- 10 F. Persson, L. H. Thamdrup, M. B. L. Mikkelsen, S. E. Jarlgaard, P. Skafte-Pedersen, H. Bruus and A. Kristensen, *Nanotechnology*, 2007, **18**, 245301.
- 11 A. Plöbl and G. Kräuter, *Materials Science and Engineering: R: Reports*, 1999, **25**, 1–88.

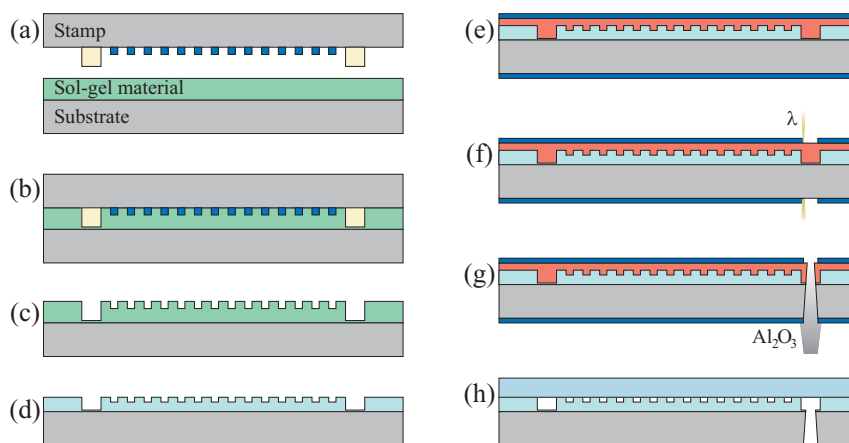


Fig. 7 Cross-sectional sketches of the process flow. (a) Imprint of multi-level hybrid stamp in spin-coated gel film. (b) Heating during imprint to cross-link the gel material. (c) Demolding of stamp. (d) Thermal annealing of gel at 600°C in oxygen atmosphere calcinates organics and produces pure silica. (e) Spin-coating of protective resist layer (red) and application of self-adhesive masking tape (blue, Nitto SWT-20). (f) Laser marking of tape using CO₂-laser ($\lambda = 10.6 \mu\text{m}$). Silicon substrates are transparent at this wavelength, enabling simultaneous marking of both sides. (g) Powder blasting of inlet holes through the masking tape using 110 μm Al₂O₃ particles. (h) Sealing of fluidic channels by fusion bonding of a polished 157 μm thick cover slip to the imprinted sol-gel silica surface. Subsequent thermal annealing at 550°C strengthens the bond.

Appendix D

Paper 2

Pressure-driven DNA in nanogroove arrays: complex dynamics leads to length- and topology-dependent separation

Supporting information and movies of DNA molecules are available at
<http://pubs.acs.org/doi/abs/10.1021/nl1044764>

Pressure-Driven DNA in Nanogroove Arrays: Complex Dynamics Leads to Length- and Topology-Dependent Separation

Morten Bo Mikkelsen,[†] Walter Reisner,[‡] Henrik Flyvbjerg,[†] and Anders Kristensen^{*,†}

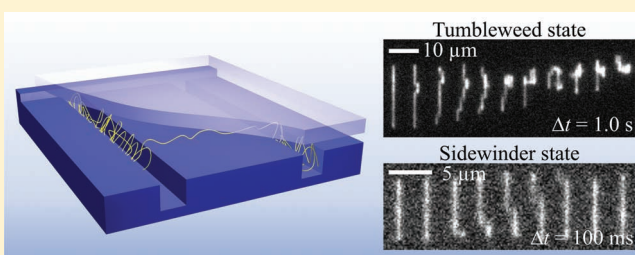
[†]DTU Nanotech, Technical University of Denmark, DK-2800 Kgs. Lyngby, Denmark

[‡]Department of Physics, McGill University, Montreal, Quebec H3A 2T8, Canada

S Supporting Information

ABSTRACT: The motion of linear and circular DNA molecules is studied under pressure driven buffer flow in a 50 nm slit channel with arrays of transverse 150 nm deep nanogrooves. Transport occurs through two states of propagation unique to this nanogroove geometry, a slow, stepwise groove-to-groove translation called the “sidewinder” and a fast, continuous tumbling across the grooves called the “tumbleweed”. Dynamical transitions between the two states are observed at fixed buffer velocity. Molecules exhibit size- and topology-dependent velocities.

KEYWORDS: Confined DNA, transport dynamics, entropic trapping, separation, complex dynamics, emergent behavior



Nanoconfinement is a powerful tool for controlling polymer conformation and dynamics in lab-on-a-chip type devices for the analysis of DNA and other biomolecules. When a polymer is confined to a space with a dimension below the polymer’s gyration radius, the static conformation of the chain will be extended perpendicular to the confinement axis and the chain entropy will be reduced. In sufficiently small nanochannels, for example, DNA will spontaneously stretch,^{1–4} creating an extension along the channel linear with the molecule contour length.⁵ Nanochannel devices are thus a convenient platform for performing physical mapping of DNA.^{6,7} In addition, varying confinement in a chip will create global entropy variation and hence free energy gradients that can locally trap DNA, that is, entropic trapping,^{8,9} or drive DNA from confined to open regions of a chip, that is, entropic recoil.¹⁰

In this letter, we present a device that combines such local manipulation of DNA conformation with entropic trapping.⁸ It consists of an array of 150 nm deep and 75–600 nm wide nanogrooves in the bottom of an open slit, see Figure 1. The depth of the slit ($d_s = 50$ nm) is less than the groove depth ($d_g = 150$ nm), so that in equilibrium a molecule is both extended along a groove and entropically trapped in it. As a molecule is only entropically confined, at sufficient buffer flow, it is driven out of its groove. This leads to a unique form of motion in which an extended molecule is driven transverse to its axis of extension.

In the classic entropic trapping geometry of Han and Craighead,⁸ consisting of traps with lateral dimensions greater than the polymer radius of gyration, the trapped conformation exists in a coil state abutting the slit Figure 2e,f. This coil conformation is approximately that of an unconfined polymer if the field strength in the traps is weak.¹¹ Larger molecules have a greater probability of escaping the traps than smaller molecules, as larger coils abut

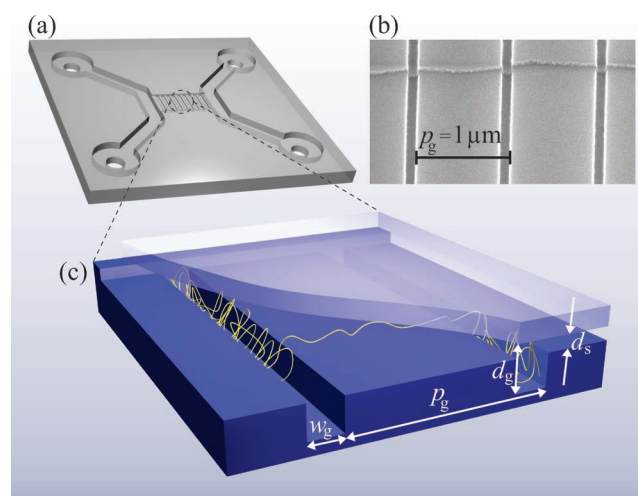


Figure 1. (a) Cartoon of the fluidic device showing inlet reservoirs and microchannels leading to the 450 μm long and 50 μm wide nanoslit. (b) SEM micrograph showing edge of nanoslit and transverse nanogrooves. (c) Cartoon of nanogroove channel with stretched DNA being transported from one groove to the next. Slit depth $d_s = 50$ nm, groove depth $d_g = 150$ nm, groove width w_g is varied from 75 to 600 nm, and periodicity p_g is varied between 1 and 2.6 μm .

a greater slit surface and hence have a greater probability of forming herniations in the slit that lead to escape.^{8,11} This classic

Received: December 22, 2010

Revised: February 14, 2011

Published: March 01, 2011

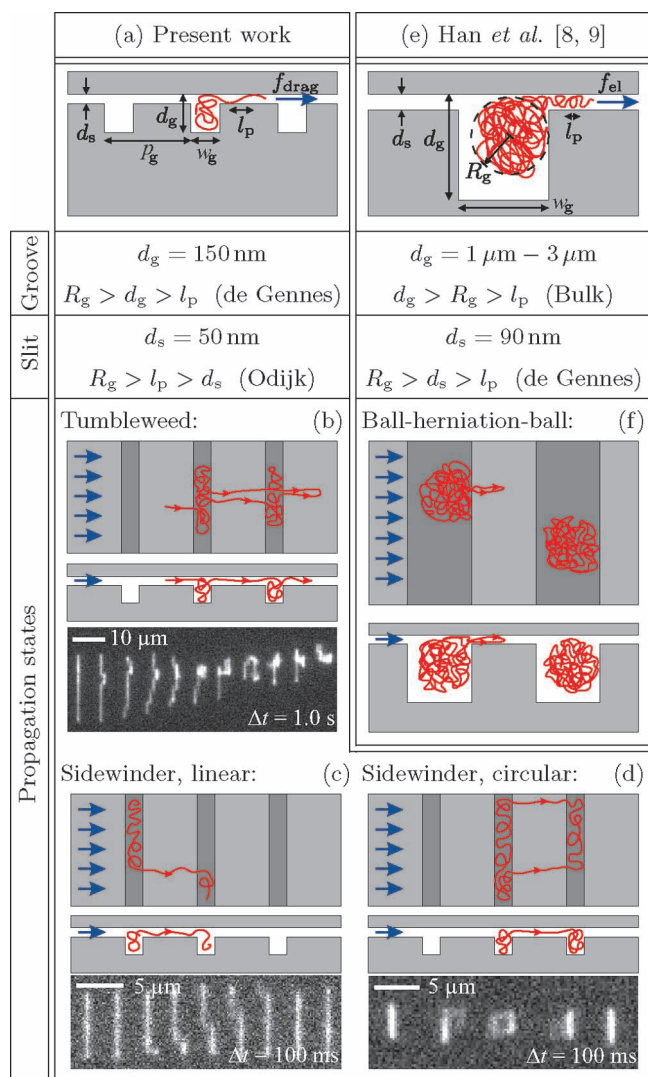


Figure 2. Propagation states of DNA in various geometries. Arrowheads on DNA (red lines) indicate direction of motion of DNA that flows in response to buffer flow shown as blue arrows. (a) Alternating de Gennes and Odijk confinement regimes¹ stretch DNA in front of the slit, which gives rise to two distinct propagation states, the folded tumbleweed state (b), and the stretched sidewinder state in the case of (c) linear DNA and (d) circular DNA. This contrasts with the single propagation state (f) seen in Han and Craighead's device (e), in which alternating bulk and de Gennes regimes allow DNA to coil in a ball conformation in front of the slit, and transport through the slit is initiated by herniation from the ball. l_p is persistence length and R_g gyration radius.

geometry has been utilized to perform size separations for DNA in the 1–100 kbp size range for both batch¹² and continuous flow separation modes.¹³

In contrast, our nanogroove geometry alters the confined DNA conformation by extending the molecule in the entropic trap, giving rise to a qualitatively different transport physics. In particular, we observe a new type of self-organized dynamical behavior of a single polymer chain. The hundreds of degrees of freedom of a DNA molecule alternate between a state where an extended DNA molecule can make stochastic hops based on escape of its free ends, which we call the “sidewinder” (Figure 2c,d), and a compact highly folded state propagating at constant velocity, which we call the “tumbleweed” (Figure 2b). From a fundamental point-of-view,

this system demonstrates that features of complex dynamical behavior^{14,15} can arise in the context of motion of a single polymer chain under a constant driving force in a periodic potential landscape.

While pure motion in either state exhibits a size-independent velocity at fixed buffer velocity, the dynamic interplay between the two states creates a size-dependent velocity that can be utilized for separation. In particular, we show that our device can perform separations based on polymer topology; linear and topologically circular DNA molecules of the same size migrate at different speeds in the nanogroove arrays. This is a striking feature unique to the nanogroove geometry; the classic entropic trapping geometry is in principle much less sensitive to polymer topology. While circular DNA has a slightly more compact conformation in bulk than linear DNA, which should lead to an increased trapping lifetime and a lower migration velocity in the classic geometry, the difference is small; the radii of gyration of ideal linear and circular chains differ by only a factor of $(2)^{1/2}$.¹⁶

Molecule Dynamics. When a solution of DNA is driven through the nanogroove device at buffer velocities below the threshold for escape,¹⁷ a molecule remains extended in the nanogroove while buffer circulates through the slit; see Supporting Information for movie files and experimental conditions. This regime could be used for physical mapping of the extended DNA while performing real-time buffer exchanges. As buffer velocity is slowly increased above the threshold for escape for linear DNA, end-escape becomes most probable and the molecule will enter the sidewinder state; the escape of a molecule-end prompts a groove-to-groove translation, repeats of which give rise to a motion similar to that of a sidewinder rattlesnake, see Movie2 in Supporting Information. This state of motion is slow and its average velocity is independent of molecule length, because most time is spent waiting for end-escape to occur.

As buffer velocity is still further increased, herniation of contour from the molecule midsection into the adjacent groove can occur. At low buffer velocity, contour transport is slow and herniation will most likely lead to a sidewinder transition, see Movie4 in Supporting Information. But if the herniated segment that flows into the adjacent groove flows there too fast to stretch out in the groove as fast as it arrives, the DNA contour in the groove may locally be folded back on itself. Such an increase in local base pair concentration increases self-avoidance interactions, hence decreases the free energy differential between DNA in nanogroove and slit, so that this locally folded DNA is locally less confined. Consequently, there is a high probability of additional herniation of contour from this folded region of the molecule, see Movie8 in Supporting Information. Thus, at sufficient buffer speed once they have formed regions of folded DNA will tend to remain and self-propagate in a characteristic continuously “tumbling” state of motion: the tumbleweed state. Reversions of the tumbleweed to the sidewinder occurs, for example, if an end-escape occurs and pulls contour out of folded segments before they prompt the next herniation.

Alternations between the two states occur during the dynamics, see Movie1 in Supporting Information, with the tumbleweed becoming dominant as the buffer velocity is increased. Moreover, the longer the molecule, the more probable is herniation as opposed to end-escape¹⁸ and the more likely it is for the molecule to have folded and compressed regions. As observed, the faster tumbleweed state is thus more probable for longer molecules.

Circular DNA can escape via herniation to a circular equivalent of the sidewinder state, see Figure 2d. Propagating circular DNA

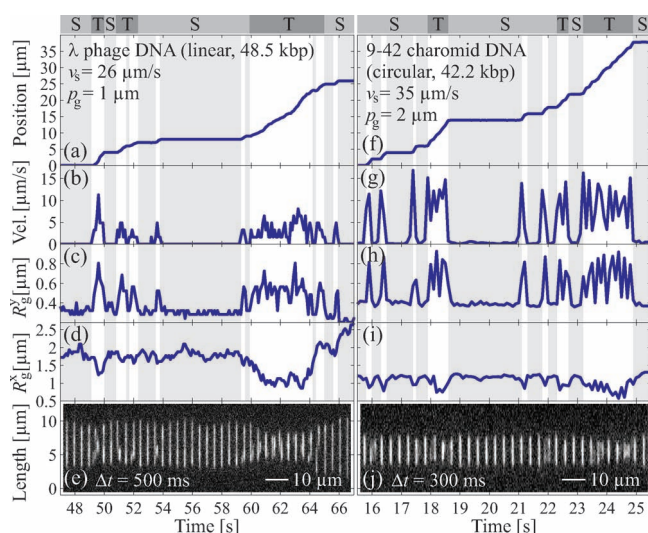


Figure 3. Data extracted from movies of linear λ -DNA (a–e) and circular 9-42 charomid DNA (f–j) in slit channels with groove period p_g and buffer velocity v_s . Gray background indicates trapping of molecule and confinement to a single groove. Bar on top indicates the state of the molecules, tumbleweed (T) or sidewinder (S). Graphs have time resolution $\Delta t = 100$ ms and show the molecules' center-of-mass positions, velocities, and radii of gyration along (R_g^x) and perpendicular (R_g^y) to the grooves. (e,j) Fluorescence image montages corresponding to graphs.

can also form tumbleweed states when herniated strands in the adjacent nanogroove undergo additional folding, see Movie10 in Supporting Information.

Single Molecule Analysis. Figure 3 shows center-of-mass positions, velocities, and radii of gyration along (R_g^x) and perpendicular (R_g^y) to the grooves for two molecules with different topologies, linear and circular. For both molecules, these plots qualitatively demonstrate the existence of the two states of motion, tumbleweed (T) and sidewinder (S), as indicated on the top bar, as well as dynamic transitions between them. The data analysis protocol is described in Section 3 in Supporting Information.

The sidewinder state is characterized by single-groove transitions, during which velocity and R_g^y shortly increase while the molecule spans two grooves. R_g^x decreases only slightly during transitions because the molecule is in equilibrium in both grooves. The circular molecule has a greater decrease in R_g^x because of its shorter extension.

The tumbleweed state is characterized by the continuous propagation across multiple grooves of a compressed molecule. Compression is seen as an elevated intensity in the fluorescence images, but it also reduces the molecule's extension along the grooves, resulting in the decrease of R_g^x to roughly half the equilibrium extension, while velocity and R_g^y remain high.

Using these criteria to identify sidewinders and tumbleweeds, we can quantitatively demonstrate that they are two distinct states of propagation. The time a molecule is trapped in a single groove, waiting to escape, is referred to as its dwell time τ . The widths of gray areas in Figure 3 are dwell times. Histograms of observed dwell times are shown in Figure 4 panels a and d for linear and circular DNA, respectively. Dwell times are random and exponentially distributed, $p(\tau) \propto \exp(-\tau/\bar{\tau})$, for $\tau > 0.9$ s. This exponential distribution is proof that a molecule, which has dwelled longer than 0.9 s, has constant probability of escape per unit time, independent of how long it has been trapped, that is, escape is a Poisson process.

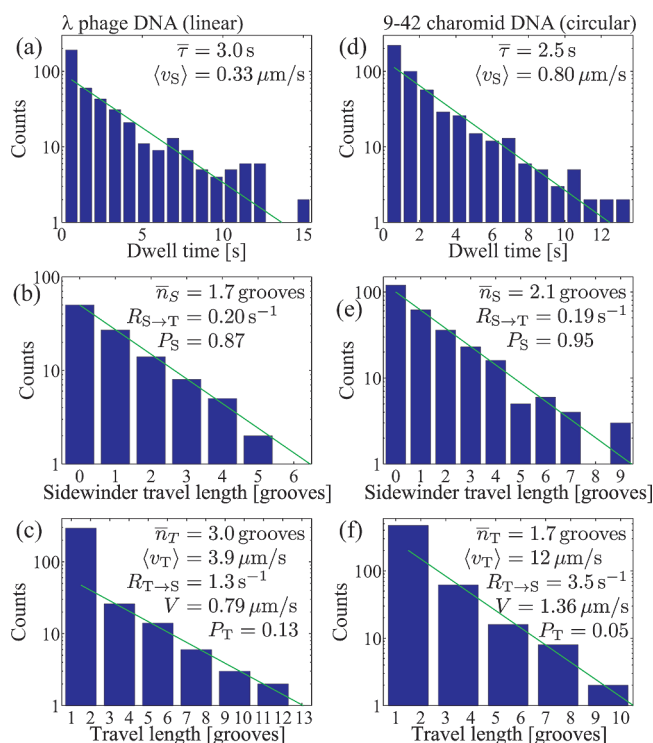


Figure 4. Histograms of dwell time τ , sidewinder travel length n_s , and tumbleweed travel length n_T . (a–c) λ -DNA with $p_g = 1$ μm and $v_s = 26$ $\mu\text{m/s}$. (d–f) Circular 9-42 charomid DNA with $p_g = 2$ μm and $v_s = 35$ $\mu\text{m/s}$. Characteristic times, transition rates, and probabilities given in panels characterize the exponential fits shown. Calculated velocities V correspond well to the measured values $\langle v_{\text{lin}} \rangle = 0.87$ $\mu\text{m/s}$ and $\langle v_{\text{circ}} \rangle = 1.66$ $\mu\text{m/s}$.

Such a molecule must be in equilibrium with itself in the groove or its behavior would not be time-invariant. The count of dwell times less than 0.9 s exceeds the number predicted by the exponential distribution. The excess count could be attributed to molecules that were compressed or folded a little when they landed in the groove. This makes them escape with the higher escape rate that folds and compression give rise to, before they have relaxed to equilibrium. This tumbleweed-like feature could make them tumbleweeds but with sidewinder features if we used a different cutoff in our classifier of states. The average velocity of DNA in the sidewinder state is given by $\langle v_s \rangle = p_g/\bar{\tau}$, where p_g is the distance between neighboring grooves.

Figure 4 panels b and e show histograms of the number n_s of sidewinder transitions made by a molecule between two consecutive periods in the tumbleweed state. Both histograms show clearly that n_s is a random integer with exponential distribution. Thus the transition from the sidewinder to the tumbleweed state is also a Poisson process. Its transition rate is $R_{S \rightarrow T} = \langle v_s \rangle / (p_g \bar{n}_s)$.

Figure 4 panels c and f show histograms of distances n_T traveled by individual tumbleweeds between two consecutive periods of dwelling as a sidewinder in a nanogroove. The integer n_T measures distance in units of the nanogroove separation p_g . It is a random number with exponential probability distribution of values exceeding two groove periods. Thus the transition from the tumbleweed to the sidewinder state is also a Poisson process, showing that the DNA molecule is in a state of dynamical equilibrium with itself when it travels as a tumbleweed. The count of molecules traveling only one or two groove periods greatly exceeds the count suggested by the shown exponential

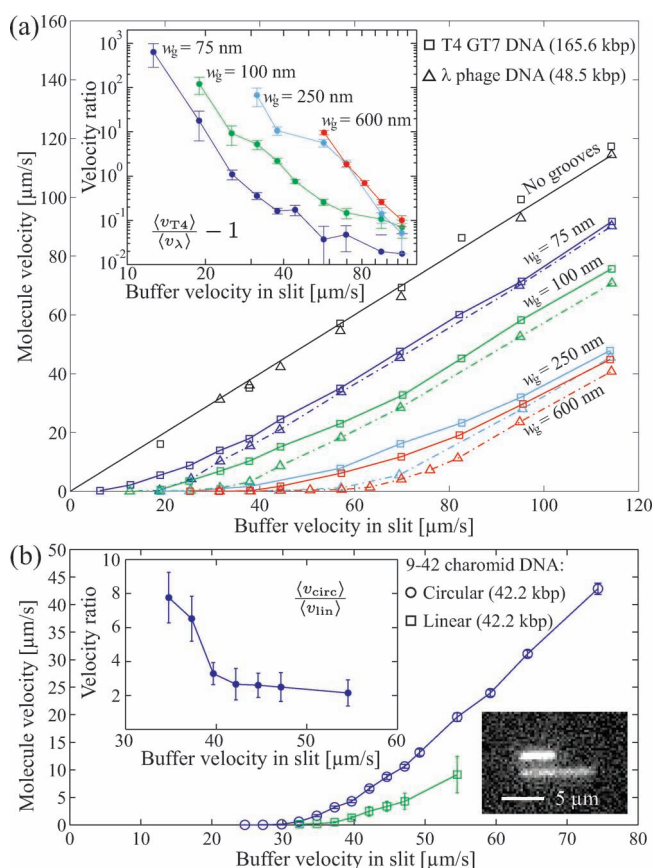


Figure 5. (a) Molecule velocity as function of buffer velocity in groove arrays of different width w_g . Groove period $p_g = w_g + 2 \mu\text{m}$. Insert shows velocity ratio between T4 GT7-DNA and λ -DNA $\langle v_{T4} \rangle / \langle v_{\lambda} \rangle - 1$ in a double-logarithmic plot. Velocity ratios of the order of 100 are seen for 75 nm grooves. Data based on movies of 1702 λ -DNA and 1460 T4 GT7-DNA molecules. Buffer velocity measured as the average molecule velocity in a groove-free region of the slit channel. (b) Molecule velocity as function of buffer velocity for circular (intact) and linear (broken once) 9-42 charomid DNA. Fluorescence image shows circular DNA (top) and linear DNA (bottom) trapped in adjacent grooves. $w_g = 100$ nm and $p_g = 2 \mu\text{m}$. Inserted graph shows velocity ratio of circular and linear molecules $\langle v_{circ} \rangle / \langle v_{lin} \rangle$. Data based on movies of 479 circular and 69 linear 9-42 charomid DNA molecules.

distribution. The excess is due to DNA in the sidewinder state, compressed or folded enough to fool our filter. Some of these molecules make two consecutive groove transitions with so brief a dwelling time between that the molecule registers as a tumbleweed. Molecules traveling longer than two groove periods are bona fide tumbleweeds with a transition rate back to the sidewinder state given by $R_{T \rightarrow S} = \langle v_T \rangle / (p_g \bar{n}_T)$, where $\langle v_T \rangle$ is the average velocity of DNA in the tumbleweed state.

The exponentially distributed travel lengths of sidewinders and tumbleweeds show that they are two distinct dynamic states. Both linear λ -DNA and circular 9-42 charomid DNA molecules are seen to randomly alternate between these two states at a given buffer velocity. Many molecules will intermittently be borderline cases. This does not challenge the existence of the two states but shows that their borderline is not sharp. That does not prevent separation based on the different transport properties of sidewinders and tumbleweeds, see Section 5 in Supporting Information, because the average state of motion of a molecule is biased toward one state or the other.

With P_S as the probability of being in a sidewinder state and P_T as the probability of being in a tumbleweed state, detailed balance gives $P_T R_{T \rightarrow S} = P_S R_{S \rightarrow T}$ with $P_S + P_T = 1$. The molecule velocity is then determined by $V = \langle v_S \rangle P_S + \langle v_T \rangle P_T$.

Ensemble Analysis. Figure 5a shows average velocities as function of buffer velocity for λ -DNA and T4 GT7-DNA in a slit channel with groove arrays of different width w_g . The arrays are placed in series to ensure equal buffer velocities in slit regions.

At low buffer velocity, only sidewinders exist and propagation is very slow. As soon as tumbleweeds form, which happens at a length-dependent threshold, they dominate the dynamics since $\langle v_T \rangle \gg \langle v_S \rangle$. This results in the very large velocity ratio $\langle v_{T4} \rangle / \langle v_{\lambda} \rangle - 1$ shown as insert in Figure 5a. In the regime of high buffer velocity, only tumbleweeds exist, and molecules reach a length-independent velocity, experiencing the nanogrooves as an effective friction, see Section 4 in Supporting Information. Increasing groove width increases the free energy difference between groove and slit, hence shifts threshold buffer velocities to higher values.

Figure 5b compares average velocities of linear and circular 9-42 charomid DNA molecules. The higher basepair-concentration of circular DNA¹⁹ reduces the free energy difference between contours in the groove and in the slit. Consequently, the escape probability of circular DNA is higher than that of linear DNA. The velocity ratio $\langle v_{circ} \rangle / \langle v_{lin} \rangle = 8$ at $v_s = 35 \mu\text{m/s}$ shows that the system can be used for separation of linear and circular molecules; see Movie9 in Supporting Information. This difference is much greater than would be expected for the classic entropic trapping geometry. In the classic geometry, we would expect the mobility μ of linear and circular molecules to differ by no more than 30%, with the bound arising from the ratio of the radii of gyration of ideal linear and circular chains ($\mu_{circ} / \mu_{lin} > R_g^{circ} / R_g^{lin} \sim 1/(2)^{1/2} \approx 0.7$).

Conclusion. We have found and characterized two distinct states of motion, sidewinder and tumbleweed, which are observed for both linear and circular DNA molecules in nanogroove arrays. The characteristic features of these states emerge as the many degrees of freedom of the polymer interact repeatedly with the nanotopology. The demonstrated device can be used for molecule filtering, DNA separation, and sample preparation. In particular, it possesses the unique property that motion of DNA in the arrays is sensitive to molecule topology as well as size.

■ ASSOCIATED CONTENT

S Supporting Information. Movie files and details on experiments and data analysis. This material is available free of charge via the Internet at <http://pubs.acs.org>.

■ AUTHOR INFORMATION

Corresponding Author

*E-mail: anders.kristensen@nanotech.dtu.dk.

■ ACKNOWLEDGMENT

The work was partly funded by the Danish Council for Technology and Innovation through the Innovation Consortium OCTOPUS, by the Danish Research Council for Technology and Production, FTP Grant 274-05-0375, and by the European Commission funded project READNA (Contract HEALTH-F4-2008-201418).

■ REFERENCES

- (1) Reisner, W.; Morton, K. J.; Riehn, R.; Wang, Y. M.; Yu, Z.; Rosen, M.; Sturm, J. C.; Chou, S. Y.; Frey, E.; Austin, R. H. *Phys. Rev. Lett.* **2005**, *94*, No. 196101.
- (2) Reisner, W.; Beech, J. P.; Larsen, N. B.; Flyvbjerg, H.; Kristensen, A.; Teegenfeldt, J. O. *Phys. Rev. Lett.* **2007**, *99*, No. 058302.
- (3) Jo, K.; Dhingra, D. M.; Odijk, T.; de Pablo, J. J.; Graham, M. D.; Runnheim, R.; Forrest, D.; Schwartz, D. C. *Proc. Natl. Acad. Sci. U.S.A.* **2007**, *104*, 2673–2678.
- (4) Krishnan, M.; Mönch, I.; Schwille, P. *Nano Lett.* **2007**, *7*, 1270–1275.
- (5) Teegenfeldt, J. O.; Prinz, C.; Cao, H.; Chou, S.; Reisner, W. W.; Riehn, R.; Wang, Y. M.; Cox, E. C.; Sturm, J. C.; Silberzan, P.; Austin, R. H. *Proc. Natl. Acad. Sci. U.S.A.* **2004**, *101*, 10979–10983.
- (6) Riehn, R.; Lu, M.; Wang, Y.-M.; Lim, S. F.; Cox, E. C.; Austin, R. H. *Proc. Natl. Acad. Sci. U.S.A.* **2005**, *102*, 10012–10016.
- (7) Wang, Y. M.; Teegenfeldt, J. O.; Reisner, W.; Riehn, R.; Guan, X.-J.; Guo, L.; Golding, I.; Cox, E. C.; Sturm, J.; Austin, R. H. *Proc. Natl. Acad. Sci. U.S.A.* **2005**, *102*, 9796–9801.
- (8) Han, J.; Turner, S.; Craighead, H. *Phys. Rev. Lett.* **1999**, *83*, 1688–1691.
- (9) Han, J.; Craighead, H. G. *Science* **2000**, *288*, 1026–1029.
- (10) Turner, S. W. P.; Cabodi, M.; Craighead, H. G. *Phys. Rev. Lett.* **2002**, *88*, No. 128103.
- (11) Han, J.; Craighead, H. G. *Anal. Chem.* **2002**, *74*, 394–401.
- (12) Fu, J.; Yoo, J.; Han, J. *Phys. Rev. Lett.* **2006**, *97*, No. 018103.
- (13) Fu, J.; Schoch, R. B.; Stevens, A. L.; Tannenbaum, S. R.; Han, J. *Nat Nanotechnol.* **2007**, *2*, 121–128.
- (14) Schaller, V.; Weber, C.; Semmrich, C.; Frey, E.; Bausch, A. R. *Nature* **2010**, *467*, 73–77.
- (15) Haken, H. *Synergetics, an Introduction: Nonequilibrium Phase Transitions and Self-Organization in Physics, Chemistry, and Biology*, 3rd ed.; Springer series in synergetics; Springer-Verlag: New York, 1983.
- (16) M. Rubinstein, R. H. C. *Polymer Physics*; Oxford University Press: New York, 2003.
- (17) Sakaue, T. *Eur. Phys. J. E* **2006**, *19*, 477–487.
- (18) Sebastian, K. L.; Paul, A. K. R. *Phys. Rev. E: Stat. Phys., Plasmas, Fluids, Relat. Interdiscip. Top.* **2000**, *62*, 927–939.
- (19) Persson, F.; Utko, P.; Reisner, W.; Larsen, N. B.; Kristensen, A. *Nano Lett.* **2009**, *9*, 1382–1385.

Appendix E

Paper 3

Controlled deposition of sol-gel sensor material using hemi-wicking

Controlled deposition of sol–gel sensor material using hemiwicking

Morten Bo Mikkelsen¹, Rodolphe Marie¹, Jan H Hansen²,
Dorota Wencel³, Colette McDonagh³, Hans Ole Nielsen² and
Anders Kristensen¹

¹ DTU Nanotech, Technical University of Denmark, DK-2800 Kgs. Lyngby, Denmark

² DELTA, DK-2970 Hørsholm, Denmark

³ Optical Sensors Laboratory, National Centre for Sensor Research, School of Physical Sciences, Dublin City University, Collins Avenue, Glasnevin, Dublin 9, Ireland

E-mail: anders.kristensen@nanotech.dtu.dk

Received 1 June 2011, in final form 16 August 2011

Published 5 October 2011

Online at stacks.iop.org/JMM/21/115008

Abstract

Optical sensors are fabricated by depositing liquid sol–gel sensor material on a polycarbonate surface, which has been decorated with arrays of periodic micropillars. Using the principle of hemiwicking, the liquid material is spread, guided by the surface structures, to homogeneously fill the volume between the surface structures and form a liquid film with a thickness determined by the height of the micropillars. After evaporation of solvents, a uniform layer of sensor material resides on the surface. This fabrication method enables easy and reproducible deposits of isolated spots of different sensor materials of precise thickness to be made on plastic surfaces, and it provides an improved method for fabricating cheap optical sensors integrated in disposable lab containers.

(Some figures in this article are in colour only in the electronic version)

1. Introduction

In reagent-based optical sensing systems, a change in the optical response of an intermediate agent, e.g., an analyte-sensitive dye molecule, is used to monitor the analyte concentration. Such reagent dyes can be immobilized in a solid matrix of sol–gel silica that is permeable to the analyte, thus making an optical sensor material. In a liquid form, sol–gel-based materials can be coated on a wide range of substrates, which makes this kind of optical sensor materials very versatile [1].

In biotech applications such as, e.g., cell culturing [2], constant monitoring of pH and dissolved oxygen is of great importance. Sol–gel-based sensor materials for measuring these analytes [3, 4] enable fabrication of cheap optical sensors, which can be integrated in disposable lab ware, such as cultivation bags, shake flasks and petri dishes. Using integrated sensors, invasive probes are avoided and sources of contamination are reduced, since the sensors are disposable and optically read from the outside of the container.

Coatings of sol–gel material can be produced using dip-, spray-, or spin-coating [5–7], and homogeneous thin films of sol–gel sensor material, which are required for obtaining fast and uniform response times of the optical sensors, have been demonstrated on dip-coated substrates [4]. However, for deposition of sensor material on the inside of containers, or when several different sensor materials are to be deposited in separate areas on the same surface, these coating methods are not feasible. In present commercial applications of this sensor technology^{4, 5} patches with sensor material are fabricated and manually glued to the inside of containers.

We present a method for deposition of liquid sensor material on a homogeneous layer in a well-defined region of a surface. By decorating the surface with periodic micropillars and using the principle of hemiwicking [8], a drop of liquid material that is deposited on the microstructured surface will spread, guided by the structures, to homogeneously fill the

⁴ PreSens Precision Sensing GmbH, Regensburg, Germany. <http://www.presens.de>

⁵ Sartorius AG Goettingen, Germany. <http://www.sartorius-mechatronics.com>

volume between the structures. Spreading of the liquid is governed by the geometry of the microstructures and surface energy, and the thickness of the deposited film is determined by the height of the micropillars and is thus independent of the volume of the deposited drop. This enables easy and reproducible deposits of spots of the sol–gel sensor material of precise thickness to be made on plastic surfaces.

Microstructuring of the inside of blow-molded plastic containers may be performed using step-and-stamp imprint lithography [9], and for plastic components produced by injection molding, microstructures can be integrated directly in the mold [10]. Both of these fabrication methods are suited for large-scale industrial production.

Spreading by hemiwicking thus enables direct, controlled deposition of spots of the sol–gel sensor material inside containers, and it simplifies the fabrication of optical sensors in disposable lab ware.

2. Hemiwicking of sol–gel material

Hemiwicking is the phenomenon of liquid being imbibed and spread by a surface texture, and it has previously been studied in relation to wetting of surfaces [8, 11, 12] and controlled spreading of liquids [13, 14]. In this paper, we use hemiwicking to produce films of liquid sol–gel sensor material with well-defined thickness. When deposited on a surface, the sol–gel material is a liquid mixture of solvents, i.e. water and ethanol, and solutes. After evaporation of the solvents, the solid–gel matrix, containing the analyte-sensitive dye molecules, remains deposited between the microstructures.

When a drop of liquid is deposited on top of a microstructured surface, some of the liquid will penetrate into the surface texture to wet the microstructures, provided that the equilibrium contact angle between the liquid and surface $\theta_{eq} < \pi/2$, while the remaining drop lies as a spherical cap on top of the microstructures. The front of the penetrating liquid will continue to propagate within the surface structure, minimizing surface energy, until it reaches the edges of the drop. However, if θ_{eq} is smaller than a critical angle θ_c , as described in [11], hemiwicking is favorable, and the liquid front will continue to spread within the surface structure beyond the extent of the drop. A liquid film is thus formed over the surface, between the microstructures, while the drop is drained. This is sketched in figure 1(a) in the case of a surface with a periodic array of micropillars.

Surface structures can pin a contact line, and for disconnected structures like the array of pillars, the liquid front must be activated to continue the progression. For wetting liquids, this is made possible via the meniscus forming around each pillar. In order for the contact line to continue the progression, the meniscus must be able to extend from one row of pillars to the next [12]. Assuming zero mean curvature of the meniscus, the condition for the sufficient extension is $h/l > \tan \theta_{eq}$ on an array of micropillars of height h , radius r and period $d = l + 2r$, as sketched in figure 1(b). Before attaining the equilibrium contact angle, the advancing contact line will thus reach the next row of pillars, which will be wetted, and the liquid front will continue to propagate on the

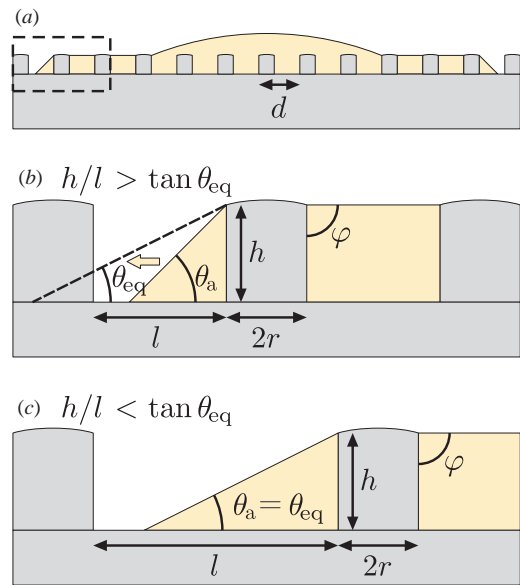


Figure 1. (a) Cross-sectional sketch of a drop of liquid deposited on a two-dimensional array of micropillars of height h , radius r and period $d = l + 2r$. Driven by surface energy, a liquid film self-propagates within the microtexture, spreading the liquid and draining the drop, which lies as a spherical cap on top of the pillars. (b) Enlarged view of the dashed box in (a) showing the liquid front in the case of $h/l > \tan \theta_{eq}$. The contact angle of the advancing liquid front θ_a is larger than the equilibrium contact angle θ_{eq} , and the liquid front will reach the next row of pillars before attaining θ_{eq} . The next row of pillars will thus be wetted, and the propagation continues on the other side. In (c), the same situation is shown for a different geometry with $h/l < \tan \theta_{eq}$. In this case, the liquid front is pinned when $\theta_a = \theta_{eq}$ and the propagation is stopped. At the top of the pillars, the contact line is pinned by the corner, and surface energy forces $\varphi = 90^\circ$, producing a flat air–liquid interface.

other side. This will proceed until the drop, which was initially on top of the pillars, has been drained completely and all the liquid has been imbibed by the microstructure, provided that the inter-pillar volume is large enough to contain the drop volume.

The contact line at the top of the pillars is pinned by the corner, so that the contact angle φ is not limited to θ_{eq} but can take a wide range of values [8, 15]. For narrow structures, surface energy forces $\varphi = 90^\circ$, producing a flat air–liquid interface [14]. The pillar height h thus exclusively determines the thickness of the deposited liquid layer. The volume of the deposited drop controls the size of the wetted area, but it does not affect the deposited material thickness. Hemiwicking can thus be used for producing liquid films of precise thickness [8].

In the case of a geometry with $h/l < \tan \theta_{eq}$, as sketched in figure 1(c), the liquid front gets pinned when the advancing contact angle θ_a equals θ_{eq} , and propagation stops before the next row of pillars is reached [13]. The same situation is found when a spreading liquid reaches the edge of the structured area. However, propagation may continue in other directions on the structured surface, and filling of the surface structure is hence not sensitive to alignment as long as the liquid is deposited inside the patterned area.

To create a uniform film of sensor material by hemiwicking, it is required that the solvent evaporation of the deposited sol–gel material occurs much slower than the spreading of the material. Otherwise, evaporation during spreading will result in inhomogeneous sensor spots. The propagation speed of the spreading liquid film increases with h/l [13], and hence the geometry of the surface structures can be optimized to minimize the spreading time.

3. Optimization of surface structures

In order to find the optimal surface structures for fabricating sensor spots by uniform spreading of sol–gel sensor material, the material was deposited on a series of 7 mm diameter arrays of pillars of different dimensions and periods, which were fabricated by thermal imprint lithography [16] on a polycarbonate foil. Polycarbonate was chosen since it is a common material for laboratory bottles. Using a Krüss DSA 10 drop shape analyzer, the contact angle of the ETEOS-based sol–gel oxygen sensor material described in [4] was measured to be $\theta_{eq} = 12^\circ \pm 3^\circ$ on a flat polycarbonate surface. The solvents of the sol–gel material, i.e. water and ethanol, evaporate from a $0.5 \mu\text{l}$ drop in 10 s.

Four-inch silicon stamps with structure heights ranging between 10 and $50 \mu\text{m}$, each containing different square lattice and hexagonal lattice geometries, were fabricated using UV lithography and dry etching. Pillar radii and periods were chosen to make ratios of h/l ranging from 0.06 to 5. For all geometries, θ_{eq} is smaller than θ_c , thus making hemiwicking possible. A fluorosilane coating was applied to the stamp surface by molecular vapor deposition to prevent sticking of the polymer. Imprints were made in $255 \mu\text{m}$ thick sheets of polycarbonate at 170°C and 1.3 MPa for 5 min, before cooling the imprint stack to 120°C and demolding.

Deposition of the sensor material on the structured polycarbonate foil was performed using an Eppendorf pipette, and best results were obtained by filtering the sensor material with a $0.1 \mu\text{m}$ PTFE syringe filter and deposition in a clean room to avoid dust defects in the coating. After deposition, the sol–gel material was fully dried and condensed by heating to 110°C for 18 h.

Figure 2 shows examples of depositions of the sensor material on microstructures of different geometries. Like in [13] and [14], we find that the ability of a given geometry to homogeneously spread the sensor material mainly depends on the ratio of h/l , and for structures of equal h/l , it is relatively independent of pillar height and lattice pattern, i.e. rectangular or hexagonal. As shown in figure 2, the deposition results can therefore be grouped into four regimes of h/l in relation to the equilibrium contact angle $\tan \theta_{eq} \approx 0.2$.

- For $h/l < \tan \theta_{eq}$, the liquid front gets pinned as sketched in figure 1(c), and propagation beyond the drop is not possible. Evaporation causes uneven material distribution with ring deposits as described in [17].
- For $\tan \theta_{eq} < h/l < 0.5$, metastable pinning by the pillars happens easily, and propagation is slow and very sensitive to the lattice pattern. This favors formation of polygonal shapes of the deposited material, as described

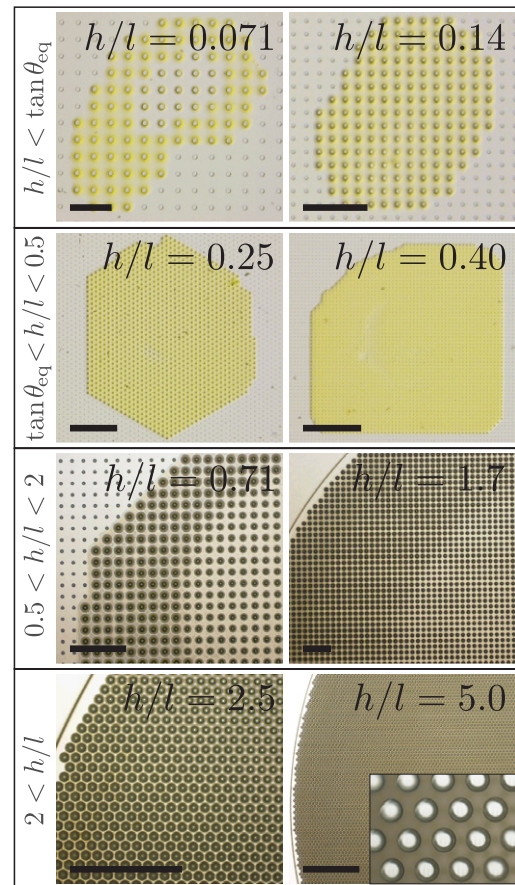


Figure 2. Top view of the sol–gel sensor material deposited on a polycarbonate foil with regions of different pillar geometries. The deposition results are grouped into four regimes, depending on the ratio of h/l in relation to $\tan \theta_{eq} \approx 0.2$. Homogeneous spreading of the sensor material is only obtained for surface structures with $h/l > 2$, as shown in the bottom row. Scale bars show $500 \mu\text{m}$.

in [13]. Unless the deposited volume is small, spreading is incomplete and material is left on top of the surface structures.

- For $0.5 < h/l < 2$, the deposited material spreads independently of the lattice pattern to form a round deposition area. This is in correspondence with [13] for increased h/l . However, the material distribution is uneven, with the deposit being homogeneous at the center but denser at the perimeter. The inhomogeneity diminishes as h/l is increased.
- For $2 < h/l$, very homogeneous layers are produced.

Figure 2 shows that the homogeneity of the deposited film increases as the ratio of h/l is increased. We explain this tendency by the increasing propagation speed for increasing h/l [13]. For small h/l , the spreading time is large, and much of the solvent evaporates while the material is spreading. The solid content of the liquid material thus increases as the film progresses, resulting in an inhomogeneous deposition. Evaporation-induced redistribution of material, as described in [17], may also play a role. At high h/l , the spreading time is small, and less solvent evaporates during spreading. Most of the solvent thus evaporates from the material after a uniform

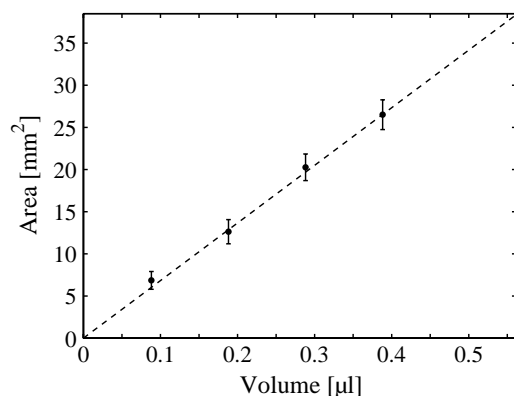


Figure 3. Spreading area as function of volume of oxygen sensor material deposited on a polycarbonate foil with the optimized surface microstructures. Deposition is performed using a 0.1 µl–2.5 µl-range Eppendorf pipette. The data are corrected for capillary filling of the pipette tip, which added approximately 0.09 µl to the volume reading on the pipette. Error bars show standard deviation. The dashed line shows the expected spreading area $A = V / (h [1 - \phi_S])$, where V is the deposited volume, $\phi_S = 2\pi r^2 / (\sqrt{3}d^2)$, $h = 23 \mu\text{m}$, $r = 9.5 \mu\text{m}$ and $d = 30 \mu\text{m}$. Axis limits correspond to the volume/area of the microstructures of each sensor spot.

film has been made. Uniform evaporation rates over the film result in homogeneous material deposition, considering length scales larger than period d of the pillars. Between the pillars, on length scales smaller than d , non-uniform evaporation may cause redistribution of material [17].

Evaporation time depends on the volatility of the solvents and the thickness of the liquid film, and spreading time depends on the distance, contact angle and liquid viscosity. The mentioned regimes of h/l are therefore only valid for the specific structures and materials.

Based on the uniformity of the depositions of sensor material on different surface structures and the sensing performance of the fabricated sensor spots, the best results were obtained with a hexagonal lattice with $h = 23 \mu\text{m}$, $r = 9.5 \mu\text{m}$, $d = 30 \mu\text{m}$ and $h/l = 2.1$. This structure is further characterized in the following sections.

4. Characterization of material deposition

In figure 3, the spreading area is plotted as a function of four different volumes of the sensor material deposited on the optimized microstructure. The linear relation between volume and area shows that spreading of the liquid only occurs as long as the deposited drop can be drained, and the filling stops once all liquid is inside the pillar volume. The excellent agreement between experimental and theoretical spreading areas indicates that the liquid film is uniformly distributed with a film thickness controlled by the pillar height.

If the volume of the deposited sensor material cannot be contained in the inter-pillar volume of a sensor area, the excess material will not spread but stay where deposited on top of the microstructures, thus producing a non-uniformity. Deposited volumes of the sensor material must, therefore, not exceed

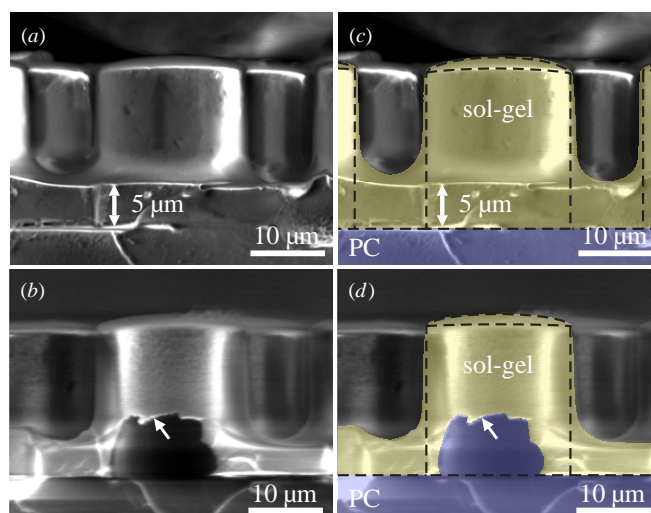


Figure 4. (a), (b) Cross-sectional SEM images of condensed sol-gel oxygen sensor material deposited on 23 µm high, 19 µm wide pillars imprinted in polycarbonate (PC) foil. (c) and (d) show same images as (a) and (b), but with overlaid colors to highlight the PC substrate and pillars (blue) and the sol-gel coating (yellow). Dashed lines show outline of the front row of pillars. (a), (c) After evaporation of solvents, the thickness of the deposited sensor material is 5 µm. Between the pillars, menisci are seen. (b), (d) The fracture shows that a thin film of sensor material has been deposited on the vertical side walls of the pillars, indicated by the arrow. Due to the ductility of the PC foil, cleavage was difficult and could only be performed during immersion in liquid nitrogen.

the 0.56 µl required to completely fill the 7 mm diameter microstructured area.

Figure 4 shows cross-sectional SEM images of the condensed sol-gel sensor material on the 23 µm high and 19 µm wide polycarbonate structures. The thickness of the sensor material is measured to be $\ell = 5 \mu\text{m}$ at the center between the pillars. It is seen that the vertical sidewalls have been coated by a layer of sensor material with a thickness of the order of a few hundred nanometers, and at the bottom between the pillars, the surface is meniscus-shaped as sketched in figure 5. The material thickness is thus inhomogeneous within each unit cell of the pillar array. However, this inhomogeneity is repeated in every unit cell, so when averaging over length scales larger than the period $d = 30 \mu\text{m}$, the material distribution can be considered homogeneous.

For thin films, fluorescence intensity is proportional to material thickness [18], and measurements of the fluorescence intensity of the sensor material were utilized to get a qualitative evaluation of the thickness homogeneity. Fluorescence images recorded with a CCD camera make it possible to evaluate the homogeneity on different length scales.

Fluorescence images were recorded using a Nikon Eclipse inverted fluorescence microscope, equipped with a metal halide light source and a Photometrics-cooled EMCCD camera, and a Nikon TRITC filter cube was used to isolate the fluorescence signal at 620 nm [19] of the Ru(II)-tris(4,7-diphenyl-1,10-phenanthroline) in the oxygen sensor material. A 4× objective with numerical aperture of 0.13 was used for

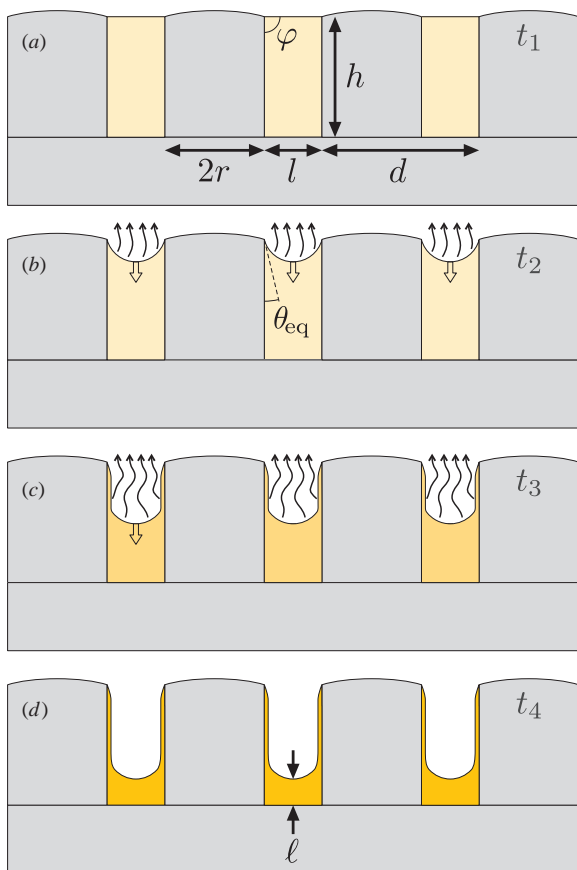


Figure 5. (a) During filling of the microstructure, the air–liquid interface is flat, as sketched in figure 1. When the solvent evaporates, the decreasing liquid level moves the contact line away from the top corner of the pillar and forces the contact angle to θ_{eq} , thus creating the meniscus sketched in (b). (c) As the meniscus descends, a thin film is deposited on the vertical sidewalls of the pillars like in a dip-coating process [5]. The solid content of the liquid increases, as indicated by the darker color. (d) The meniscus-shaped surface is maintained while the solid phase of the sensor material condensates and dries completely at the bottom of the pillars.

obtaining a large field of view and large depth of focus, which is convenient for imaging curved surfaces.

On each sensor spot, five fluorescence images were taken, as shown in the top panel of figure 6. The bottom panel of figure 6 shows intensity histograms of the images (a)–(e). The narrow peak centered at intensity 9.20 au comes from the pillars (dark), where no sensor material is present and only the auto-fluorescence of the polycarbonate substrate produces a signal. This peak thus serves as a reference signal, since it is independent of the deposited sensor material. The much broader peak centered around intensity 13.70 au comes from the fluorescence of the sensor material (bright). Broadening of the peak at intensity 13.70 au is caused by the thickness variation within each unit cell, produced by the conformal deposition seen in figure 4, but also by inhomogeneity of the light source as well as defects and dust particles on both sides of the substrate. However, particle defects will not displace the peak, due to their small area, but only decrease the peak height.

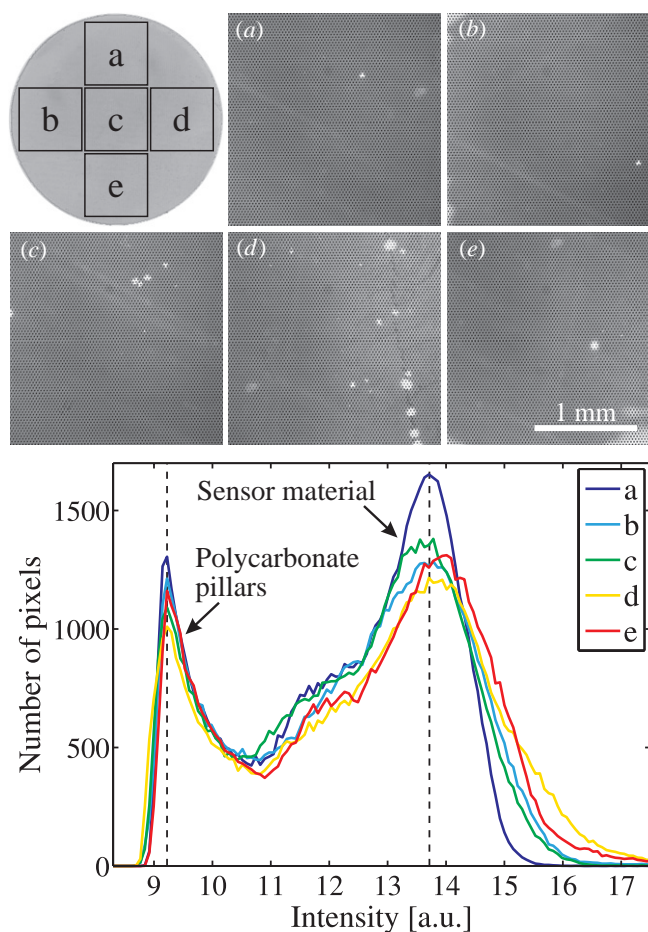


Figure 6. Top panel shows five fluorescence images (a)–(e) and the positions on the sensor spot where they were recorded. Lower panel shows intensity histograms of the five fluorescence images. Average peak centers are indicated by vertical dashed lines at intensities 9.20 au (polycarbonate pillars) and 13.70 au (sensor material).

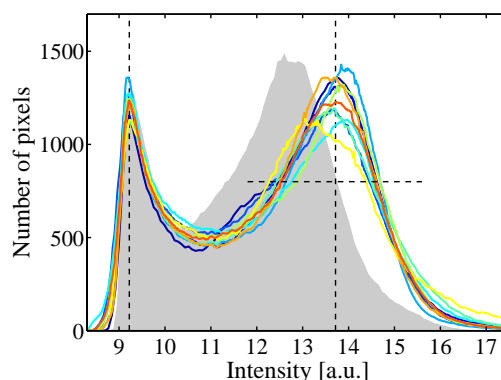


Figure 7. Average histograms of ten different sensor spots. Vertical dashed lines indicate average peak positions at intensities 9.20 au and 13.70 au. The gray shaded area shows the average histogram of a sensor spot with a 4 μm layer of sensor material, which is produced by 20% dilution of the sensor material in ethanol. Horizontal dashed line at 800 pixels marks the level at which the peak widths in figure 8 are evaluated.

All histograms in figure 6, which were taken at different locations on the same sensor spot, are centered at intensity

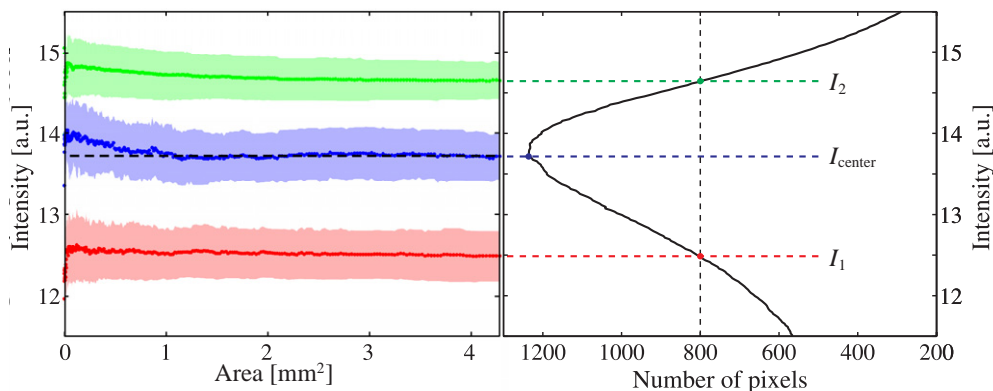


Figure 8. For fluorescence images of ten different sensor spots, histograms were produced for centered image sections of increasing area; 4×4 pixels, 6×6 pixels, 8×8 pixels, and so forth up to the full 512×512 pixels in each image. For every histogram, the peak center (blue), and the lower peak limit (red) and the upper peak limit (green) at the level of 0.3% of the pixels, corresponding to the 800 pixels level shown in the right panel, were calculated. In the left panel, the average positions of the peak center and peak limits are plotted as a function of the image section area, and the graph thus shows the evolution of the average position of the fluorescence intensity peak as larger and larger areas are evaluated. The right panel shows the average fluorescence peak based on the full images of ten different sensor spots. Dashed lines at $I_{\text{center}} = 13.70$ au, $I_1 = 12.49$ au and $I_2 = 14.64$ au show corresponding levels of the two panels. Shaded areas show the standard deviation.

13.70 ± 0.29 au. This implies that variations in the thickness distributions are equally small for all five areas within the same spot, and that the deposited material is uniformly spread over the structured surface.

Figure 7 shows average histograms of ten different sensor spots, each curve based on the average of five fluorescence images as in figure 6. The gray shaded profile shows the average histogram of a sensor spot with 80% sensor material in ethanol, producing a $4 \mu\text{m}$ layer thickness between the pillars. For comparison, it thus shows how much the intensity histogram changes when the layer thickness is reduced by $1 \mu\text{m}$. The variation between the ten different sensor spots is much smaller and shows a good spot-to-spot reproducibility.

To investigate the influence of the image size on the histograms, for fluorescence images of ten different sensor spots, histograms were produced for centered image sections of increasing size: 4×4 pixels, 6×6 pixels, 8×8 pixels, and so forth up to the full 512×512 pixels in each image. For each histogram, the peak center and the width, at the level of 0.3% of the pixels, corresponding to the 800 pixels level shown in figure 7, were calculated. Figure 8 shows the average peak center and width for the ten spots as a function of the image size. The peak position and width are seen to be constant down to image areas of 0.5 mm^2 . Below this area, the increasing trend of the peak center, but constant standard deviation, may be caused by light-source inhomogeneity increasing the excitation light intensity toward the image center. Large deviations from the average and increasing standard deviation are only seen for areas below 0.05 mm^2 , corresponding to approximately 50 unit cells of the pillar geometry. Figure 8 thus shows that, at least above 0.5 mm^2 , the same intensity histogram is obtained irrespective of the image size, and this self-similarity is another indication of good uniformity of the coating. Furthermore, it shows that the fluorescence intensity does not depend on the area, and that reproducible results can be obtained from small exposed

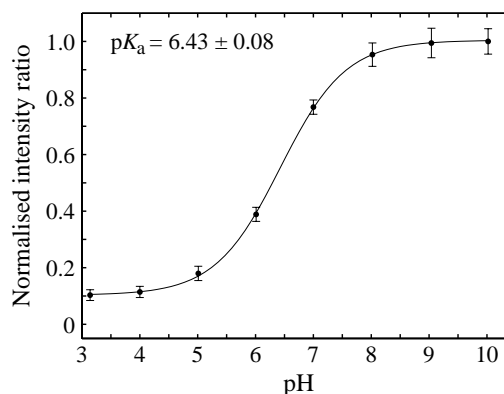


Figure 9. Calibration plot based on five different sensor spots. The normalized intensity ratio between fluorescence at 460 and 408 nm ($I_{460 \text{ nm}}/I_{408 \text{ nm}}$) is plotted as a function of pH. Error bars show the standard deviation.

areas. From a practical point of view it means that reproducible measurements of fluorescence can be obtained with a small probe, e.g., a laser, pointed randomly on the much larger sensor spot.

5. Sensor characterization

Sensor spots for pH and oxygen sensing were fabricated by depositing the two different sensor materials on a polycarbonate foil with the optimized 7 mm diameter pillar arrays of $h = 23 \mu\text{m}$, $r = 9.5 \mu\text{m}$ and $d = 30 \mu\text{m}$. The performance of the sensors was evaluated as described in [3] and [4].

Five pH sensor spots were characterized by measuring the intensity ratio between fluorescence at 460 and 408 nm wavelengths as a function of pH. The result is shown in figure 9 where a sigmoidal function has been fitted to calculate the $\text{p}K_a$ of 6.43 ± 0.08 . This value corresponds well to the $\text{p}K_a$ of

Table 1. Comparison of sensor characteristics for pH and oxygen sensors fabricated by hemiwicking (this work) and dip-coating.

	This work	Dip-coating [3, 4]
pK_a	6.43 ± 0.08	6.28 ± 0.02
$\tau_0[\mu s]$	6.061 ± 0.024	$4.91 \pm 10\%$
$K_{SV}[\text{O}_2\%]^{-1}$	0.080 ± 0.002	0.072 ± 0.002

6.28 ± 0.02 given in [3], which was made using five different films produced by dip-coating. The small error bars in figure 9 indicate good spot-to-spot reproducibility.

Equally, on the oxygen sensor spots, excited-state life times τ were measured on 38 different spots in oxygen-free atmosphere τ_0 and ambient air of 20.9% oxygen. The Stern–Volmer constant $K_{SV} = ((\tau_0/\tau) - 1)/[\text{O}_2\%]$, where $[\text{O}_2\%]$ is the concentration of O_2 in percentages, was calculated.

In table 1, the results of the sensor characterization are tabulated together with the results obtained in [3] and [4] on dip-coated films. The excited-state life time in oxygen-free atmosphere τ_0 is seen to be larger than for the dip-coated sensors, which is most likely caused by the ten-fold thicker layer of the sensor material deposited on the microstructured surface. The thicker material layer may also explain the slightly larger value of K_{SV} . However, it is worth noting that the standard deviation of τ_0 is only 0.40% compared to the much larger 10% stated in [4]. The standard deviations of K_{SV} are of equal magnitude for the two deposition methods.

6. Conclusion

In conclusion, we have shown that hemiwicking can be used to spread a liquid sol–gel sensor material on a microstructured polycarbonate surface, and that, after evaporation of the solvents, the condensed material is uniformly distributed over the structured surface. The sensing performance of sensor spots fabricated by hemiwicking was characterized and found to be in good correspondence with the performance of sensors fabricated by dip-coating of the same sensor material. We have thus demonstrated an improved method for fabricating cheap optical sensors that can be integrated in disposable lab ware.

References

- [1] McDonagh C, Burke C S and MacCraith B D 2008 Optical chemical sensors *Chem. Rev.* **108** 400–22
- [2] Naciri M, Kuystermans D and Al Rubeai M 2008 Monitoring pH and dissolved oxygen in mammalian cell culture using optical sensors *Cytotechnology* **57** 245–50
- [3] High performance optical ratiometric sol–gel-based pH sensor 2009 *Sensors Actuators B* **139** 208–13
- [4] Higgins C, Wencel D, Burke C S, MacCraith B D and McDonagh C 2008 Novel hybrid optical sensor materials for in-breath O_2 analysis *Analyst* **133** 241–7
- [5] Brinker C J, Frye G C, Hurd A J and Ashley C S 1991 Fundamentals of sol-gel dip coating *Thin Solid Films* **201** 97–108
- [6] Hwang D K, Moon J H, Shul Y G, Jung K T, Kim D H and Lee D W 2003 Scratch resistant and transparent UV-protective coating on polycarbonate *J. Sol-Gel Sci. Technol.* **26** 783–7
- [7] Huang Y-Y and Chou K-S 2003 Studies on the spin coating process of silica films *Ceram. Int.* **29** 485–93
- [8] Quéré D 2008 Wetting and roughness *Annu. Rev. Mater. Res.* **38** 71–99
- [9] Haatainen T and Ahopelto J 2003 Pattern transfer using step and stamp imprint lithography *Phys. Scr.* **67** 357
- [10] Utiko P, Persson F, Kristensen A and Larsen N B 2011 Injection molded nanofluidic chips: fabrication method and functional tests using single-molecule DNA experiments *Lab Chip* **11** 303–8
- [11] Bico J, Thiele U and Quéré D 2002 Wetting of textured surfaces *Colloids Surf.* **206** 41–6
- [12] Bico J, Tordeux C and Quéré D 2001 Rough wetting *Europhys. Lett.* **55** 214
- [13] Courbin L, Denieul E, Dressaire E, Roper M, Ajdari A and Stone H A 2007 Imbibition by polygonal spreading on microdecorated surfaces *Nature Mater.* **6** 661–4
- [14] Extrand C W, Moon S I, Hall P and Schmidt D 2007 Superwetting of structured surfaces *Langmuir* **23** 8882–90
- [15] Chang F-M, Hong S-J, Sheng Y-J and Tsao H-K 2010 Wetting invasion and retreat across a corner boundary *J. Phys. Chem. C* **114** 1615–21
- [16] Schift H 2008 Nanoimprint lithography: an old story in modern times? A review *J. Vac. Sci. Technol. B* **26** 458–80
- [17] Deegan R D, Bakajin O, Dupont T F, Huber G, Nagel S R and Witten T A 1997 Capillary flow as the cause of ring stains from dried liquid drops *Nature* **389** 827–9
- [18] Kimura S and Takami K 1988 Photoresist thickness measurement using laser-induced fluorescence *Appl. Opt.* **27** 3675–8
- [19] Pieper S B, Mestas S P, Lear K L, Zhong Z and Reardon K F 2008 Phosphorescence characteristics of ruthenium complex as an optical transducer for biosensors *Appl. Phys. Lett.* **92** 081915

Bibliography

- [1] D. Psaltis, S. R. Quake and C. Yang, Developing optofluidic technology through the fusion of microfluidics and optics, *Nature*, 2006, **442**, 381–386, DOI: 10.1038/nature05060.
- [2] C. Monat, P. Domachuk and B. J. Eggleton, Integrated optofluidics: A new river of light, *Nature Photonics*, 2007, **1**, 106–114, DOI: 10.1038/nphoton.2006.96.
- [3] C. Monat, P. Domachuk, C. Grillet, M. Collins, B. Eggleton, M. Cronin-Golomb, S. Mutzenich, T. Mahmud, G. Rosengarten and A. Mitchell, Optofluidics: a novel generation of reconfigurable and adaptive compact architectures, *Microfluidics and Nanofluidics*, 2008, **4**, 81–95, DOI: 10.1007/s10404-007-0222-z.
- [4] Y. Fainman, L. Lee, D. Psaltis and C. Yang, *Optofluidics: Fundamentals, Devices, and Applications*, McGraw-Hill, 2009.
- [5] U. Levy and R. Shamaï, Tunable optofluidic devices, *Microfluidics and Nanofluidics*, 2008, **4**, 97–105, DOI: 10.1007/s10404-007-0216-x.
- [6] G. M. Whitesides, The origins and the future of microfluidics, *Nature*, 2006, **442**, 368–373, DOI: 10.1038/nature05058.
- [7] J. O. Tegenfeldt, C. Prinz, H. Cao, S. Chou, W. W. Reisner, R. Riehn, Y. M. Wang, E. C. Cox, J. C. Sturm, P. Silberzan and R. H. Austin, The dynamics of genomic-length DNA molecules in 100-nm channels, *Proceedings of the National Academy of Sciences of the United States of America*, 2004, **101**, 10979–10983, DOI: 10.1073/pnas.0403849101.
- [8] S. Mandal and D. Erickson, Nanoscale optofluidic sensor arrays, *Optics Express*, 2008, **16**, 1623–1631, DOI: 10.1364/OE.16.001623.
- [9] S. Balslev, A. M. Jørgensen, B. Bilenberg, K. B. Mogensen, D. Snakenborg, O. Geschke, J. P. Kutter and A. Kristensen, Lab-on-a-chip with integrated optical transducers, *Lab Chip*, 2006, **6**, 213–217, DOI: 10.1039/B512546D.
- [10] Y. Lv, Z. Zhang and F. Chen, Chemiluminescence biosensor chip based on a microreactor using carrier air flow for determination of uric acid in human serum, *Analyst*, 2002, **127**, 1176–1179, DOI: 10.1039/B203501B.

- [11] O. J. A. Schueller, D. C. Duffy, J. A. Rogers, S. T. Brittain and G. M. Whitesides, Reconfigurable diffraction gratings based on elastomeric microfluidic devices, *Sensors and Actuators A: Physical*, 1999, **78**, 149–159, DOI: 10.1016/S0924-4247(98)00242-8.
- [12] C. M. Lampert, Large-area smart glass and integrated photovoltaics, *Solar Energy Materials and Solar Cells*, 2003, **76**, 489–499, DOI: 10.1016/S0927-0248(02)00259-3.
- [13] X. Wang, D. Wilson, R. Muller, P. Maker and D. Psaltis, Liquid-Crystal Blazed-Grating Beam Deflector, *Applied Optics*, 2000, **39**, 6545–6555, DOI: 10.1364/AO.39.006545.
- [14] F. Persson and J. O. Tegenfeldt, DNA in nanochannels—directly visualizing genomic information, *Chemical Society Reviews*, 2010, **39**, 985–999, DOI: 10.1039/B912918A.
- [15] M. B. Christiansen, A. Kristensen, S. Xiao and N. A. Mortensen, Photonic integration in k-space: Enhancing the performance of photonic crystal dye lasers, *Applied Physics Letters*, 2008, **93**, 231101, DOI: 10.1063/1.3040686.
- [16] A. Gombert, W. Glaubitt, K. Rose, J. Dreibholz, B. Bläsi, A. Heinzl, D. Sporn, W. Döll and V. Wittwer, Subwavelength-structured antireflective surfaces on glass, *Thin Solid Films*, 1999, **351**, 73–78, DOI: 10.1016/S0040-6090(98)01780-5.
- [17] H. Ghiradella, Light and color on the wing: structural colors in butterflies and moths, *Applied Optics*, 1991, **30**, 3492–3500, DOI: 10.1364/AO.30.003492.
- [18] J. P. Youngblood and N. R. Sottos, Bioinspired Materials for Self-Cleaning and Self-Healing, *MRS Bulletin*, 2008, **33**, 732–741, DOI: 10.1557/mrs2008.158.
- [19] A. Solga, Z. Cerman, B. F. Striffler, M. Spaeth and W. Barthlott, The dream of staying clean: Lotus and biomimetic surfaces, *Bioinspiration & Biomimetics*, 2007, **2**, S126, DOI: 10.1088/1748-3182/2/4/S02.
- [20] R. Blossey, Self-cleaning surfaces - virtual realities, *Nature Materials*, 2003, **2**, 301–306, DOI: 10.1038/nmat856.
- [21] D. Mijatovic, J. C. T. Eijkel and A. van den Berg, Technologies for nanofluidic systems: top-down vs. bottom-up – a review, *Lab on a Chip*, 2005, **5**, 492–500, DOI: 10.1039/B416951D.
- [22] R. Reisfeld and T. Saraidarov, Innovative materials based on sol-gel technology, *Optical Materials*, 2006, **28**, 64–70, DOI: 10.1016/j.optmat.2004.11.055.
- [23] L. C. Klein, Sol-Gel Optical Materials, *Annual Review of Materials Science*, 1993, **23**, 437–452, DOI: 10.1146/annurev.ms.23.080193.0022533.
- [24] P. Lalanne and M. Hutley, in *Artificial Media Optical Properties—Subwavelength Scale*, ch. 5, pp. 62–71, DOI: 10.1081/E-EOE-120009537.

- [25] F. Guillemot, A. Brunet-Bruneau, E. Bourgeat-Lami, T. Gacoin, E. Barthel and J.-P. Boilot, Latex-templated silica films: Tailoring porosity to get a stable low-refractive index, *Chemistry of Materials*, 2010, **22**, 2822–2828, DOI: 10.1021/cm903754k.
- [26] S. Y. Chou, P. R. Krauss and P. J. Renstrom, Nanoimprint lithography, *Journal of Vacuum Science & Technology B*, 1996, **14**, 4129–4133, DOI: 10.1116/1.588605.
- [27] H. Schiff and A. Kristensen, in *Handbook of nanotechnology*, ed. B. Bhushan, Springer Verlag, Berlin, Germany, 3rd edn., 2010, ch. 9.
- [28] J. D. Plummer, M. D. Deal and P. B. Griffin, *Silicon VLSI technology: fundamentals, practice and modeling*, Prentice Hall, 2000.
- [29] A. Broers, A. Hoole and J. Ryan, Electron beam lithography - Resolution limits, *Microelectronic Engineering*, 1996, **32**, 131–142, DOI: 10.1016/0167-9317(95)00368-1.
- [30] M. D. Austin, W. Zhang, H. Ge, D. Wasserman, S. A. Lyon and S. Y. Chou, 6 nm half-pitch lines and $0.04 \mu\text{m}^2$ static random access memory patterns by nanoimprint lithography, *Nanotechnology*, 2005, **16**, 1058, DOI: 10.1088/0957-4484/16/8/010.
- [31] B. Wu, Next-generation lithography for 22 and 16 nm technology nodes and beyond, *Science China: Information Sciences*, 2011, **54**, 959–979, DOI: 10.1007/s11432-011-4227-6.
- [32] R. B. Bird, R. C. Armstrong and O. Hassager, *Dynamics of Polymeric Liquids: Fluid mechanics*, John Wiley and Sons, 2nd edn., 1987, vol. 1.
- [33] H. Bruus, *Theoretical microfluidics*, Oxford University Press, 2008.
- [34] *Alternative Lithography: Unleashing the Potentials of Nanotechnology*, ed. C. M. Sotomayor Torres, Kluwer Academic Publishers, 2003.
- [35] M. B. Christiansen, M. Schøler, S. Balslev, R. B. Nielsen, D. H. Petersen and A. Kristensen, Wafer-scale fabrication of polymer distributed feedback lasers, *Journal of Vacuum Science & Technology B*, 2006, **24**, 3252–3257, DOI: 10.1116/1.2387154.
- [36] G. Luo, I. Maximov, D. Adolph, M. Graczyk, P. Carlberg, S. Ghatnekar-Nilsson, D. Hessman, T. Zhu, Z. Liu, H. Q. Xu and L. Montelius, Nanoimprint lithography for the fabrication of interdigitated cantilever arrays, *Nanotechnology*, 2006, **17**, 1906, DOI: 10.1088/0957-4484/17/8/017.
- [37] S. Merino, A. Retolaza, A. Juarros and H. Schiff, The influence of stamp deformation on residual layer homogeneity in thermal nanoimprint lithography, *Microelectronic Engineering*, 2008, **85**, 1892–1896, DOI: 10.1016/j.mee.2008.06.011.

- [38] H. Schiff, L. J. Heyderman, M. Auf der Maur and J. Gobrecht, Pattern formation in hot embossing of thin polymer films, *Nanotechnology*, 2001, **12**, 173, DOI: 10.1088/0957-4484/12/2/321.
- [39] H.-C. Scheer, N. Bogdanski, M. Wissen, T. Konishi and Y. Hirai, Profile evolution during thermal nanoimprint, *Microelectronic Engineering*, 2006, **83**, 843–846, DOI: 10.1016/j.mee.2006.01.255.
- [40] H. Schiff, S. Bellini, M. B. Mikkelsen and J. Gobrecht, Visualization of mold filling stages in thermal nanoimprint by using pressure gradients, *Journal of Vacuum Science & Technology B*, 2007, **25**, 2312–2316, DOI: 10.1116/1.2806972.
- [41] H. Schiff, G. Kim, J. Lee and J. Gobrecht, 3D visualization of mold filling stages in thermal nanoimprint by white light interferometry and atomic force microscopy, *Nanotechnology*, 2009, **20**, 355301, DOI: 10.1088/0957-4484/20/35/355301.
- [42] H. Schmitt, L. Frey, H. Ryssel, M. Rommel and C. Lehrer, UV nanoimprint materials: Surface energies, residual layers, and imprint quality, *Journal of Vacuum Science & Technology B*, 2007, **25**, 785–790, DOI: 10.1116/1.2732742.
- [43] D. M. Taylor, T. J. Lewis and T. P. T. Williams, The electrokinetic charging of polymers during capillary extrusion, *Journal of Physics D: Applied Physics*, 1974, **7**, 1756, DOI: 10.1088/0022-3727/7/12/320.
- [44] H. Schulz, M. Wissen, N. Bogdanski, H.-C. Scheer, K. Mattes and C. Friedrich, Impact of molecular weight of polymers and shear rate effects for nanoimprint lithography, *Microelectronic Engineering*, 2006, **83**, 259–280, DOI: 10.1016/j.mee.2005.07.090.
- [45] H. Schiff, S. Bellini, J. Gobrecht, F. Reuther, M. Kubenz, M. B. Mikkelsen and K. Vogelsang, Fast heating and cooling in nanoimprint using a spring-loaded adapter in a preheated press, *Microelectronic Engineering*, 2007, **84**, 932–936, DOI: 10.1016/j.mee.2007.01.061.
- [46] M. Worgull, *Hot Embossing: Theory and Technology of Microreplication*, William Andrew, 2009.
- [47] T. Haatainen and J. Ahopelto, Pattern Transfer using Step&Stamp Imprint Lithography, *Physica Scripta*, 2003, **67**, 357, DOI: 10.1238/Physica.Regular.067a00357.
- [48] T. Mäkelä, T. Haatainen, P. Majander, J. Ahopelto and V. Lambertini, Continuous Double-Sided Roll-to-Roll Imprinting of Polymer Film, *Japanese Journal of Applied Physics*, 2008, **47**, 5142–5144, DOI: 10.1143/JJAP.47.5142.
- [49] L. J. Guo, Nanoimprint Lithography: Methods and Material Requirements, *Advanced Materials*, 2007, **19**, 495–513, DOI: 10.1002/adma.200600882.

- [50] S. H. Ahn and L. J. Guo, Large-Area Roll-to-Roll and Roll-to-Plate Nanoimprint Lithography: A Step toward High-Throughput Application of Continuous Nanoimprinting, *ACS Nano*, 2009, **3**, 2304–2310, DOI: 10.1021/nm9003633.
- [51] M. Colburn, S. C. Johnson, M. D. Stewart, S. Damle, T. C. Bailey, B. Choi, M. Wedlake, T. B. Michaelson, S. V. Sreenivasan, J. G. Ekerdt and C. G. Willson, Step and flash imprint lithography: a new approach to high-resolution patterning, *Proceedings of SPIE 3676*, 1999, 379, DOI: 10.1117/12.351155.
- [52] Y. Cho, S. Kwon, J.-W. Seo, J.-G. Kim, J.-W. Cho, J.-W. Park, H. Kim and S. Lee, Development of large area nano imprint technology by step and repeat process and pattern stitching technique, *Microelectronic Engineering*, 2009, **86**, 2417–2422, DOI: 10.1016/j.mee.2009.05.004.
- [53] T. Haatainen, P. Majander, T. Mäkelä, J. Ahopelto and Y. Kawaguchi, Imprinted 50 nm Features Fabricated by Step and Stamp UV Imprinting, *Japanese Journal of Applied Physics*, 2008, **47**, 5164–5166, DOI: 10.1143/JJAP.47.5164.
- [54] ITRS International Technology Roadmap for Semiconductors. <http://public.itrs.net>.
- [55] D. Forchheimer, G. Luo, L. Montelius and L. Ye, Molecularly imprinted nanostructures by nanoimprint lithography, *Analyst*, 2010, **135**, 1219–1223, DOI: 10.1039/C0AN00132E.
- [56] R. J. McMurray, N. Gadegaard, P. M. Tsimbouri, K. V. Burgess, L. E. McNamara, R. Tare, K. Murawski, E. Kingham, R. O. C. Oreffo and M. J. Dalby, Nanoscale surfaces for the long-term maintenance of mesenchymal stem cell phenotype and multipotency, *Nature Materials*, 2011, **10**, 637–644, DOI: 10.1038/nmat3058.
- [57] M. Takahashi, Y. Murakoshi, R. Maeda and K. Hasegawa, Large area micro hot embossing of Pyrex glass with GC mold machined by dicing, *Microsystem Technologies*, 2007, **13**, 379–384, DOI: 10.1007/s00542-006-0186-z.
- [58] C. Peroz, C. Heitz, E. Barthel, E. Søndergård and V. Goletto, Glass nanostructures fabricated by soft thermal nanoimprint, *Journal of Vacuum Science & Technology B*, 2007, **25**, L27–L30, DOI: 10.1116/1.2748791.
- [59] L. H. Thamdrup, A. Klukowska and A. Kristensen, Stretching DNA in polymer nanochannels fabricated by thermal imprint in PMMA, *Nanotechnology*, 2008, **19**, 125301, DOI: 10.1088/0957-4484/19/12/125301.
- [60] C. J. Brinker and G. W. Scherer, *Sol-Gel Science: The Physics and Chemistry of Sol-Gel Processing*, Academic Press, San Diego, CA, 1990.
- [61] S. Henning and L. Svensson, Production of Silica Aerogel, *Physica Scripta*, 1981, **23**, 697, DOI: 10.1088/0031-8949/23/4B/018.
- [62] L. W. Hrubesh, Aerogel applications, *Journal of Non-Crystalline Solids*, 1998, **225**, 335–342, DOI: 10.1016/S0022-3093(98)00135-5.

- [63] C. McDonagh, C. S. Burke and B. D. MacCraith, Optical Chemical Sensors, *Chemical Reviews*, 2008, **108**, 400–422, DOI: 10.1021/cr068102g.
- [64] J. Zhang, X. Wang, L. He, L. Chen, C.-Y. Su and S. L. James, Metal-organic gels as functionalisable supports for catalysis, *New Journal of Chemistry*, 2009, **33**, 1070–1075, DOI: 10.1039/B822104A.
- [65] S. V. Nitta, V. Pisupatti, A. Jain, P. C. Wayner, W. N. Gill and J. L. Plawsky, Surface modified spin-on xerogel films as interlayer dielectrics, *Journal of Vacuum Science & Technology B*, 1999, **17**, 205–212, DOI: 10.1116/1.590541.
- [66] A. Agrios and P. Pichat, State of the art and perspectives on materials and applications of photocatalysis over TiO₂, *Journal of Applied Electrochemistry*, 2005, **35**, 655–663, DOI: 10.1007/s10800-005-1627-6.
- [67] S. Hofacker, M. Mechtel, M. Mager and H. Kraus, Sol-gel: a new tool for coatings chemistry, *Progress in Organic Coatings*, 2002, **45**, 159–164, DOI: 10.1016/S0300-9440(02)00045-0.
- [68] D. Hwang, J. Moon, Y. Shul, K. Jung, D. Kim and D. Lee, Scratch Resistant and Transparent UV-Protective Coating on Polycarbonate, *Journal of Sol-Gel Science and Technology*, 2003, **26**, 783–787, DOI: 10.1023/A:1020774927773.
- [69] Y.-Y. Huang and K.-S. Chou, Studies on the spin coating process of silica films, *Ceramics International*, 2003, **29**, 485–493, DOI: 10.1016/S0272-8842(02)00191-8.
- [70] C. Brinker, G. Frye, A. Hurd and C. Ashley, Fundamentals of sol-gel dip coating, *Thin Solid Films*, 1991, **201**, 97–108, DOI: 10.1016/0040-6090(91)90158-T.
- [71] T. Kreuzberger, A. Harnisch, M. Helgert, L. Erdmann and R. Brunner, Sol-gel process to cast quartz glass microlens arrays, *Microelectronic Engineering*, 2009, **86**, 1173–1175, DOI: 10.1016/j.mee.2009.01.071.
- [72] M. Li, H. Tan, L. Chen, J. Wang and S. Y. Chou, Large area direct nanoimprinting of SiO₂-TiO₂ gel gratings for optical applications, *Journal of Vacuum Science & Technology B*, 2003, **21**, 660–663, DOI: 10.1116/1.1545736.
- [73] C. Peroz, S. Dhuey, B. Harteneck and S. Cabrini, Proceedings of the 53rd EIPBN Conference, 2009.
- [74] M. Verschuuren and H. van Sprang, 3D Photonic Structures by Sol-Gel Imprint Lithography, *Materials Research Society Symposia Proceedings*, 2007, **1002**, N03–N05, DOI: 10.1557/PROC-1002-N03-05.
- [75] F. Devreux, J. P. Boilot, F. Chaput and A. Lecomte, Sol-gel condensation of rapidly hydrolyzed silicon alkoxides: A joint ²⁹Si NMR and small-angle x-ray scattering study, *Phys. Rev. A*, 1990, **41**, 6901–6909, DOI: 10.1103/PhysRevA.41.6901.

- [76] P. Innocenzi, M. O. Abdirashid and M. Guglielmi, Structure and properties of sol-gel coatings from methyltriethoxysilane and tetraethoxysilane, *Journal of Sol-Gel Science and Technology*, 1994, **3**, 47–55, DOI: 10.1007/BF00490148.
- [77] K. Yoon, K.-Y. Yang, H. Lee and H.-S. Kim, Formation of TiO₂ nanopattern using reverse imprinting and sol-gel method, *Journal of Vacuum Science & Technology B*, 2009, **27**, 2810–2813, DOI: 10.1116/1.3246394.
- [78] S.-S. Kim, S.-Y. Choi, C.-G. Park and H.-W. Jin, Transparent conductive ITO thin films through the sol-gel process using metal salts, *Thin Solid Films*, 1999, **347**, 155–160, DOI: 10.1016/S0040-6090(98)01748-9.
- [79] A. Mehner, J. Dong, T. Prenzel, W. Datchary and D. Lucca, Mechanical and chemical properties of thick hybrid sol-gel silica coatings from acid and base catalyzed sols, *Journal of Sol-Gel Science and Technology*, 2010, **54**, 355–362, DOI: 10.1007/s10971-010-2203-z.
- [80] A. A. Letailleur, F. Ribot, C. Boissière, J. Teisseire, E. Barthel, B. Desmazières, N. Chemin and C. Sanchez, Sol-Gel Derived Hybrid Thin Films: The Chemistry behind Processing, *Chemistry of Materials*, 2011, DOI: 10.1021/cm202755g.
- [81] A. Alvarez-Herrero, G. Ramos, F. del Monte, E. Bernabeu and D. Levy, Water adsorption in porous TiO₂-SiO₂ sol-gel films analyzed by spectroscopic ellipsometry, *Thin Solid Films*, 2004, **455–456**, 356–360, DOI: 10.1016/j.tsf.2004.01.023.
- [82] B. C. Yadav, N. K. Pandey, A. K. Srivastava and P. Sharma, Optical humidity sensors based on titania films fabricated by sol-gel and thermal evaporation methods, *Measurement Science and Technology*, 2007, **18**, 260, DOI: 10.1088/0957-0233/18/1/032.
- [83] B. Bhola, P. Nosovitskiy, H. Mahalingam and W. Steier, Sol-Gel-Based Integrated Optical Microring Resonator Humidity Sensor, *IEEE Sensors Journal*, 2009, **9**, 740–747, DOI: 10.1109/JSEN.2009.2020113.
- [84] T. Leveder, S. Landis, N. Chaix and L. Davoust, Thin polymer films viscosity measurements from nanopatterning method, *Journal of Vacuum Science & Technology B*, 2010, **28**, 1251–1258, DOI: 10.1116/1.3504591.
- [85] S. Kasolang and R. S. Dwyer-Joyce, Viscosity measurement in thin lubricant films using shear ultrasonic reflection, *Journal of Engineering Tribology*, 2008, **222**, 423–429, DOI: 10.1243/13506501JET382.
- [86] A. Letailleur, J. Teisseire, N. Chemin, E. Barthel and E. Søndergård, Chemorheology of Sol-Gel Silica for the Patterning of High Aspect Ratio Structures by Nanoimprint, *Chemistry of Materials*, 2010, **22**, 3143–3151, DOI: 10.1021/cm100285b.
- [87] D. E. Streng, S. F. Lim, J. Pan, A. Karpusenka and R. Riehn, Stretching chromatin through confinement, *Lab on a Chip*, 2009, **9**, 2772–2774, DOI: 10.1039/b909217j.

- [88] R. Riehn, M. Lu, Y.-M. Wang, S. F. Lim, E. C. Cox and R. H. Austin, Restriction mapping in nanofluidic devices, *Proceedings of the National Academy of Sciences of the United States of America*, 2005, **102**, 10012–10016, DOI: 10.1073/pnas.0503809102.
- [89] Y. M. Wang, J. O. Tegenfeldt, W. Reisner, R. Riehn, X.-J. Guan, L. Guo, I. Golding, E. C. Cox, J. Sturm and R. H. Austin, Single-molecule studies of repressor-DNA interactions show long-range interactions, *Proceedings of the National Academy of Sciences of the United States of America*, 2005, **102**, 9796–9801, DOI: 10.1073/pnas.0502917102.
- [90] W. Reisner, N. B. Larsen, A. Silahatoglu, A. Kristensen, N. Tommerup, J. O. Tegenfeldt and H. Flyvbjerg, Single-molecule denaturation mapping of DNA in nanofluidic channels, *Proceedings of the National Academy of Sciences*, 2010, **107**, 13294–13299, DOI: 10.1073/pnas.1007081107.
- [91] M. B. Mikkelsen, W. Reisner, H. Flyvbjerg and A. Kristensen, Pressure-Driven DNA in Nanogroove Arrays: Complex Dynamics Leads to Length- and Topology-Dependent Separation, *Nano Letters*, 2011, **11**, 1598–1602, DOI: 10.1021/nl1044764.
- [92] J. Han and H. G. Craighead, Separation of Long DNA Molecules in a Microfabricated Entropic Trap Array, *Science*, 2000, **288**, 1026–1029, DOI: 10.1126/science.288.5468.1026.
- [93] J. Fu, R. B. Schoch, A. L. Stevens, S. R. Tannenbaum and J. Han, A patterned anisotropic nanofluidic sieving structure for continuous-flow separation of DNA and proteins, *Nature Nanotechnology*, 2007, **2**, 121–128, DOI: 10.1038/nnano.2006.206.
- [94] P. Utko, F. Persson, A. Kristensen and N. B. Larsen, Injection molded nanofluidic chips: Fabrication method and functional tests using single-molecule DNA experiments, *Lab on a Chip*, 2011, **11**, 303–308, DOI: 10.1039/c0lc00260g.
- [95] Y. Kim, K. S. Kim, K. L. Kounovsky, R. Chang, G. Y. Jung, J. J. dePablo, K. Jo and D. C. Schwartz, Nanochannel confinement: DNA stretch approaching full contour length, *Lab on a Chip*, 2011, **11**, 1721–1729, DOI: 10.1039/C0LC00680G.
- [96] R. Chantiwas, S. Park, S. A. Soper, B. C. Kim, S. Takayama, V. Sunkara, H. Hwang and Y.-K. Cho, Flexible fabrication and applications of polymer nanochannels and nanoslits, *Chemical Society Reviews*, 2011, **40**, 3677–3702, DOI: 10.1039/C0CS00138D.
- [97] S. Park, Y. S. Huh, H. G. Craighead and D. Erickson, A method for nanofluidic device prototyping using elastomeric collapse, *Proceedings of the National Academy of Sciences*, 2009, **106**, 15549–15554, DOI: 10.1073/pnas.0904004106.
- [98] A. R. Abate, D. Lee, T. Do, C. Holtze and D. A. Weitz, Glass coating for PDMS microfluidic channels by sol-gel methods, *Lab on a Chip*, 2008, **8**, 516–518, DOI: 10.1039/B800001H.

- [99] X. Wang, J. Jin, X. Li, X. Li, Y. Ou, Q. Tang, S. Fu and F. Gao, Low-pressure thermal bonding, *Microelectronic Engineering*, 2011, **88**, 2427–2430, DOI: 10.1016/j.mee.2011.01.022.
- [100] W. Reisner, K. J. Morton, R. Riehn, Y. M. Wang, Z. Yu, M. Rosen, J. C. Sturm, S. Y. Chou, E. Frey and R. H. Austin, Statics and Dynamics of Single DNA Molecules Confined in Nanochannels, *Phys. Rev. Lett.*, 2005, **94**, 196101, DOI: 10.1103/PhysRevLett.94.196101.
- [101] F. Persson, P. Utko, W. Reisner, N. B. Larsen and A. Kristensen, Confinement Spectroscopy: Probing Single DNA Molecules with Tapered Nanochannels, *Nano Letters*, 2009, **9**, 1382–1385, DOI: 10.1021/nl803030e.
- [102] W. Li, J. O. Tegenfeldt, L. Chen, R. H. Austin, S. Y. Chou, P. A. Kohl, J. Krotine and J. C. Sturm, Sacrificial polymers for nanofluidic channels in biological applications, *Nanotechnology*, 2003, **14**, 578, DOI: 10.1088/0957-4484/14/6/302.
- [103] H. Cao, Z. Yu, J. Wang, J. O. Tegenfeldt, R. H. Austin, E. Chen, W. Wu and S. Y. Chou, Fabrication of 10 nm enclosed nanofluidic channels, *Applied Physics Letters*, 2002, **81**, 174–176, DOI: 10.1063/1.1489102.
- [104] K. R. Hawkins and P. Yager, Nonlinear decrease of background fluorescence in polymer thin-films - a survey of materials and how they can complicate fluorescence detection in μ TAS, *Lab on a Chip*, 2003, **3**, 248–252, DOI: 10.1039/B307772C.
- [105] A. Piruska, I. Nikcevic, S. H. Lee, C. Ahn, W. R. Heineman, P. A. Limbach and C. J. Seliskar, The autofluorescence of plastic materials and chips measured under laser irradiation, *Lab on a Chip*, 2005, **5**, 1348–1354, DOI: 10.1039/B508288A.
- [106] F. Persson, L. H. Thamdrup, M. B. L. Mikkelsen, S. E. Jarlgaard, P. Skafte-Pedersen, H. Bruus and A. Kristensen, Double thermal oxidation scheme for the fabrication of SiO₂ nanochannels, *Nanotechnology*, 2007, **18**, 245301, DOI: 10.1088/0957-4484/18/24/245301.
- [107] R. Marie, J. P. Beech, J. Vörös, J. O. Tegenfeldt and F. Höök, Use of PLL-g-PEG in Micro-Fluidic Devices for Localizing Selective and Specific Protein Binding, *Langmuir*, 2006, **22**, 10103–10108, DOI: 10.1021/la060198m.
- [108] C. Peroz, V. Chauveau, E. Barthel and E. Søndergård, Nanoimprint Lithography on Silica Sol-Gels: A Simple Route to Sequential Patterning, *Advanced Materials*, 2009, **21**, 555–558, DOI: 10.1002/adma.200702484.
- [109] A. Plößl and G. Kräuter, Wafer direct bonding: tailoring adhesion between brittle materials, *Materials Science and Engineering: R: Reports*, 1999, **25**, 1–88, DOI: 10.1016/S0927-796X(98)00017-5.
- [110] A. V. Larsen, L. Poulsen, H. Birgens, M. Dufva and A. Kristensen, Pinched flow fractionation devices for detection of single nucleotide polymorphisms, *Lab Chip*, 2008, **8**, 818–821, DOI: 10.1039/B802268B.

- [111] R. Dhumpa, K. J. Handberg, P. H. Jørgensen, S. Yi, A. Wolff and D. D. Bang, Rapid detection of avian influenza virus in chicken fecal samples by immunomagnetic capture reverse transcriptase–polymerase chain reaction assay, *Diagnostic Microbiology and Infectious Disease*, 2011, **69**, 258–265, DOI: 10.1016/j.diagmicrobio.2010.09.022.
- [112] C. M. Dobson, Protein folding and misfolding, *Nature*, 2003, **426**, 884–890, DOI: 10.1038/nature02261.
- [113] F. Sanger, S. Nicklen and A. R. Coulson, DNA Sequencing with Chain-Terminating Inhibitors, *Proceedings of the National Academy of Sciences of the United States of America*, **74**, 5463–5467, DOI: 10.1073/pnas.74.12.5463.
- [114] C. Aaij and P. Borst, The gel electrophoresis of DNA, *Biochimica et Biophysica Acta*, 1972, **269**, 192–200, DOI: 10.1016/0005-2787(72)90426-1.
- [115] R. K. Saiki, D. H. Gelfand, S. Stoffel, S. J. Scharf, R. Higuchi, G. T. Horn, K. B. Mullis and H. A. Erlich, Primer-directed enzymatic amplification of DNA with a thermostable DNA polymerase, *Science*, 1988, **239**, 487–491, DOI: 10.1126/science.2448875.
- [116] J. Kieleczawa, *DNA sequencing: optimizing the process and analysis*, Jones and Bartlett Publishers, 1st edn., 2005.
- [117] R. G. Blazej, P. Kumaresan and R. A. Mathies, Microfabricated bioprocessor for integrated nanoliter-scale Sanger DNA sequencing, *Proceedings of the National Academy of Sciences*, 2006, **103**, 7240–7245, DOI: 10.1073/pnas.0602476103.
- [118] J. Han, S. Turner and H. Craighead, Entropic trapping and escape of long DNA molecules at submicron size constriction, *Physical Review Letters*, 1999, **83**, 1688–1691, DOI: 10.1103/PhysRevLett.83.1688.
- [119] J. Han and H. G. Craighead, Characterization and optimization of an entropic trap for DNA separation, *Analytical Chemistry*, 2002, **74**, 394–401, DOI: 10.1021/ac0107002.
- [120] K. Jo, D. M. Dhingra, T. Odijk, J. J. de Pablo, M. D. Graham, R. Runnheim, D. Forrest and D. C. Schwartz, A single-molecule barcoding system using nanoslits for DNA analysis, *Proceedings of the National Academy of Sciences of the United States of America*, 2007, **104**, 2673–2678, DOI: 10.1073/pnas.0611151104.
- [121] A. Meller, L. Nivon, E. Brandin, J. Golovchenko and D. Branton, Rapid nanopore discrimination between single polynucleotide molecules, *Proceedings of the National Academy of Sciences*, 2000, **97**, 1079–1084, DOI: 10.1073/pnas.97.3.1079.
- [122] J. Li, M. Gershow, D. Stein, E. Brandin and J. A. Golovchenko, DNA molecules and configurations in a solid-state nanopore microscope, *Nature Materials*, 2003, **2**, 611–615, DOI: 10.1038/nmat965.

- [123] D. Branton, D. W. Deamer, A. Marziali, H. Bayley, S. A. Benner, T. Butler, M. Di Ventra, S. Garaj, A. Hibbs, X. Huang, S. B. Jovanovich, P. S. Krstic, X. S. Lindsay, Stuart Ling, C. H. Mastrangelo, A. Meller, J. S. Oliver, Y. V. Pershin, J. M. Ramsey, R. Riehn, G. V. Soni, V. Tabard-Cossa, M. Wanunu, M. Wiggin and J. A. Schloss, The potential and challenges of nanopore sequencing, *Nature Biotechnology*, 2008, **26**, 1146–1153, DOI: 10.1038/nbt.1495.
- [124] W. W. Reisner, *PhD thesis*, Department of Physics, Princeton University, 2006.
- [125] M. Rubinstein and R. H. Colby, *Polymer Physics*, Oxford University Press, 2003.
- [126] W. Reisner, J. P. Beech, N. B. Larsen, H. Flyvbjerg, A. Kristensen and J. O. Tegenfeldt, Nanoconfinement-Enhanced Conformational Response of Single DNA Molecules to Changes in Ionic Environment, *Phys. Rev. Lett.*, 2007, **99**, 058302, DOI: 10.1103/PhysRevLett.99.058302.
- [127] D. W. Schaefer, J. F. Joanny and P. Pincus, Dynamics of semiflexible polymers in solution, *Macromolecules*, 1980, **13**, 1280–1289, DOI: 10.1021/ma60077a048.
- [128] P.-G. de Gennes, *Scaling concepts in polymer physics*, Cornell University Press, Ithaca, NY, 1979.
- [129] T. Odijk, The statistics and dynamics of confined or entangled stiff polymers, *Macromolecules*, 1983, **16**, 1340–1344, DOI: 10.1021/ma00242a015.
- [130] F. Persson, *PhD thesis*, DTU Nanotech, Technical University of Denmark, 2009.
- [131] J. W. Lichtman and J.-A. Conchello, Fluorescence microscopy, *Nature Methods*, 2005, **2**, 910–919, DOI: 10.1038/nmeth817.
- [132] T. Sakaue, DNA electrophoresis in designed channels, *The European Physical Journal. E, Soft Matter*, 2006, **19**, 477–487, DOI: 10.1140/epje/i2005-10075-9.
- [133] J. Han and H. G. Craighead, Entropic trapping and sieving of long DNA molecules in a nanofluidic channel, *Journal of Vacuum Science & Technology A*, 1999, **17**, 2142–2147, DOI: 10.1116/1.581740.
- [134] M. L. Jepsen and H. J. Gerritsen, Liquid-crystal-filled gratings with high diffraction efficiency, *Optics Letters*, 1996, **21**, 1081–1083, DOI: 10.1364/OL.21.001081.
- [135] R. Rajasekharan, C. Bay, Q. Dai, J. Freeman and T. D. Wilkinson, Electrically reconfigurable nanophotonic hybrid grating lens array, *Applied Physics Letters*, 2010, **96**, 233108, DOI: 10.1063/1.3449130.
- [136] B. Maune, M. Loncar, J. Witzens, M. Hochberg, T. Baehr-Jones, D. Psaltis, A. Scherer and Y. Qiu, Liquid-crystal electric tuning of a photonic crystal laser, *Applied Physics Letters*, 2004, **85**, 360–362, DOI: 10.1063/1.1772869.

- [137] J. Q. Yu, Y. Yang, A. Q. Liu, L. K. Chin and X. M. Zhang, Microfluidic droplet grating for reconfigurable optical diffraction, *Optics Letters*, 2010, **35**, 1890–1892, DOI: 10.1364/OL.35.001890.
- [138] B. V. Huff and G. L. McIntire, Determination of the electrophoretic mobility of polystyrene particles by capillary electrophoresis, *Journal of Microcolumn Separations*, 1994, **6**, 591–594, DOI: 10.1002/mcs.1220060610.
- [139] H. K. Jones and N. E. Ballou, Separations of chemically different particles by capillary electrophoresis, *Analytical Chemistry*, 1990, **62**, 2484–2490, DOI: 10.1021/ac00221a014.
- [140] A. Gombert, *Diffraction Optics and Micro-Optics*, 2004, p. DTuD3.
- [141] H. J. Gerritsen and M. L. Jepsen, Rectangular Surface-Relief Transmission Gratings With a Very Large First-Order Diffraction Efficiency (95%) for Unpolarized Light, *Appl. Opt.*, 1998, **37**, 5823–5829, DOI: 10.1364/AO.37.005823.
- [142] H. F. O. Müller, Application of holographic optical elements in buildings for various purposes like daylighting, solar shading and photovoltaic power generation, *Renewable Energy*, 1994, **5**, 935–941, DOI: 10.1016/0960-1481(94)90114-7.
- [143] L. Menez, J.-P. Mulet and P. Lalanne, *Light-diffusing grating*, 2010, US patent no. 2010/0128349 A1.
- [144] B. Bläsi, A. Gombert and M. Niggemann, in *Polymers - Opportunities and Risks II*, ed. P. Eyerer, M. Weller and C. Hübner, Springer, Berlin / Heidelberg, 2010, vol. 12, pp. 263–279, DOI: 10.1007/698_2009_14.
- [145] M. Hanauer, S. Pierrat, I. Zins, A. Lotz and C. Sönnichsen, Separation of Nanoparticles by Gel Electrophoresis According to Size and Shape, *Nano Letters*, 2007, **7**, 2881–2885, DOI: 10.1021/nl071615y.
- [146] U. Schnabel, C.-H. Fischer and E. Kenndler, Characterization of colloidal gold nanoparticles according to size by capillary zone electrophoresis, *Journal of Microcolumn Separations*, 1997, **9**, 529–534, DOI: 10.1002/(SICI)1520-667X(1997)9:7<529::AID-MCS2>3.0.CO;2-3.
- [147] F.-K. Liu, F.-H. Ko, P.-W. Huang, C.-H. Wu and T.-C. Chu, Studying the size/shape separation and optical properties of silver nanoparticles by capillary electrophoresis, *Journal of Chromatography A*, 2005, **1062**, 139–145, DOI: 10.1016/j.chroma.2004.11.010.
- [148] S.-W. Ahn, K.-D. Lee, J.-S. Kim, S. H. Kim, J.-D. Park, S.-H. Lee and P.-W. Yoon, Fabrication of a 50 nm half-pitch wire grid polarizer using nanoimprint lithography, *Nanotechnology*, 2005, **16**, 1874, DOI: 10.1088/0957-4484/16/9/076.

- [149] Z. Y. Yang and M. Zhao, A study of the porosities of polymer nanoporous films using numerical simulations and experimental methods, *Journal of Optics A: Pure and Applied Optics*, 2007, **9**, 872–876, DOI: 10.1088/1464-4258/9/10/017.
- [150] S. Ndoni, M. E. Vigild and R. H. Berg, Nanoporous Materials with Spherical and Gyroid Cavities Created by Quantitative Etching of Polydimethylsiloxane in Polystyrene-Polydimethylsiloxane Block Copolymers, *Journal of the American Chemical Society*, 2003, **125**, 13366–13367, DOI: 10.1021/ja0360034.
- [151] J.-Q. Xi, M. F. Schubert, J. K. Kim, E. F. Schubert, M. Chen, S.-Y. Lin, W. Liu and J. A. Smart, Optical thin-film materials with low refractive index for broadband elimination of Fresnel reflection, *Nature Photonics*, 2007, **1**, 176–179, DOI: 10.1038/nphoton.2007.26.
- [152] S. Yu, T. K. S. Wong, X. Hu and K. Pita, Sol-gel derived mesoporous silica films used as low dielectric constant materials, *Thin Solid Films*, 2004, **462–463**, 311–315, DOI: 10.1016/j.tsf.2004.05.029.
- [153] S. H. Behrens and D. G. Grier, The charge of glass and silica surfaces, *Journal of Chemical Physics*, 2001, **115**, 6716–6721, DOI: 10.1063/1.1404988.
- [154] Molecular Probes. Certificate of analysis, C37231 CML latex, lot no. 813621.
- [155] S. H. Behrens, D. I. Christl, R. Emmerzael, P. Schurtenberger and M. Borkovec, Charging and Aggregation Properties of Carboxyl Latex Particles: Experiments versus DLVO Theory, *Langmuir*, 2000, **16**, 2566–2575, DOI: 10.1021/la991154z.
- [156] J. E. A. M. van den Meerakker, P. C. Baarslag and M. Scholten, On the Mechanism of ITO Etching in Halogen Acids: The Influence of Oxidizing Agents, *Journal of The Electrochemical Society*, 1995, **142**, 2321–2325, DOI: 10.1149/1.2044294.
- [157] J. J. Mazer and J. V. Walther, Dissolution kinetics of silica glass as a function of pH between 40 and 85°C, *Journal of Non-Crystalline Solids*, 1994, **170**, 32–45, DOI: 10.1016/0022-3093(94)90100-7.
- [158] J. D. Rimstidt and H. L. Barnes, The kinetics of silica-water reactions, *Geochimica et Cosmochimica Acta*, 1980, **44**, 1683–1699, DOI: 10.1016/0016-7037(80)90220-3.
- [159] G. B. Alexander, W. M. Heston and R. K. Iler, The Solubility of Amorphous Silica in Water, *The Journal of Physical Chemistry*, 1954, **58**, 453–455, DOI: 10.1021/j150516a002.
- [160] S. Behrens, M. Borkovec and M. Semmler, in *Trends in Colloid and Interface Science XII*, ed. G. Koper, D. Bedeaux, C. Cavaco and W. Sager, Springer, Berlin / Heidelberg, 1998, vol. 110, pp. 66–69, DOI: 10.1007/BFb0118051.
- [161] R. Reisfeld, T. Saraidarov and B. Jasinska, Porous glasses as a matrix for incorporation of photonic materials. Pore determination by positron annihilation lifetime spectroscopy, *Optical Materials*, 2004, **26**, 181–189, DOI: 10.1016/j.optmat.2003.11.019.

- [162] Sartorius AG, Goettingen, Germany. <http://www.sartorius-mechatronics.com>.
- [163] M. Naciri, D. Kuystermans and M. Al-Rubeai, Monitoring pH and dissolved oxygen in mammalian cell culture using optical sensors, *Cytotechnology*, 2008, **57**, 245–250, DOI: 10.1007/s10616-008-9160-1.
- [164] D. Wencel, B. D. MacCraith and C. McDonagh, High performance optical ratiometric sol-gel-based pH sensor, *Sensors and Actuators B: Chemical*, 2009, **139**, 208–213, DOI: 10.1016/j.snb.2008.12.066.
- [165] C. Higgins, D. Wencel, C. S. Burke, B. D. MacCraith and C. McDonagh, Novel hybrid optical sensor materials for in-breath O₂ analysis, *Analyst*, 2008, **133**, 241–247, DOI: 10.1039/b716197b.
- [166] PreSens Precision Sensing GmbH, Regensburg, Germany. <http://www.presens.de>.
- [167] D. Quéré, Wetting and Roughness, *Annual Review of Materials Research*, 2008, **38**, 71–99, DOI: 10.1146/annurev.matsci.38.060407.132434.
- [168] S. Shibuichi, T. Onda, N. Satoh and K. Tsujii, Super Water-Repellent Surfaces Resulting from Fractal Structure, *The Journal of Physical Chemistry*, 1996, **100**, 19512–19517, DOI: 10.1021/jp9616728.
- [169] X. J. Feng and L. Jiang, Design and Creation of Superwetting/Antiwetting Surfaces, *Advanced Materials*, 2006, **18**, 3063–3078, DOI: 10.1002/adma.200501961.
- [170] P. Patel, C. K. Choi and D. D. Meng, Superhydrophilic Surfaces for Antifogging and Antifouling Microfluidic Devices, *Journal of the Association for Laboratory Automation*, 2010, **15**, 114–119, DOI: 10.1016/j.jala.2009.10.012.
- [171] J. Bico, U. Thiele and D. Quéré, Wetting of textured surfaces, *Colloids and Surfaces A: Physicochemical and Engineering Aspects*, 2002, **206**, 41–46, DOI: 10.1016/S0927-7757(02)00061-4.
- [172] D. M. Spori, T. Drobek, S. Zürcher, M. Ochsner, C. Sprecher, A. Mühlebach and N. D. Spencer, Beyond the Lotus Effect: Roughness Influences on Wetting over a Wide Surface-Energy Range, *Langmuir*, 2008, **24**, 5411–5417, DOI: 10.1021/la800215r.
- [173] J. Bico, C. Tordeux and D. Quéré, Rough wetting, *Europhysics Letters*, 2001, **55**, 214, DOI: 10.1209/epl/i2001-00402-x.
- [174] F.-M. Chang, S.-J. Hong, Y.-J. Sheng and H.-K. Tsao, Wetting Invasion and Retreat across a Corner Boundary, *The Journal of Physical Chemistry C*, 2010, **114**, 1615–1621, DOI: 10.1021/jp9097588.
- [175] C. W. Extrand, S. I. Moon, P. Hall and D. Schmidt, Superwetting of Structured Surfaces, *Langmuir*, 2007, **23**, 8882–8890, DOI: 10.1021/la700816n.

- [176] L. Courbin, E. Denieul, E. Dressaire, M. Roper, A. Ajdari and H. A. Stone, Imbibition by polygonal spreading on microdecorated surfaces, *Nature Materials*, 2007, **6**, 661 – 664, DOI: 10.1038/nmat1978.
- [177] R. D. Deegan, O. Bakajin, T. F. Dupont, G. Huber, S. R. Nagel and T. A. Witten, Capillary flow as the cause of ring stains from dried liquid drops, *Nature*, 1997, **389**, 827–829, DOI: 10.1038/39827.
- [178] K. L. Sebastian and A. K. R. Paul, Kramers problem for a polymer in a double well, *Physical Review E*, 2000, **62**, 927–939, DOI: 10.1103/PhysRevE.62.927.
- [179] V. Korampally, S. Mukherjee, M. Hossain, R. Manor, M. Yun, K. Gangopadhyay, L. Polo-Parada and S. Gangopadhyay, Development of a Miniaturized Liquid Core Waveguide System With Nanoporous Dielectric Cladding – A Potential Biosensing Platform, *IEEE Sensors Journal*, 2009, **9**, 1711–1718, DOI: 10.1109/JSEN.2009.2030287.
- [180] N. Gopalakrishnan, K. S. Sagar, M. B. Christiansen, M. E. Vigild, S. Ndoni and A. Kristensen, UV patterned nanoporous solid-liquid core waveguides, *Optics Express*, 2010, **18**, 12903–12908, DOI: 10.1364/OE.18.012903.
- [181] M. Gleiche, L. F. Chi and H. Fuchs, Nanoscopic channel lattices with controlled anisotropic wetting, *Nature*, 2000, **403**, 173–175, DOI: 10.1038/35003149.